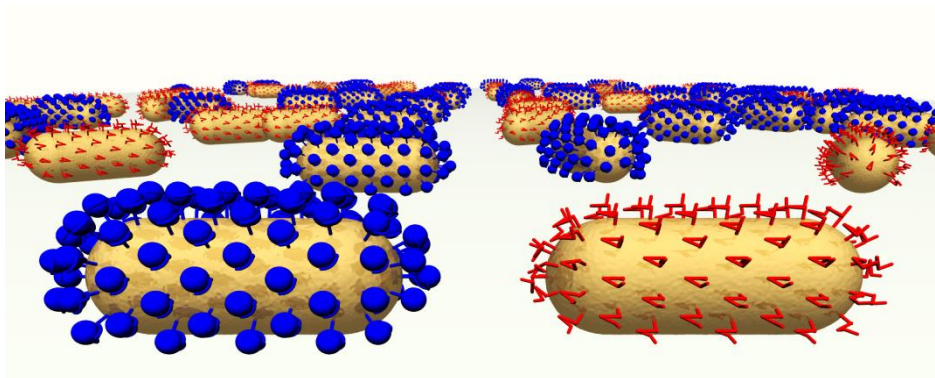# Sensing Applications of Biofunctionalised Plasmonic Gold Nanoparticles

Dissertation zur Erlangung des Grades
"Doktor der Naturwissenschaften" im Promotionsfach Chemie
am Fachbereich Chemie, Pharmazie und Geowissenschaften
der Johannes Gutenberg-Universität in Mainz

Janak Prasad

geboren am 28.10.1984 in Jamshedpur (INDIA)

Mainz, November 2014

"Somewhere, something incredible is waiting to be known."

-Carl Sagan

Dedicated to

My parents and family members

ABSTRACT

Plasmonic metal nanoparticles focus, amplify and manipulate light at the nanoscale level. This fundamental property comes from the collective coherent oscillations of conduction band electrons resonantly excited by incident light in metal nanoparticles called Localised Surface Plasmon Resonance (LSPR) or 'particle plasmons'. Plasmons in metal nanoparticles have been used for sensing of disease relevant biomolecules, in photothermal therapy and to improve the efficiency of solar cells. In this thesis, I will focus on synthesis and functionalisation aspects of gold nanoparticles to carry out sensing applications with these.

Recent improvements in wet chemical synthesis have led to production of gold nanoparticles with different shapes and sizes that differ in their sensing capabilities. Among the various shapes, gold nanorods are often the most preferred shape for biomolecule sensing by LSPR. The nanorods are stabilised by a positively charged CTAB layer that can attract proteins at near neutral pH. The adsorption and desorption of proteins can be studied at single molecule level to decipher the binding kinetics of proteins on the nanoparticle surface. I describe such a study performed with high spatial and temporal resolution to determine the single binding events of fibronectin onto gold nanorods.

Gold nanorods must be functionalised with specific biorecognition elements to perform analyte detection or study interaction between proteins in a multiplexed manner. I functionalise gold nanorods with short DNA sequences (aptamer sequences and NTA conjugated polythymidines) and successfully performed multiple analyte (or protein-protein interactions) with these functionalised particles.

Plasmons of clustered nanoparticles couple which changes the resonance energy. Controlled assembly of nanospheres into dimers and higher order structures such as core-satellites can serve as a means to enhance their sensitivity. These clusters offer higher senstivity due to presence of plasmonic hotspots in the interparticle gap region. The plasmonic coupling is a distance dependent phenomena which forms the basis of plasmon rulers. I have developed a strategy to produce Hsp90 functionalised dimers of gold nanospheres. This technique does not suffer from photobleaching and photoblinking effects (as in dyes) and is shown for the first time to study protein (Hsp90) conformational dynamics.

SCIENTIFIC PUBLICATIONS

"Single Unlabeled Protein Detection on Individual Plasmonic Nanoparticles"
I. Ament, J. Prasad, A. Henkel, S. Schmachtel and C. Sönnichsen
Nano Letters **2012**, 12, 1092-1095.

"Multiplex Plasmon Sensor for Rapid Label-Free Analyte Detection"
J. Prasad*, C. Rosman*, A. Neiser, A. Henkel, J. Edgar and C. Sönnichsen
Nano Letters **2013**, 13, 3243-3247.

"Plasmonic Nanosensors for Simultaneous Quantification of Multiple Protein-Protein Binding Affinities"
R. Ahijado-Guzman, J. Prasad, C. Rosman, A. Henkel, L. Tome, D. Schneider, G. Rivas and C. Sönnichsen
Nano Letters **2014**, 14, 5528-5532.

"Plasmonic Core-satellite Assemblies as Highly Sensitive Refractive Index Sensors"
J. Prasad, I. Zins, R. Branscheid, J. Becker, A. Koch, G. Fytas, U. Kolb and C. Sönnichsen
The Journal of Physical Chemistry C, Under Review.

Table Of Contents

List of figures

List of tables

Chapter 1

Basic Introduction and Theoretical Framework on Plasmons

1.1 Emergence of Plasmonics

Gold has fascinated researchers across the globe by its enigmatic behaviour since centuries. The material is mainly famous for its remarkable ornamental value and to some extent for its supposed medicinal value.[1] In fact, the medieval artisans empirically used 'finely divided gold' to achieve red colouration in church window glasses. The Lycurgus cup (4th century AD) is probably the most famous example of the use of gold nanoparticles in ancient times, exhibiting different coloration when observed upon illumination inside or outside of the cup. There is also evidence of the ancient use of metallic nanoparticles in glass and pottery from Egyptian dynasties, Celtic enamels, Japanese and Chinese glasses.[2] Ironically, even though these structures and many others were produced with ease, it still took quite a while to discover and understand the underlying optical phenomena that drives such intriguing effects.

It was not until 150 years ago, when the phenomenon behind the stained glasses started unfolding. In 1857, Michael Faraday for the first time produced "colloidal gold" in solution and observed their optical properties.[3] The actual scientific study on nanometric gold started in the early 20th century when Gustav Mie (1908)[4] and Richard Gans (1912) presented a solution to Maxwell equations that describes the extinction spectra of spherical and spheroidal nano-objects of arbitratry size and hence explains the surprising optical properties of metallic colloids .With the pioneering work of Mie and others the origin of the optical properties of metallic nanoparticles was understood and a new field of plasmonics was born. This field deals with phenomena of amplification, concentration and manipulation of light at the nanoscale level by metallic nanoparticles.

1.2 Definition of Surface Plasmons

Noble metal nanoparticles have a large fraction of atoms concentrated at their surface. All noble metal atoms exhibit completely filled (n-1) d orbitals. However, the corresponding ns (and np) orbitals of such nanoparticles only have a lone electron in it. In the range of 5-200 nm diameters, gold nanoparticles are large enough to support a conduction band which is

formed by the half-filled ns and np orbitals. Thus, a metal nanoparticle can be visualised as a lattice of ionic cores with the conduction electrons moving almost freely through vacant orbitals even at room temperature.[5,6]
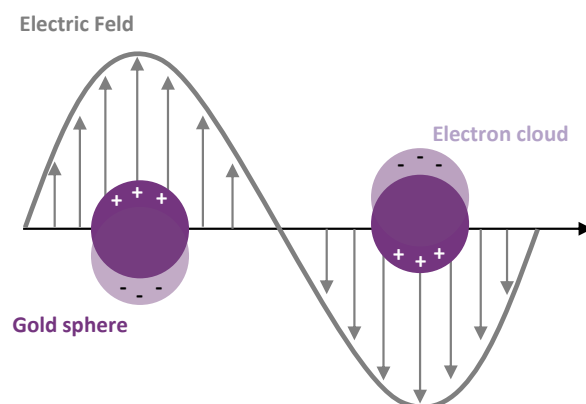
Figure 1.1. Schematic showing the collective oscillation of conduction band electrons in gold nanoparticles.

Nanoparticles upto 200 nm size are much smaller than the wavelength of light. When the nanoparticles are illuminated, a part of the incident light is absorbed in moving the conduction band electrons towards the nanoparticle surface. This leads to the development of a negative charge on one side (where the conduction electrons are accumulated), and an equal positive charge at the other side of the nanoparticles, thereby creating a dipole. The dipole produces an electric field inside the nanoparticle opposite to that of the light, which in turn, gives rise to a linear restoring force. The restoring force on the electrons forces them to return to the equilibrium position. As a consequence, a dipolar oscillation of electrons is created. The collective coherent oscillations of the conduction band electrons in metal nanoparticles are known as 'Plasmons' (Figure 1.1). The frequency at which oscillations occur is known as 'plasmon resonance frequency'. As a result of these oscillating dipoles, light is radiated from the nanoparticles in the form of scattering. Since the dipolar oscillations are confined to the surface of metal nanoparticles, the phenomena is known as 'Localised Surface Plasmon Resonance (LSPR)'. Surface plasmons are of interest because they can concentrate light energy much below optical wavelengths, suggesting their use for subwavelength lithography,[7] optical computing and imaging.[8]

1.3 Theories on Plasmons

Several theories have been proposed to describe the plasmons in metal nanoparticles. Out of them, the two most noteworthy ones are described here.

1.3.1 The Electrostatic modelling: Quasi Static Approximation (QSA)

The electrostatic approach gives a qualtitative description of the amount of light a metallic nanoparticle can absorb or scatter. However, this theory does not hold good for very small and very large nanoparticles. The collective oscillation of electrons in metal nanoparticles is described by the polarizability (α):

$$\alpha(\lambda) = \frac{1}{L}\varepsilon_0 V \frac{\varepsilon(\lambda)-\varepsilon_m}{\varepsilon(\lambda)+\kappa\varepsilon_m} \qquad (1.1)$$

where V is the volume of the particle , ε_m is the dielectric constant of the surrounding medium, L is the shape factor (L=1/3 for spherical particles) that incorporates the dependence of the polarisability on the geometry of the surface and ε is the dielectric function of the metal nanoparticle.

The dielectric function of the metal (ε), is frequency dependent and has real and imaginary parts as given by:

$$\varepsilon(\lambda) = \varepsilon_1(\omega) + \varepsilon_2(\omega) \qquad (1.2)$$

where, n is the refractive index and κ is the light absorption coefficient.

The induced dipole moment (p) that results from electronic polarisation is given by:

$$p = \varepsilon_m \alpha E_0 \qquad (1.3)$$

The electric field (E_i) produced by the dipole inside a spherical particle is described by the equation :

$$E_i = E_0 \frac{3\varepsilon_m}{\varepsilon(\lambda)+2\varepsilon_m} \qquad (1.4)$$

The resonance occurs for polarizability and dipole electric field when the terms in the denominator go to a minimum, ie:

$$[\varepsilon_1(\omega) + 2\varepsilon_m]^2 + [\varepsilon_2(\omega)]^2 = minimal \quad (1.5)$$

Which is fullfilled when $\varepsilon_1(\omega)$= -2ε_m and $\varepsilon_2(\omega)$<<1.

The real part (ε_1) of the metal dielectric function governs the frequency position of the plasmon resonance while the imaginary part (ε_2) determines the width and height of the resonance.

1.3.2 The Electrodynamic modelling: Mie Theory

In order to calculate the response of a metal nanoparticle to an external electromagnetic field, one must solve Maxwell's equations. Fortunately, an analytical solution already exists generally known as *'Mie Theory'*.[4] The theory is valid for all nanoparticle sizes and optical wavelengths in contrast to Rayleigh's scattering theory, which is limited to nanoparticles much smaller than the wavelength of the incident radiation. In fact, Rayleigh scattering is a first-order approximation of Mie-Theory.[9]

In his solution of the Maxwell equations, Mie describes the interaction between a plane wave and uncharged homogeneous particles. This allows the precise calculation of the electromagnetic fields within and surrounding the particle. The spherically symmetrical geometry suggests a multipole expansion of the fields. The resulting surface harmonics enable the calculation of the extinction, scattering and absorption cross-sections of the particles as follows:

$$\sigma_{ext} = \frac{2\pi}{|k^2|} \sum_{L=1}^{\infty} (2L + 1).Re[a_L + b_L] \qquad (1.6)$$

$$\sigma_{scat} = \frac{2\pi}{|k^2|} \sum_{L=1}^{\infty} (2L + 1).[|a_L|^2 + |b_L|^2] \qquad (1.7)$$

$$\sigma_{abs} = \sigma_{ext} - \sigma_{scat} \qquad (1.8)$$

where a_L and b_L are Mie-coefficients from the multipole expansion, L is the multipole order (L=1 for dipole mode) and k is the wave vector of the incident electromagnetic wave. For nanoparticles much smaller than wavelength of light the, the formula can be simplified to:

$$\sigma_{ext} = 9\frac{\omega}{c} \, \varepsilon_m^{3/2} \, V \frac{\varepsilon_2(\omega)}{[\varepsilon_1(\omega)+2\varepsilon_m]^2+[\varepsilon_2(\omega)]^2} \qquad (1.9)$$

1.4 Plasmonic nanoparticles as sensors

The resonance properties depend on the properties of the nanoparticles (such as size, shape, material) and those of the external dielectric medium. During the excitation of surface plasmons, the dipole of opposite charges on the nanoparticle surface creates an electric field in the vicinity of the nanoparticle. This field induces the polarisation of the dielectric medium, thereby resulting in charge accumulation in the dielectric medium interfaced with the metallic surface. Thus, both the nanoparticle and the dielectric medium polarize each other.[2] This charge tends to compensate the charge accumulation due to the movement of conduction

electrons in the nanoparticles and hence reduces the net charge at the nanoparticle surface. The adjustment of the charge density depends on the dielectric function (ε_m) of the surrounding medium. Thus, the larger the ε_m, the larger is the polarisation of the medium and the more is the compensation effect. Reduction of the net charge at the nanoparticle surface corresponds to the reduction in the restoring force. Lowering the restoring force leads to smaller resonance frequency (and higher wavelength). The dielectric function of the medium (ε_m) is related to its refractive index (n), as $n^2 = \varepsilon_m$. Thus, when the refractive index of the surrounding medium increases, the surface plasmon band also gets red shifted to larger wavelengths (Figure 1.2). The dielectric nature of the medium interfaced with the nanoparticle surface can be changed by changing the refractive index of the medium, surface modification of the nanoparticle and nanoparticle aggregation.
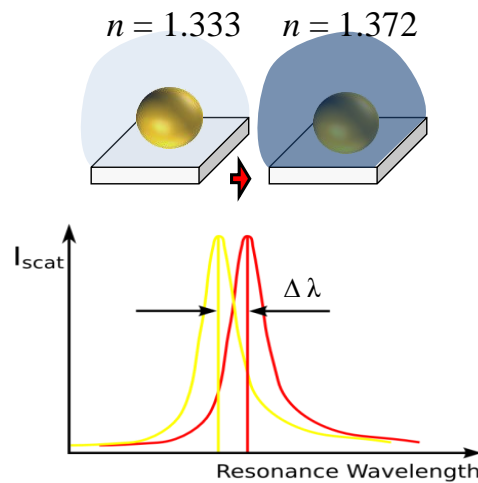
Figure 1.2. Effect of surrounding medium on gold nanoparticles. Schematic shows spectral shift in resonance maxima of gold nanoparticles due to change in refractive index (n=1.333 to n=1.37) of the surrounding medium.

To measure the impact of change in the refractive index of the surrounding medium onto the nanoparticle's spectral position, the term 'Sensitivity' has been coined. Sensitivity is defined as:

$$S_\lambda = \Delta\lambda / \Delta n \qquad (1.10)$$

Where $\Delta\lambda$ denotes the spectral shift in the nanoparticle's resonance position and Δn is the change in the refractive index of the surrounding medium. The higher sensitivity value of a particle, the better it is for sensing applications.

The sensitivity of a plasmonic nanoparticle is typically evaluated by its figure of merit (FoM),defined as the ratio of the plasmon frequency shift per refractive index unit change in the surrounding medium divided by the width of the spectral resonance peak. This accounts for both the absolute shift in the resonance peak position and the width of the resonance in defining the sensitivity of an LSPR sensor. Large shifts with narrow resonances lead to higher FoM and sensitivity. The highest FoM reported for any individual nanoparticle is 5.4 for a sharply spiked gold nanostar.[10]

1.5 General requirements for Plasmon-based sensing

Gold nanoparticles are unique in the sense that they do not photobleach and photoblink like the fluorescent dyes. Moreover, they offer a very high scattering efficiency and size and shape dependent tunability of their resonance position over a large spectral range. These properties make gold nanoparticles useful for applications like sensing of chemical and biological entities (such as disease markers)[11] and live imaging of the cells.[12] However, in order to explore and realize some of these potential applications of gold nanoparticles one must take a note of the two main basic criteria that must be fulfilled by these nanoparticles when using them in biologically relevant media: stability and specificity.

1.5.1 Nanoparticle stability

Gold nanoparticles are usually stable in aqueous solutions because of their charge and/or the presence of a protective layer around them. The protective layer are formed by the ingredients pertinent to the synthesis of these nanoparticles and may include: (1) citrate to stabilise gold nanospheres[13] and (2) cetyltrimethylammonium bromide (CTAB) to stabilise gold nanorods.[14] These layers tend to destabilise and the nanoparticles tend to irreversibly aggregate when ionic strength of the medium reaches that of a biological fluid. Nanoparticle aggregation is highly unfavourable process as it alters the physical properties of gold nanoparticles. Two effects are noteworthy- firstly, an increase in the size and polydispersity index of the nanoparticles depending on the extent of aggregation and thus increased light scattering and, secondly, the change in the initial colour of the nanoparticle dispersion to blue or grey. This colour change is brought about by the coupling of plasmons of the neighbouring particles and a comcomitant red shifting of their plasmon frequencies. The colloidal stability

of the nanoparticles in ionic buffers and simulated biological fluids can be achieved by means of surface modification with suitable coordinating species such as thiols or surfactants.

1.5.2 Particle functionalisation for target specificity and selectivity

Functionalisation of gold nanoparticles is a major parameter for maintaining their monodispersity in physiological buffers. Functionalisation serves two purposes: (a) it allows for the control of interactions neighbouring nanoparticles leading to their agglomeration under a certain specific condition (b) it is required for a selective interaction between a biomolecule of interest (such as proteins and other ligands) and nanoparticle. Fortunately, the surface atoms of the gold nanoparticle seem to exhibit incomplete valence which makes it perfect for interacting with donor-acceptor species (or ligands). For this reason, metal nanoparticles can show similar behavior as their related metal complexes, forming selective chemical bonds with appropriate ligands. Among the reactive groups that bind to gold surface include thiol (-SH), amine (-NH$_2$), carboxy(-COOH), phosphine (-PH$_3$)[15] and its derivatives amongst others.[16] Thiol group has the highest affinity towards the gold surface which makes it suitable for ligand exchange reactions on gold nanoparticles. Often bifunctional ligands bearing at least one thiol group is used to attach proteins and other biomolecules to gold.

Gold nanospheres capped with citrate are simpler to functionalise with thiol bearing molecules (thiolated DNA and proteins), the same is however not true for gold nanorods because of the presence of CTAB. Besides being considered a potential protein denaturant[17] and cytotoxic, the presence of CTAB may also interfere with established protein-nanoparticle conjugation protocols. General methods for conjugation of gold nanorods with proteins employ either- (1) surfactants, (2) polyelectrolytes or (3) small thiolated molecules. In the first two cases, a surfactant [18, 19] or polyelectrolyte (PAA)[20] is first adsorbed onto the CTAB layer of gold nanorods. The first method holds good only for thiolated proteins (derived from reduction with TCEP or DTT), wherein the protein replaces the CTAB-surfactant complexes and binds directly to the nanorod surface. In the second method, multiple layer-by layer assemblies of ployelectrolytes (PAA/PDDA) are formed onto the gold nanorods. The protein is bound onto the final PAA layer. In the third method, CTAB layer on gold nanorod is exchanged with small ligand molecules such as cystamine/cysteamine,[21] mercaptoundecanoic acid[22] or thiolated polyethylene glycols. Later, coupling agents (Glutaraldehyde[21] , EDC/NHS[22]) are employed to covalently link proteins to the functionalised ligands. Thiolated proteins can also bind directly to the gold nanorod surface via ligand exchange.

1.6 Approaches of Plasmonic Sensing

Functionalised gold nanoparticles have been used as sensors for molecular detection. The sensing principle relies on either changing the refractive index in the vicinity of the nanoparticles or on agglomeration of the nanoparticles in the presence of the target molecule. The following discusses the two most common sensing approaches based on the aforementioned principle.

1.6.1 Ensemble based approach

In this approach, a concentrated solution of functionalised gold nanoparticles is reacted to the target molecules in bulk. Target binding is detected by monitoring a change in the resonance position of the ensemble. Since this approach is mass sensitive, it particularly works well for antibody-antigen or aptamer-target binding assays wherein the target is large and concentrated enough to produce a significant red-shift in the ensemble spectra. However, binding of smaller molecules can go undetected.
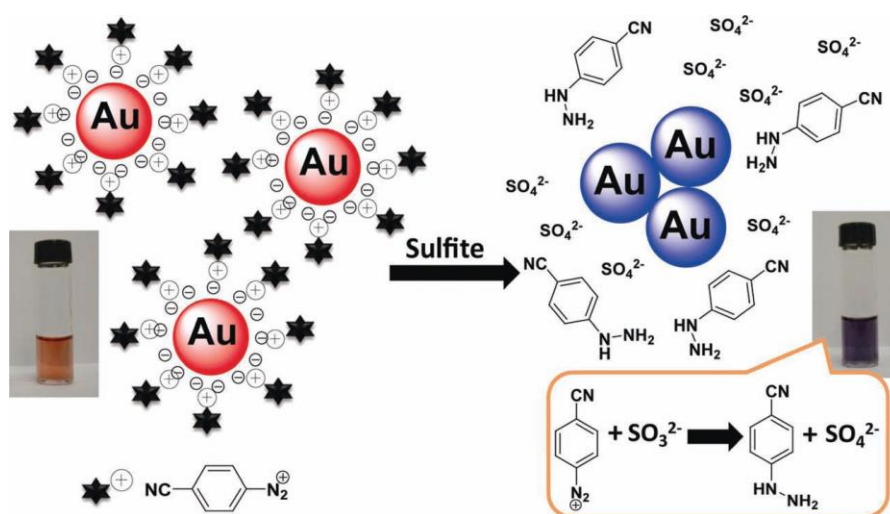
Figure 1.3. Colorimetric detection of molecules with gold nanoparticles.[23]

Colorimetry is another simple way of observing target binding to the nanoparticles (Figure 1.3). Herein, the surface chemistry of the nanoparticles is designed in such a way that a reversible aggregation happens in them depending on the presence or absence of the target. This in turn leads to a concomitant change colour of the suspension from red to purple and can be detected by naked eye.

Ensemble measurements are often advantages to qualtitatively determine the presence of target antigen in the physiological solutions. However, this detection method requires

concentrated functionalised nanoparticle suspension for analyte sensing, is often limited to single time use and difficult to multiplex.

1.6.2 Single particle based approach

Single particle spectroscopy is a robust technique to detect changes taking place on the surface of single metal nanoparticles. In these techniques, nanoparticles are usually randomly deposited onto surface of a glass flow cell channel. A dark field setup (designed for single particle spectroscopy) collects the light scattered by individual nanoparticles and displays the spectral position of their plasmon resonance.[24] Each nanoparticle responds to any modification made in the embedding medium (due to analyte binding or particle-particle interactions) by a change in the spectral position of its plasmon resonance. This spectral change can be monitored and analysed to depict and understand the underlying processes at the nanoscale level in a qualitative and quantitative way. Besides having the advantages of an ensemble based technique, single particle approach requires less sensing particles and can be used for multiplexed detection of analytes in a small sample volume.

1.7 Plasmon Coupling: As a route to enhance sensitivity

Combining the nanoparticles together results in the coupling between the plasmons of individual nanoparticles. At the nanoparticle level, coupling between two or more particle plasmons lead to a significant red shift in the spectra of the original sensing nanoparticle. This principle has been used to increase the measured signal in single particle based sensing by sandwiching the analyte of interest between two plasmonic nanoparticles. Since binding of one particle is enough to red shift the spectra (by an order of magnitude higher than produced due to refractometric changes from a protein monolayer on the nanoparticle surface), this method is also more efficient in detecting trace levels of biomolecules. In fact, several groups have been able to decrease the limit of detection of an analyte from nanomolar to picomolar and even femtomolar levels. The pinciple behind spectral shifts in nanoparticle pairs can be explained by several models as discussed below.

1.8 Plasmon Coupling Models

Three basic models have been described here to understand the basic phenomena that lead to Plasmon coupling between nanoparticles- (1) Exciton-coupling model (2) Dipolar coupling model (3) Plasmon hybridisation model.

1.8.1 Exciton-coupling model

This model assumes nanoparticles pairs to be analogous to transition dipoles of chromophores.[25] According to this model, the excited-state levels of each monomer split into a lower energy level and a higher energy level upon dimerization. These energy levels can have two possible arrangements (in a dipole) in the dimer -in-phase or symmetric and out-of-phase or anti-symmetric. The energy splitting 2U is given by the interaction energy which is approximated by the Coulombic interaction between the transition dipole moments of the monomers. The field E experienced by each dipole (μ) is the sum of the incident field E_0 and the field due to the neighboring dipole.

$$E = E_0 + \frac{\xi\mu}{4\pi\varepsilon_0\, r^3} \qquad (1.11)$$

$$U = -\frac{\xi|\mu|^2}{4\pi\varepsilon_0\, r^3} \qquad (1.12)$$

The additional field experienced by each dipole depends on the distance r between the nanoparticles. The orientation of the dipoles (ξ) is decided by the direction of the incident light. When the incident light polarization (and therefore both dipoles directed) are along the inter-particle axis, $\xi = 2$, and the interaction energy U is negative .This implies that the interaction is attractive for dipoles aligned symmetrically, which is manifested by a red-shift in the resonance frequency in the dimer. The dipoles aligned anti-symmetrically are higher in energy, but are optically forbidden for homodimers and manifest itself as a dark mode. When the incident field polarization (and hence the direction of both dipoles) is orthogonal to the inter-particle axis, $\xi = -1$, which means a positive interaction energy. For the dipoles aligned symmetrically, the interaction is repulsive. As a result, a blueshift of the resonance frequency is observed in this case, however the shift magnitude is smaller than the parallel polarization case, since the interaction energy is twofold smaller in magnitude in this case. The anti-symmetric configuration is lower in energy, but is optically forbidden for homodimers.

This model can only offer a qualitative explanation to plasmon coupling. It does not take into account the retardation of the electromagnetic field. Since the particles have a finite size and cannot really be considered point dipoles, the retardation of the electromagnetic field when the particle size becomes appreciable in relation to the wavelength of the light. In addition, it also neglects higher order multipole– multipole type interactions that become important when the interacting particles come very close (separation < 0.5 diameter).

1.8.2 Dipolar coupling model

This model was described by Kreibig and Vollmer to qualitatively explain interparticle plasmon coupling on the basis of dipole-dipole interactions. In a nanoparticle pair, the dipolar nearfield of a plasmonic particle decays as the cube of the inverse distance. This means that the plasmon coupling strength is also a function of d^{-3}, a dependence which can be approximated very nearly to an exponential decay.While the interparticle dipolar coupling potential is known to decay with center-to-center distance as d^{-3}, the intraparticle restoring potential (reflected by the inverse of the dipole polarizability) is inversely proportional to the volume (or diameter), D^3. As a result, fractional plasmon shift ($\Delta\lambda/\lambda_0$) due to plasmon coupling becomes a function of (d/D)-3 or $(s/D + 1)$-3, where s is the interparticle edge-to-edge separation and D is the particle diameter (Figure 1.4). This function is independent of the metal type and dielectric constant of the surrounding medium and show weak dependence on particle shape.
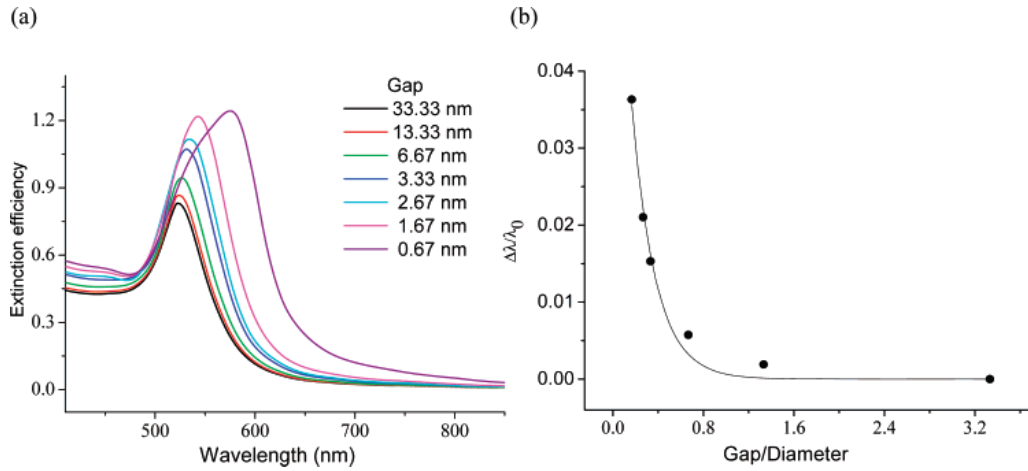
Figure 1.4. (a) DDA-simulated extinction efficiency spectra of 10 nm diameter Au nanosphere pair in water for varying interparticle separation gap for incident light polarization direction parallel to the interparticle axis. (b) Plot of fractional plasmon shift in Au nanosphere pair as a function of the gap/diameter ratio.[23]

The model was extended by Jain et al to derive the plasmon ruler equation for gold nanoparticle pairs as mentioned below.[26]

$$\frac{\Delta\lambda}{\lambda_0} \approx 0.18 \, e^{\frac{-(\frac{s}{D})}{0.23}} \qquad (1.13)$$

Like the exciton-coupling model, the quasistatic dipolar-coupling model too does not take into account electromagnetic retardation effects as well as higher-order/multipolar interactions the dipolar model. This model cannot validate the plasmon coupling strength in nearly touching dimers (with small interparticle gaps).

1.8.3 Plasmon hybridisation model

The plasmon hybridisation model was developed by Prodan et al.[27] In this method, the conduction electrons are modeled as a charged, incompressible liquid sitting on top of a rigid, positively charged ioncores. The nanoparticle pair and its spectrum is considered analogous to a homogeneous diatomic molecule and its molecular orbital diagram. According to this model, the plasmon modes ($\Psi 1$ and $\Psi 2$) of two interacting metal nanoparticles hybridize either in-phase ($\Psi 1 + \Psi 2$) or out-of-phase ($\Psi 1 - \Psi 2$).[28] When the incident light field is polarized along the interparticle axis (longitudinal polarization), the in-phase combination reflects the lower energy (red shifted) bonding mode (denoted as σ) and the out-of phase mode represents the higher energy (blue shifted) antibonding mode (denoted as σ^*). In the bonding mode, the electric field is enhanced at the junction of the particles, whereas the antibonding mode is characterized by the electric field localized on the nonjunction ends of the particles. However, when the polarization is perpendicular to the interparticle axis (transverse polarization), the in-phase combination is an antibonding mode (π^*) and the out-of phase one is a bonding mode (π). The shifts for transverse polaization are weaker than those due to longitudinal polarization. In the case of homodimers, the in-phase modes (σ and π^*) couples well to the far field and are known as 'bright modes' whereas the out-of phase modes (σ^* and π) are called 'dark modes' due to the cancellation of the equal but oppositely oriented dipoles on the two particles (Figure 1.5).
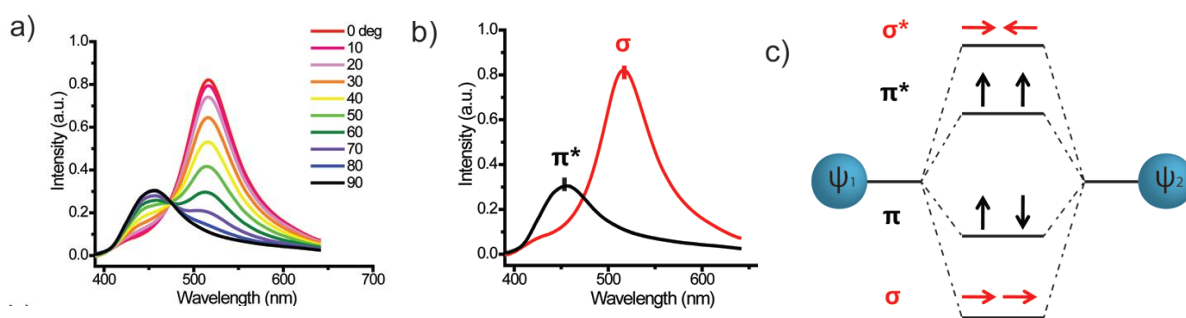
Figure 1.5. Plasmon coupling in symmetric silver nanoparticle dimers. Scattering spectra of homodimer as a function of the polarizer angle (0-90°). Two extreme cases from the polarization experiments of the homodimer dimer (b) which match well with the hybridization model (c). [25]

At large separation, the plasmons on the different nanoparticles interact only weakly and the dimer plasmons are essentially bonding and antibonding combinations of the nanoparticle plasmons of the same angular momentum l. In this case, the splitting between bonding and antibonding modes varies with $1/D^3$. At small interparticle separations, the dimer plasmons

contain contributions from all angular momenta and the interaction involves higher powers of $1/D$.

1.9 A technology with a bright future

Remarkable progress has been made in the field of plasmonics over the last few years. This includes new developments in the synthesis, assembly, characterization, and theory of conventional and unconventional metal nanostructures. Such developments have made strong impacton various applications of plasmonic nanoparticles such as chemical and biological sensing, photothermal therapeutics, and solar energy. Advanced setups are also being built to enable time-resolved studies in milliseconds to submilliseconds range. Further improvements are underway to explore other interesting features like femtosecond and picosecond dynamics associated with the excitation of plasmons to determine plasmon-resonance quality and line shape, plasmon heating, and the interaction of plasmons with the nearby environment.

In my thesis, I highlight few of the many ways that could pave the way and accelerate the above mentioned developments. I have demonstrated ways to tailor plasmonic gold nanoparticles through surface functionalization and assembly process for applications which could be instrumental from the disease diagnosis point of view. An overview of the major research topics covered during my PhD have been conveyed below.

In chapter 2, I describe single unlabeled detection of proteins with the ultimate detection limit of single molecule by surfactant stabilized gold nanorods. Commonly, fluorescent dye labels or enzymatic amplification are employed for single molecule sensing which modifies the species under investigation and therefore influences biological processes. In this chapter, I present a novel technique for detection of single unlabeled fibronectin proteins with extremely high temporal resolution in milliseconds regime. Fibronectin molecules could also be desorbed from the nanorod surface with the help of anionic surfactants. This technique could potentially resolve equilibrium coverage fluctuations, opening a window into Brownian dynamics of unlabeled macromolecules.

Surfactant-capped gold nanorods attract proteins non-specifically. To perform an efficient and cost-effective multiplexed detection for proteins in small liquid samples, the gold nanorods were functionalised with DNA aptamers. In chapter 3, I present a novel multiplexed sensor with randomly deposited aptamer functionalized gold nanorods. The spectral position

of plasmon resonances of individual nanorods, monitored by dark-field spectroscopy, respond specifically to different proteins. Using four different target-aptamer partners, I have demonstrated nanomolar sensitivity, sensor recycling and the potential to upscale to hundreds or thousands of targets. The applications for inexpensive multiplexed sensors are abundant like identifying human, animal and plant diseases, monitoring food composition, quality and safety, screening for explosives, drugs or environmental hazards.

Multiplexed gold nanorod sensors are not only limited to the detection of aptamer specific targets, but they also be tailor made to perform simultaneous detection of protein-protein interactions. Most of current techniques used for the quantification of protein-protein interactions require the analysis of one pair of binding partners at a time. In chapter 4, I present a label-free, simple, fast and cost-effective route to characterize binding affinities between multiple macromolecular partners simultaneously, using optical dark-field spectroscopy and individual protein-functionalized gold nanorods as sensing elements. A stable stock of NTA DNA-functionalized gold nanorods was used to create a library of His-tagged protein-functionalized nanorods by simply adding proteins to small aliquots of the nanorod stock solution. As a proof of concept, the binding affinities of three interacting pairs (FtsZ-s1ZipA, FtsZ-s2ZipA and FtsZ-MinC) were successfully determined.

Multiplexed analyte detection schemes can largely benefit from highly sensitive and spectrally tunable plasmonic nanostructure. However, there is a lack of such nanostructures for the mid-visible spectral regions as most available nanostructures offer high sensitivity in red to far red spectrum. In chapter 5, I report a simple strategy to produce highly sensitive gold nanostructures that work in the mid-visible electromagnetic region. These structures are produced by the assembly of 20nm gold nanoparticle satellites onto 60 nm spherical gold cores under the influence of hydroxylamine. Due to plasmon coupling between interacting nanoparticles, the core-satellite structures show a two-fold higher sensitivity than similar sized gold nanospheres.

Plasmon coupling also forms the basis for distance dependent sensing by plasmon rulers or dimers. Plasmonic dimers respond to changes in interparticle separation by expressing a spectral shift in their resonance maxima and large changes in scattering intensity. In chapter 6, I present a system consisting of a single protein sandwiched between two functionalised gold nanospheres to exploit this distance dependent spectral shifts in monitoring conformatioanl dynamics of the protein. I used plasmonic gold nanoparticle dimers for long term

investigation of nucleotide-free N-terminal conformational dynamics in heat shock protein Hsp90 with millisecond temporal resolution. This work demonstrates the first proof of concept for detection of protein conformational dynamics by plasmon rulers.

References

1. Higby, G. *Gold Bull* **1982,** 15, (4), 130-140.

2. Garcia, M. A. *Journal of Physics D: Applied Physics* **2011,** 44, (28), 283001.

3. Faraday, M. *Philosophical Transactions of the Royal Society of London* **1857,** 147, 145-181.

4. Mie, G. *Annalen der Physik* **1908,** 330, (3), 377-445.

5. Walter, M.; Akola, J.; Lopez-Acevedo, O.; Jadzinsky, P. D.; Calero, G.; Ackerson, C. J.; Whetten, R. L.; Grönbeck, H.; Häkkinen, H. *Proceedings of the National Academy of Sciences* **2008,** 105, (27), 9157-9162.

6. Juan, M. L.; Righini, M.; Quidant, R. *Nat Photon* **2011,** 5, (6), 349-356.

7. Srituravanich, W.; Fang, N.; Sun, C.; Luo, Q.; Zhang, X. *Nano Letters* **2004,** 4, (6), 1085-1088.

8. Fang, N.; Lee, H.; Sun, C.; Zhang, X. *Science* **2005,** 308, (5721), 534-537.

9. Acquista, C. *Appl. Opt.* **1976,** 15, (11), 2932-2936.

10. Liao, H.; Nehl, C. L.; Hafner, J. H. *Nanomedicine* **2006,** 1, (2), 201-208.

11. Tiwari, P.; Vig, K.; Dennis, V.; Singh, S. *Nanomaterials* **2011,** 1, (1), 31-63.

12. Long, Y.-T.; Jing, C., Springer Berlin Heidelberg: 2014; pp 99-116.

13. Haiss, W.; Thanh, N. T. K.; Aveyard, J.; Fernig, D. G. *Analytical Chemistry* **2007,** 79, (11), 4215-4221.

14. Jana, N. R.; Gearheart, L.; Murphy, C. J. *The Journal of Physical Chemistry B* **2001,** 105, (19), 4065-4067.

15. Negishi, Y.; Chaki, N. K.; Shichibu, Y.; Whetten, R. L.; Tsukuda, T. *Journal of the American Chemical Society* **2007,** 129, (37), 11322-11323.

16. Zhang, F.; Lees, E.; Amin, F.; Rivera_Gil, P.; Yang, F.; Mulvaney, P.; Parak, W. J. *Small* **2011,** 7, (22), 3113-3127.

17. Vlasova, I. M.; Zhuravleva, V. V.; Saletskii, A. M. *Russ. J. Phys. Chem.* **2012,** 86, (3), 509-515.

18. Wang, Y.; Tang, L.-J.; Jiang, J.-H. *Analytical Chemistry* **2013,** 85, (19), 9213-9220.

19. Pekcevik, I. C.; Poon, L. C. H.; Wang, M. C. P.; Gates, B. D. *Analytical Chemistry* **2013,** 85, (20), 9960-9967.

20. Wang, J.; Dong, B.; Chen, B.; Jiang, Z.; Song, H. *Dalton Transactions* **2012,** 41, (36), 11134-11144.

21. Singh, A. K.; Senapati, D.; Wang, S.; Griffin, J.; Neely, A.; Candice, P.; Naylor, K. M.; Varisli, B.; Kalluri, J. R.; Ray, P. C. *ACS Nano* **2009,** 3, (7), 1906-1912.

22. Yu, C.; Nakshatri, H.; Irudayaraj, J. *Nano Letters* **2007,** 7, (8), 2300-2306.

23. Du, J.; Shao, Q.; Yin, S.; Jiang, L.; Ma, J.; Chen, X. *Small* **2012,** 8, (22), 3412-3416.

24. Rosman, C.; Prasad, J.; Neiser, A.; Henkel, A.; Edgar, J.; Sönnichsen, C. *Nano Letters* **2013,** 13, (7), 3243-3247.

25. Jain, P. K.; El-Sayed, M. A. *Chemical Physics Letters* **2010,** 487, (4–6), 153-164.

26. Jain, P. K.; Huang, W.; El-Sayed, M. A. *Nano Letters* **2007,** 7, (7), 2080-2088.

27. Prodan, E.; Radloff, C.; Halas, N. J.; Nordlander, P. *Science* **2003,** 302, (5644), 419-422.

28. Sheikholeslami, S.; Jun, Y.-w.; Jain, P. K.; Alivisatos, A. P. *Nano Letters* **2010,** 10, (7), 2655-2660.

Chapter 2

Single unlabeled protein detection of individual plasmonic nanoparticles

Towards detection of biological changes on the molecular level, fluorescence and/ or enzymatic reactions are among the most commonly used techniques. However, their use might modify the species of interest that often changes the reaction itself. The present chapter discusses optical monitoring of unlabelled protein adsorption on single gold nanorods with a broader aim of detection of single binding events with high temporal resolution. In this work, I propounded the idea of using a fibronectin as a model protein for our research due its compact and globular shape; and high molecular weight. I characterised the adsorption of fibronectin to gold nanorods by dark-field spectroscopy and also demonstrated the protein desorption from nanoparticle surface by sodium dodecylsulphate. My experiments laid the foundation of Dr. Irene Ament's work on detection of single unlabelled protein (fibronectin) detection with high spatial and temporal resolution.

This work resulted from a collaboration with Irene Ament, Andreas Henkel, and Sebastian Schmachtel and was published as 'Single Unlabeled Protein Detection on Individual Plasmonic Nanoparticles' in Nanoletters.

2.1 Introduction

Measurements of the behavior of proteins in a fluid typically return information on their "ensemble" characteristics, although the behavior of the individual molecules might differ quite substantially. In particular when trying to understand complex conformational dynamics of a protein, or when there is a need for spatially or temporally resolved measurements, the measurement of dynamic changes on the single molecule level becomes important.[1] Unfortunately, there is a relative lack of experimental techniques to observe conformational changes of e.g. proteins in their natural environment without influencing the dynamics of the reaction..[2] Current methods that are available for these types of measurements are e.g. optical microcavities (whispering gallery modes WGM)[3,4], surface-enhanced Raman scattering (SERS),[5] and electric detection via carbon nanotube[6] or boron-doped silicon nanowire[7] field-effect transistors. The inherent disadvantages of these techniques such as low signal-to-noise

levels, or complex sensor fabrication methods, have thus far prevented their entry into routine use.

2.2.1 Sensing principle

Plasmonic nanoparticles[8-10] undergo a spectral shift in response to changes in the refractive index of their direct environment, which can be monitored by optical dark-field spectroscopy[11]. This can be measured by illuminating rod-shaped gold nanoparticles immobilized on a glass surface in a way that their surrounding environment can be modified. Only the scattered light from the particles is then detected by the dark field microscope system.

2.2.2 Basic features of the sensor compared to other techniques

To efficiently capture single binding events of molecules, we introduced two changes: the employment of EMCCD camera (iXon, Andor DV885) and the use of a white light laser (SuperK-Power, spectral regime 460 nm − 2400 nm, total average power output 2.8 W) for particle illumination to augment the signal-to-noise level.[12] These changes permitted a higher temporal resolution of measurements. Compared to optical microcavities[13], the introduction of these improvements provides a simplified optical setup, in addition to the wet-chemical sensor fabrication of plasmonic nanoparticles. Importantly, the use of nanoparticles facilitates the physical integration of the sensor into biological systems on the nanoscale, as is the case in protein-protein interaction. As a practical consequence, the sensing volume is enhanced, in comparison with planar detection methods, such as SPR.

2.2 Experimental Results

In this section, a model system to demonstrate time-resolved single protein adsorption-desorption reactions on gold nanoparticles is presented.

2.2.1 Size distribution of the model protein

The blood plasma protein fibronectin (molecular weight 450 kDa)was used as a model protein to study molecular binding events on nanoparticle surfaces. The size of the fibronectin molecules was measured using transmission electron microscopy. Equal volumes of fibronectin (12.5μg /ml in PBS buffer (0.01 M phosphate buffer, 0.0027 M potassium chloride and 0.137 M sodium chloride)) were mixed with 0.2wt% sodium phosphotungstate

staining agent and incubated for 1 hour at room temperature. 5µl of the mixture was transferred to a 200-mesh carbon coated copper grid and evaporated overnight. TEM images were acquired on an electron microscope with an accelerating voltage of 120kV (Phillips EM420). Electron microscopy confirmed a globular-to-elliptical structure of the proteins, and the relative uniformity of the size distribution (9.3+/-2.3 nm) indicated that the predominant conformation was the dimer (Figure 2.1). Because in the dried form of the protein, these dimensions represent the minimal molecular extension, and it was therefore necessary to account for the hydrated structure (average size 12 nm)[14] for our experiments.

(a)   **(b)**
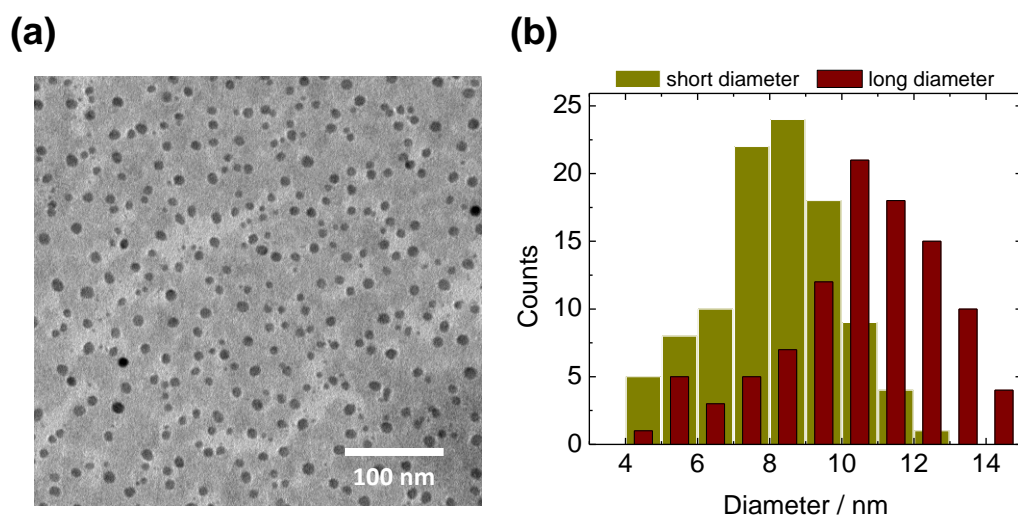
Figure 2.1. Transmission Electron Microscopy of fibronectin. (a) TEM micrograph of fibronectin stained with sodium phosphotungstate dye. (b) The relative equality of short vs. long diameter counts indicates the predominant presence of elliptical particles.

2.2.2 Demonstration of protein adsorption on gold nanoparticles

 CTAB stabilised gold nanorods were immobilised in a glass flow cell using 1M NaCl solution. The channel was rinsed with PBS buffer (0.01 M phosphate buffer, 0.0027 M potassium chloride and 0.137 M sodium chloride) to remove unbound nanoparticles. Resonance position of immobilised gold nanorods were recorded in PBS buffer to serve as a reference measurement. Bovine fibronectin (2.5µg/ml) in PBS buffer was then injected into the flow cell and incubated for 30 minutes. After the incubation, the channel was rinsed with PBS buffer and resonance wavelength of the nanorods were measured. It was observed that the resonance position of gold nanorods red shifts by 3-5 nm (depending on the aspect ratio of gold nanorods used). This spectral shift occurs due to adsorption of fibronectin onto gold nanorods (Figure 2.2). To determine the nature of this adsorption process, I used two methods

to detach the bound proteins. In the first method, SDS (a negatively charged surfactant) in PBS buffer was injected into the flow channel and incubated for 20 minutes. Subsequently, excess surfactant molecules are flushed out by rinsing the flow cell with PBS buffer. The resonance position measured after surfactant washing step shows a blue shift of a higher magnitude (Figure 2.2a). This blue shift confirms the desorption of protein molecules from the nanorod surface. A higher blue shift also indicates the possible desoption of CTAB layer. In the econd method, the nanoparticles were rinsed with sodium acetate buffer (pH 5.0) for 30 min after the fibronectin binding step. At this pH the charge on fibronectin molecules becomes neutral. However, the charge neutralisation did not lead to a significant desorption of the protein from the surface (Figure 2.2b). This indicates a much stronger binding of fibronectin molecules to gold nanorods (preferably to CTAB layer).
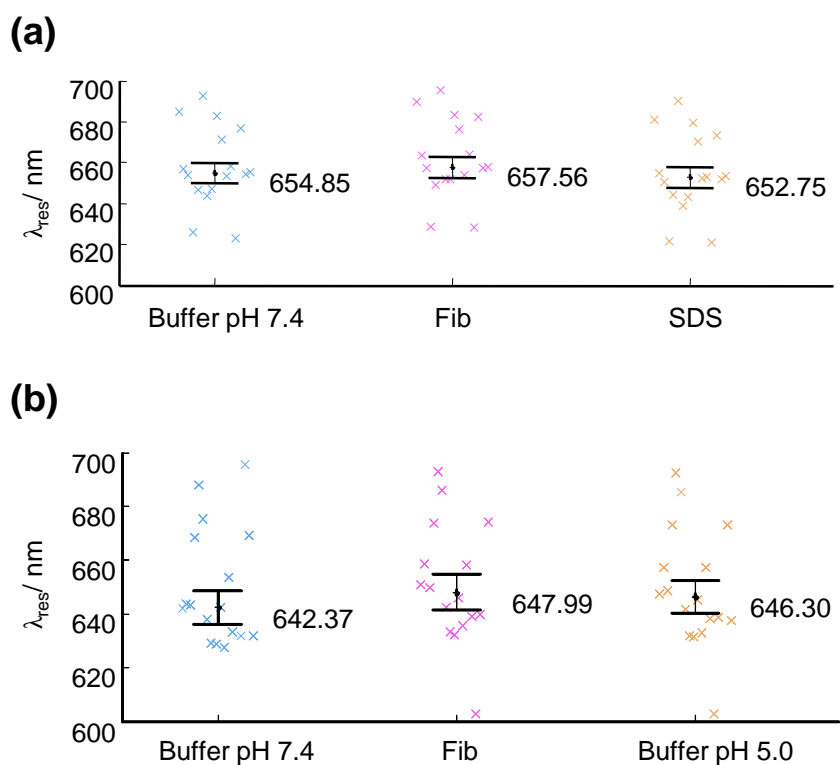
Figure 2.4 Adsorption of fibronectin on gold nanorods leads to a red shift in their resonance wavelength (shown in pink crosses). Each cross corresponds to one particle. **a**.Subsequent rinsing with sodium dodecyl sulfate in same buffer causes a blue shift of a higher magnitude in their resonance wavelength (shown in orange crosses). **b**. fibronectin cannot be desorbed just by a pH change around the isoelectric point of fibronectin. The error bars in black represent the s.e.m on 16-18 nanoparticles.

2.2.3 Proof of concept of single protein detection

Binding of fibronectin molecules to the gold nanoparticle surface was confirmed by the spectral shift in the plasmon resonance of gold nanorods. The observation that the addition of SDS induces a blue shift (indicative of protein desorption) in the resonance spectrum supports the hypothesis that electrostatic interaction drives the binding of protein to the CTAB layer on the nanorod surface, making direct adsorption of proteins to pristine gold nanorods less probable. A concentration-dependent adsorption behavior of fibronectin was studied with millisecond temporal resolution. A reduction of fibronectin concentration to 1.25 µg/ml resulted in the appearance of discrete steps in the resonance time trace (Figure 2.3a,b). The most plausible explanation for this observation is the binding and detachment of individual attaching molecules.[12] The dynamics of single-molecule adsorption and desorption behavior are discussed more exhaustively in a different thesis work.[12]
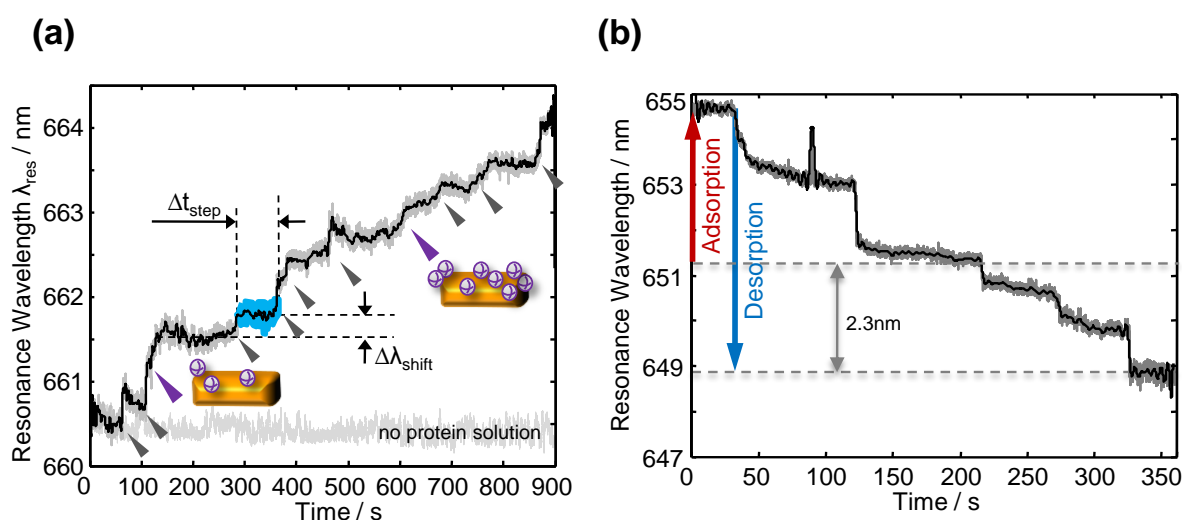
Figure 2.3 Discrete changes in resonance position due to fibronectin binding (a) and desorption (b) to/from gold nanorods, using single particle dark-field spectroscopy. The observation that the desorption step sizes are greater than those observed during adsorption are due to multiple molecules detaching at the same time.[12]

2.2.4 Dependence of resonance wavelength step size on fragment size

In order to test whether the resonance wavelength shift was dependent on the size of the adsorbing or detaching protein fragment, we cleaved the fibronectin dimers into their constituent monomers by incubating the protein for 5min with 5mM tris(2-carboxyethyl)phosphine (TCEP, Sigma). Such treatment reduced the resonance step size by half (Figure 2.4).
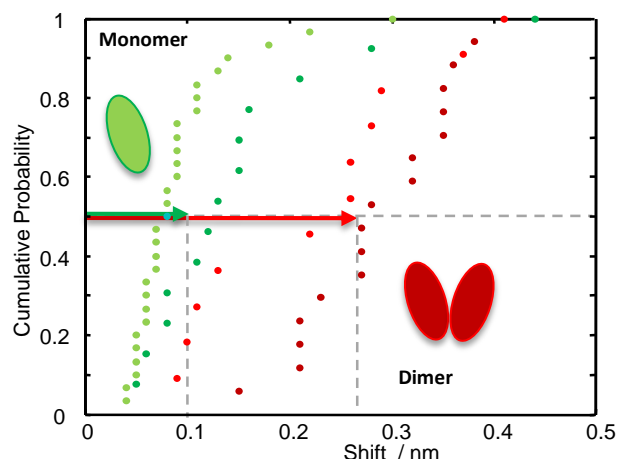
Figure 2.4 Comparison of the resonance wavelength shift step size between native and TCEP-treated fibronectin, using cumulative probability calculations. Two experiments were done with monomeric (green) and two with dimeric fibronectin.[12]

2.3 Conclusion

Conventional plasmon-based sensing techniques cannot track single molecular events and typically characterize the ensemble behavior of molecules. Specific improvements of the dark field microscopy setup involved a better temporal resolution by the camera and an optimized light source. The resulting data supports that, due to these improvements, it is now possible to measure single molecular adsorption and detachment events with sub-millisecond time regime. This capacity is unique among the methods of label-free detection and extends our capacity to apply label-free measurements of molecular interaction to the in-situ situation, e.g. on the surface of living cells. It can potentially also resolve equilibrium coverage fluctuations, opening a window into Brownian dynamics of unlabeled macromolecules. The dramatic improvements in signal to noise ratio for plasmon sensors we obtained here for our goal of single molecule detection will also improve other plasmonic sensors, e.g., plasmon rulers[15] or hydrogen sensors[16].

References

(1)   Henzler-Wildman, K.; Kern, D. *Nature* **2007**, *450*, 964-972.

(2)   Weiss, S. *Science* **1999**, *283*, 1676-1683.

(3)   Armani, A. M.; Kulkarni, R. P.; Fraser, S. E.; Flagan, R. C.; Vahala, K. J. *Science* **2007**, *317*, 783-787.

(4)   He, L.; Oezdemir, S. K.; Zhu, J.; Kim, W.; Yang, L. *Nat. Nanotechnol.* **2011**, *6*, 428-432.

(5)   Nie, S. M.; Emery, S. R. *Science* **1997**, *275*, 1102-1106.

(6)   Sorgenfrei, S.; Chiu, C. Y.; Gonzalez, R. L.; Yu, Y. J.; Kim, P.; Nuckolls, C.; Shepard, K. L. *Nat. Nanotechnol.* **2011**, *6*, 125-131.

(7)   Cui, Y.; Wei, Q. Q.; Park, H. K.; Lieber, C. M. *Science* **2001**, *293*, 1289-1292.

(8)   McFarland, A. D.; Van Duyne, R. P. *Nano Lett.* **2003**, *3*, 1057-1062.

(9)   Anker, J. N.; Hall, W. P.; Lyandres, O.; Shah, N. C.; Zhao, J.; Van Duyne, R. P. *Nat. Mater.* **2008**, *7*, 442-453.

(10)   Larsson, E. M.; Langhammer, C.; Zoric, I.; Kasemo, B. *Science* **2009**, *326*, 1091-1094.

(11)   Sönnichsen, C.; Franzl, T.; Wilk, T.; von Plessen, G.; Feldmann, J.; Wilson, O.; Mulvaney, P. *Phys. Rev. Let.* **2002**, *88*, 077402.

(12)   Ament, I.; Prasad, J.; Henkel, A.; Schmachtel, S.; Sönnichsen, C. *Nano Lett.* **2012**, *12*, 1092-1095.

(13)   Vahala, K. J. *Nature* **2003**, *424*, 839-846.

(14)   Koteliansky, V. E.; Glukhova, M. A.; Bejanian, M. V.; Smirnov, V. N.; Filimonov, V. V.; Zalite, O. M.; Venyaminov, S. Y. *Eur. J. Biochem.* **1981**, *119*, 619-624.

(15)   Liu, N.; Hentschel, M.; Weiss, T.; Alivisatos, A. P.; Giessen, H. *Science* **2011**, *332*, 1407-1410.

(16)   Liu, N.; Tang, M. L.; Hentschel, M.; Giessen, H.; Alivisatos, A. P. *Nat. Mater.* **2011**, *10*, 631-636.

Chapter 3

Multiplexed Analyte Sensing by Aptamer Functionalised Gold Nanorods

Parallel and sensitive detection of low abundant proteins from a single biological sample is of great demand in disease diagnostics and water quality monitoring. In this chapter, I present a novel multiplexed sensor composed of randomly deposited aptamer functionalized gold nanorods. The spectral position of plasmon resonances of individual nanorods, monitored by dark-field spectroscopy, respond specifically to different proteins. In this work, I made extensive search for biorecognition elements and came up with the idea of using short DNA aptamers for parallel detection of multiple targets. I screened and selected aptamers that do not exhibit any cross-talk with non-targets using SPR. I developed a new strategy to bind the thiolated DNA aptamers in their active conformation to the CTAB-stabilised gold nanorods and detect the targets successfully. Since aptamers bind to their targets on the basis of shape complementarity, I came up with the idea of utilizing proteases to cleave the bound target and dismantle its shape so that it can no longer be recognised with the aptamer. Besides the above mentioned contributions, I also shared experimental work with other co-authors.

This work resulted from a collaboration with Christina Rosman, Andreas Neiser, Andreas Henkel, and Jonathan Edgar and was published as 'Multiplexed Plasmon Sensor for Rapid Label-Free Analyte Detection' in Nanoletters .

3.1 Introduction

Early diagnosis of potentially lethal human diseases plays an essential role in their cure.[1] Biomarkers of these diseases constitute only a small fraction (around nanomolar concentration) in a highly complex proteome of unhealthy individuals.[2] Moreover, often simultaneous identification of multiple biomarkers is required to ascertain the type or cause of the disease.[3] Current techniques available for parallel sensing of analytes couple usually couple antibody molecules/fragments to spectrally encoded markers (e.g. SERS barcode,[4] luminex)[5] are are limited to simultaneous detection a few dozen independent targets. Planar spotting array based techniques such as, DNA microarrays[6] and multiplexed ELISA[7] can potentially detect more number of targets by specifying each spot to a binding position of a particular target type. However, the performance of current multiplexed detection schemes suffers from being either too complex, slow and/or expensive for routine use 'in the field'.[8]

Here I show a new approach for direct detection of multiple protein analytes simultaneously with aptamer functionalised gold nanorods. This approach allows batch synthesis of several varieties of target specific nanorods. Analyte binding to these nanorods leads to a spectral shift in their plasmon resonance[9] which is monitored and analyzed in parallel by our dark-field setups. An important feature of our aptamer based sensors is their quick reactivation which allows their multiple uses. By using four distinct proteins as targets, we demonstrate the feasibility of the concept for parellel analyte detection on a microfluidic flow cell onto sequentially deposited aptamer functionalised nanoparticles from different batches. With this simplify technique for multiplexed analyte detection we propose to reduce the costs of each sensor to negligible dimensions, especially if combined with advanced nanofabrication methods like nano-stamping[10] or optical trapping.[11] Such inexpensive sensor platform could be used for identifying human, animal and plant diseases, monitoring food composition, quality and safety, screening for explosives, drugs or environmental hazards.

3.1.1 The sensing modules

Our sensors are composed of aptamer functionalised gold nanorods. The prime reason behind using short DNA aptamers as receptors (instead of commonly employed but much larger antibodies)[12] is to make more efficient use of the sensing volume of gold nanoparticles.[13] Aptamers are short nucleic acid sequences (DNA/RNA) raised against a desired target by an iterative process known as SELEX (systematic evolution of ligands by exponential enrichment.[14] Unlike antibodies, they have a greater pH and temperature stability, simple activity regeneration and ability to bind to non-protein targets.[15] However, aptamers bind to their targets on the basis of shape complementarity; hence its structural stability is essential for target detection.

Nucleic acid aptamers adapt their active conformation in a buffered environment of high ionic strength. Ironically, the same buffer conditions lead to destabilisation of CTAB layer on gold nanorods which cause nanoparticle aggregation. To avoid such effects, I developed a novel strategy to functionalise the gold nanorods with active aptamers in buffered environment. My strategy consists of simple one pot addition aptamer molecules to gold nanorods in a buffer solution supplemented with SDS (a negatively charged surfactant that is known to prevent nanoparticle aggregation). SDS is known to increase tolerance of gold nanoparticles to increasing salt concentrations. We hypothesise that SDS micelles bind weakly and transiently to nanoparticles and prevent its non-specific interaction with the incoming ligand. This hypothesis is supported by the fact that SDS alone has not been able to

render any colloidal stability to nanoparticles in buffers. For the same reason, SDS is added to the buffered solution of thiolated aptamers so that it complexes with the CTAB layer and minimizes the non-specific interactions of CTAB layer with aptamers. The CTAB-SDS complexes on nanorod surface are slowly displaced by aptamers (Figure 3.1a). Our observation that both SDS and thiolated DNA aptamers causes the plasmon peak to shift to lower wavelength or higher energies (by electrostatic interaction leading to negative charging of the particles), supports our hypothesis (Figure 3.1b). As self-assembled monolayer of DNA aptamer has a higher negative charge density than the SDS, bound DNA causes a larger spectral shift than SDS, as evidenced by blue[16] shift of roughly 6 nm with DNA (Figure 3.1c). The spectra of gold nanorods collected post incubation with 0.4 % SDS in water, thiolated aptamer (in 0.4 % SDS in binding buffer), and thiolated mPEG (in 0.4 % SDS in binding buffer) show a similar full width at half maximum of the longitudinal plasmon peak and attests to the robustness of this functionalization strategy (Figure 3.1c).
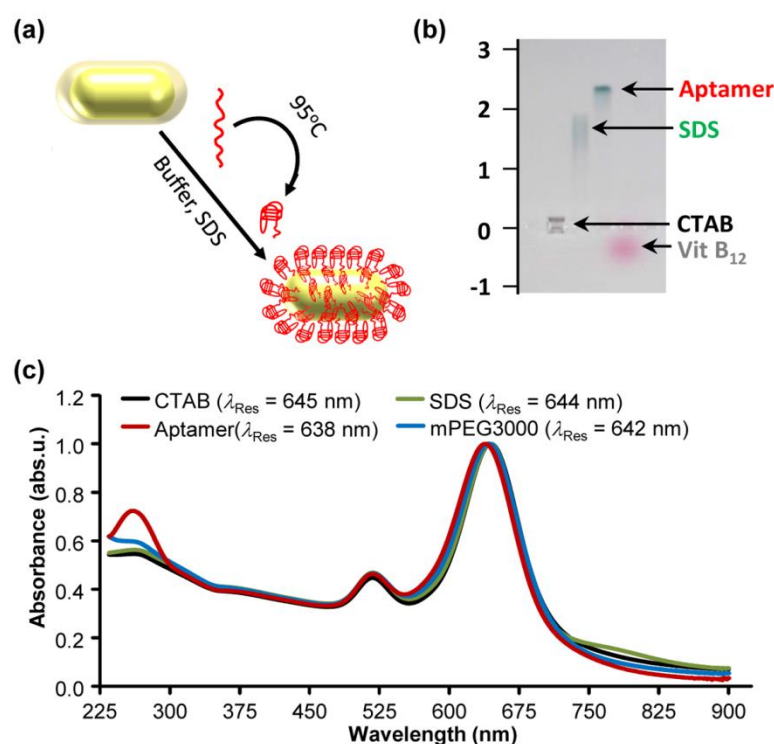
Figure 3.1. Batch synthesis of aptamer functionalised gold nanorods. a. Thiolated aptamers are heated at 95°C,10min in binding buffer in the presence of 0.3% SDS to mould them into their active conformation (G-uadruplexes in this case) and then reacted with the pellet of CTAB-stabilised gold nanorods. **b**.aptamer functionalised gold nanorods are stable in buffer and show faster electrophoretic mobility than SDS-stabilised gold nanorods (in water). The experiment was performed in 0.3% agarose in 0.5X TBE buffer (150V, 20 min runtime). **c**. UV visible spectra of gold nanorods after incubation with CTAB (black), SDS (green), thiolated aptamer (red) and thiolated methoxy-PEG (blue). The wavelength of the plasmon peak is indicated in the legend. In the UV region, the presence of the DNA aptamer is clearly visible by the characteristic DNA peak at 260nm.

3.1.2 Detection principle with plasmonic nanosensors

Plasmons in noble metal nanoparticles react to protein binding by a shift of the resonance wavelength.[17] Our approach is to simply deposit nanoparticles functionalised with receptors for specific targets T_i randomly from solution, while recording the position of each deposited nanoparticle, in order to know the specific target for each particle (see Appendix A, Figure A3). The plasmon shifts due to aptamer target interaction on each single nanoparticle is recorded by a fully automated, user friendly and fast dark-field spectroscopy system optimised for spectral precision. This system allows recording routinely the response of hundreds of particles with a precision of about 0.3 nm (corresponding to only a fraction of a percent of the plasmon linewidth or binding of about 30 proteins per particle).[18] The direct response to target binding is an advantage over fluorescence based techniques[19] (e.g. ELISA)[7] where labeling or multi-step procedures are required. With a similar system, we already demonstrated the ultimate sensitivity of single protein adsorption detection.[18] Compared to conventional SPR or SPR imaging,[20] the sensing volume for plasmons in metal nanoparticles are better matched to molecular dimensions[21] and the maximal integration density is an order of magnitude higher.

3.2 Experimental results

In this section, the main results on particle functionalisation, target specificity verification multiplexed detection of four different target proteins by aptamer functionalised gold nanorods and sensor regeneration will be presented.

3.2.1 Aptamer coverage on sensor

Aptamers in their active conformation (G-quadruplex for thrombin aptamer)[22] were conjugated via 3' thiol end group to the gold nanorods in a single step functionalisation procedure (see materials and methods section, Appendix B). Successful functionalisation was demonstrated by a blue shift in the longitudinal resonance spectra of nanorods and the emergence of a third spectral peak at 280 nm due to absorbance by DNA (Figure 3.1c). Thrombin aptamer (5'-SH-(T)$_{10}$AGTCCGTGGTAGGGCAGGTTGGGGTGACT-3') was used as model to determine the number of aptamer strands bound to the gold nanorod surface (Figure 3.2). Using UV absorbance at 260 nm, I determined the aptamer concentration in the supernatant after conjugation to gold nanorods. Three independent experiments resulted in concentrations of aptamer bound to nanorods of 0.403 μM, 0.3929 μM and 0.562 μM,

respectively. In order to quantify the number of rods, we calculate the molar extinction coefficient with the Mie-Gans theory[23] for the mean rod dimensions determined by transmission electron microscopy (67.8 nm × 31.1 nm). The corresponding values for aptamer load on particles were 2878, 2806, and 4015, respectively, yielding an average aptamer load of 3233 ± 553 aptamers per particle (mean and s.d.).
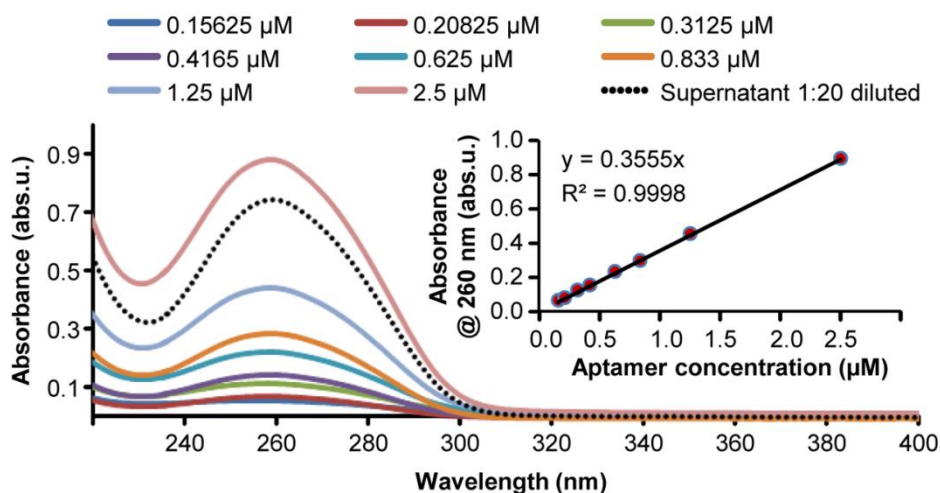
Figure 3.2. Estimation of aptamer coverage on nanorods. Calibration curve obtained with anti-thrombin aptamer in binding buffer. Dotted curve represents the aptamer in supernatant (dilution 1:20) after nanoparticle functionalization.

3.2.2 Verification of target binding affinity and specificity

The conventional method for aptamer selection relies on identifying nucleic acid sequences that bind to a protein of interest and then shortlisting sequences which still have the affinity for its target under stringent binding conditions. Therefore, little information is available on cross-reactivity of aptamers with non-target molecules. For an application like parallel sensing, it is highly desirable to have minimum to no cross talk between the aptamer and serum components. Therefore, I used the well-established SPR technique to study the interaction of selected aptamer sequences (see Appendix A) with of bovine serum albumin (BSA) and 11 other proteins including the targets. The first channel of a dual channel SPR system was functionalised with thiolated DNA aptamer in binding buffer. This was followed by passivation of bare gold areas in both channels of SPR chip with protein repellent thiolated methoxy-PEG layer. Only 6 out of 11 aptamers were found to bind to their targets in binding buffer. Two proteins (Human neutrophil elastase and Lyzozyme) showed cross-reactivity with

the other aptamers and hence were excluded from further studies (see Table A1, Appendix A). The SPR sensograms for remaining 4 aptamer-target pairs (for Fibronectin, Streptavidin, IgE and Thrombin) exhibited significant and specific response under experimental conditions (Figure 3.3) and were used for demonstration of parallel sensing of analytes.
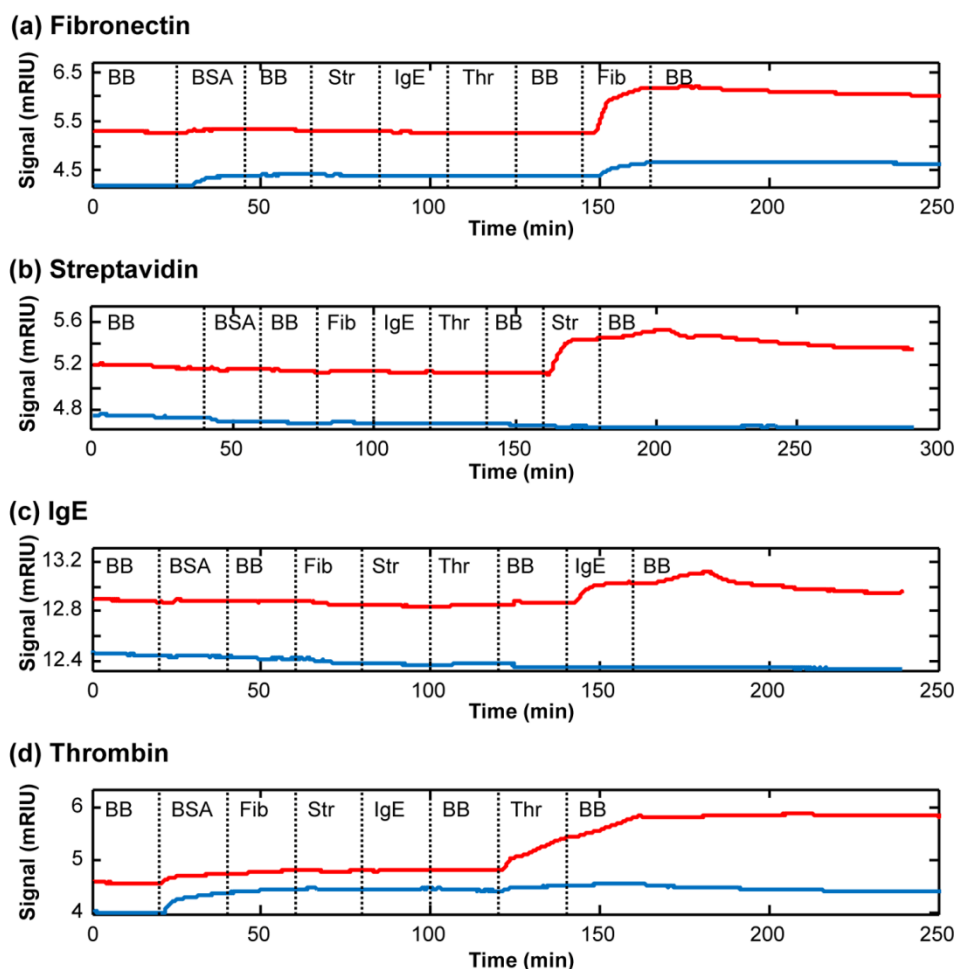
Figure 3.3. SPR sensograms showing aptamer-target specific interaction.**a**, anti-fibronectin Aptamer, **b**, anti-streptavidin aptamer, **c**, anti-IgE aptamer, **d**, anti-thrombin aptamer bind specifically to their targets under experimental conditions used. Blue - reference channel passivated with mPEG-SH, blue - sample channel functionalised with thiolated active aptamers. BB: binding buffer, BSA: Bovine Serum Albumin, Fib: Fibronectin, Str: Streptavidin, Thr: Thrombin, Lyz: Lysozyme, HNE: human neutrophil elastase.

3.2.3. Proof of concept of parallel sensing

To demonstrate the practicability of parallel detection, we flow-deposit four distinct aptamer functionalised gold nanorods in a microfluidic flow cell and sequentially group them by software based position indexing. The 'mapping' method with sequential deposition steps

(Figure A3-A4, Appendix A) is used to evaluate the response of the multiplexed sensor to Fibronectin (M_W 440 kDa), Streptavidin (M_W 66 kDa), Immunoglobulin E (IgE) (M_W 184 kDa) and Thrombin (M_W 37 kDa). Figure 3.4 shows the resulting response after sequentially flushing in Thrombin, Streptavidin, Fibronectin and IgE. The limit of detection for the sensor was determined to be in nanomolar regime.[24] Bovine serum albumin was used in excess in all the solutions to permanently block unspecific interaction of the analyte onto the glass surface. From figure 3.4, it is apparent that in all cases the plasmon shifts of the single nanoparticles are scattered around a median value of about ± 0.5 nm. A plausible explanation for this scattering could be measurement uncertainty, layer defects in functionalised particles that favours unexpected binding events. Due to this reason, collect statistics on many particle spectra is required for a precise and reliable sensor response evaluation.
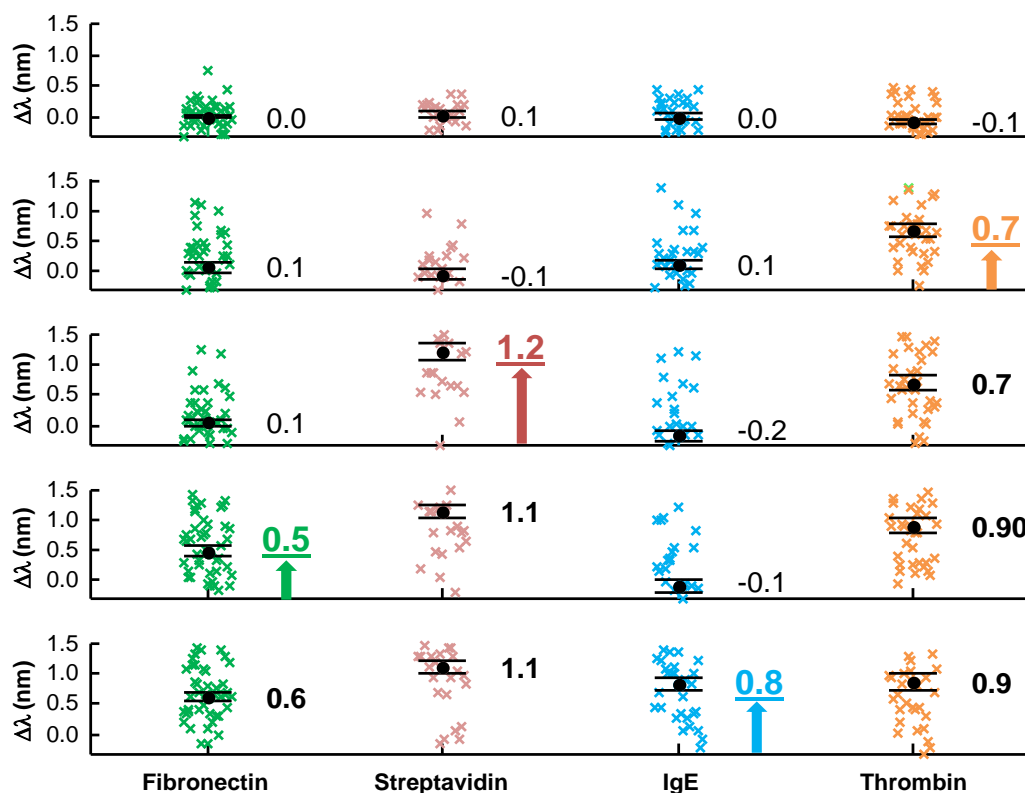
Figure 3.4. **Consecutive target detection in multiplexed sensor**. plot show the plasmon shifts of 160-360 particles in a multiplexed sensor after consecutive exposure to Thrombin, Streptavidin, Fibronectin, and IgE. Each cross represents the response of an individual nanoparticle. The four columns show the response of particles grouped according to their functionalisation (25-90 particles per group) with the median and its error (s.e.m.) indicated by black symbols and numbers. Median responses above the detection limit $L = 0.5$, indicated with arrows, correctly identify the analytes in all cases.

3.2.4. Sensor regenerations

Regeneration and reusability is an important aspect of a sensor not only commercial reasons but also because it allows having much better controls over the verification protocols. Most sensors are antibody based and are difficult to regenerate for multiple use without treating them with harsh solvents.[25] This treatment often leads to partial degradation of antibody structure. An advantage of using a non-proteinaceous biorecognition element such as a nucleic acid aptamer is that it allows us to remove protein targets by selective degradation (proteolysis). We demonstrate this regeneration concept by successfully removing the target protein (streptavidin) with the protease Trypsin (Figure 3.5). Trypsin protease has an autocatalytic enzyme and its activity gets inhibited in the presence of calcium and magnesium ions (constituents of binding buffer) which make it even more suitable for aptamer regeneration.
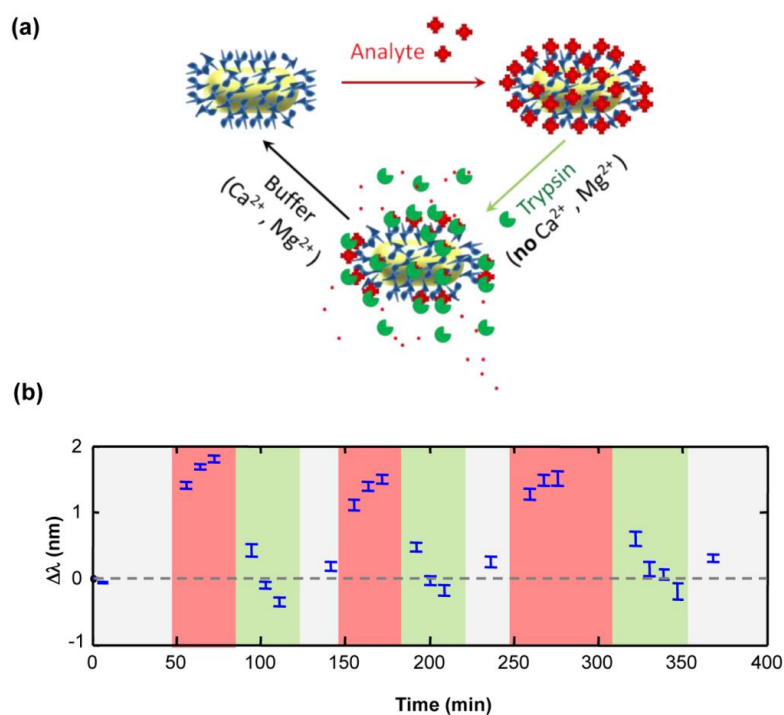
Figure 3.5. Sensor regeneration. a, Regeneration is performed with protease trypsin in buffer deviod of calcium and magnesium ions. Trypsin also has an autocatalytic activity in the reaction buffer and is inhibited in the binding buffer (with Ca^{2+}, Mg^{2+}). **b.** Sensor response **(**median and s.e.m. of 23 particles) after repeated incubation with Streptavidin (red shaded areas), protease trypsin (green shaded areas), and binding buffer (grey shaded areas. The target binding results in a strong plasmon shift $\Delta\lambda$ which is completely reversed to its original value after incubation with trypsin and rinsing with binding buffer.

3.4. Discussion

In this section, advantages of our sensing principle and possible ways to further improve these sensors will be discussed.

3.4.1 Key aspects of our sensor

Our technique for label free detection of multiple targets offers significant advantages compared to some known techniques. Firstly, no chemical manipulation of binding targets is required in our approach; therefore the binding kinetics of the proteins can be studied in unaltered state. Secondly, the fabrication of sensing platform is relatively cost effective since large scale batch functionalisation of gold nanorods can be performed quickly with ease, that remain are stable for weeks even at room temerature. Thirdly, the random deposition of nanoparticles eliminates the need for a tedious, time consuming and expensive substrate pattening of sensor. Last but not the least, since only one binding event between aptamer-target is monitored, parallel sensing of analytes is relatively short (15-20 minutes incubation excluding measurement time). In addition, the unique aspect the sensor regeneration and reusability could contribute towards cutting down the effective cost for multiple assays.

3.4.2. Perspective for technical improvements

The current system can acheive nanomolar limit of detection For detection of biomarkers down to subnanomolar or even sub-picomolar levels, the sensitivity could be further increased with secondary antibodies or nanotags[26] or by using more sensitive plasmonic geometries such as EIT structures[27] or fano resonances[28] instead of gold nanorods. Specificity and reliability of the sensor towards analyte detection can be further improved by replacing aptamers with highly specific antibodies[29] or Fab fragments. Key assests of our multiplexed sensor like small required sample volume and the fast and direct response with nanomolar sensitivity could be invaluable for point of care devices.

References

1.   de Jong, M. D.; Simmons, C. P.; Thanh, T. T.; Hien, V. M.; Smith, G. J. D.; Chau, T. N. B.; Hoang, D. M.; Van Vinh Chau, N.; Khanh, T. H.; Dong, V. C.; Qui, P. T.; Van

Cam, B.; Ha, D. Q.; Guan, Y.; Peiris, J. S. M.; Chinh, N. T.; Hien, T. T.; Farrar, J. *Nat Med* **2006,** 12, (10), 1203-1207.

2.   De, M.; Rana, S.; Akpinar, H.; Miranda, O. R.; Arvizo, R. R.; Bunz, U. H. F.; Rotello, V. M. *Nat Chem* **2009,** 1, (6), 461-465.

3.   Khunlertgit, N.; Yoon, B.-J. *EURASIP Journal on Bioinformatics and Systems Biology* **2014,** 2014, (1), 19.

4.   Cao, Y. C.; Jin, R.; Mirkin, C. A. *Science* **2002,** 297, (5586), 1536-1540.

5.   Vignali, D. A. A. *Journal of Immunological Methods* **2000,** 243, (1-2), 243-255.

6.   Schena, M.; Shalon, D.; Davis, R. W.; Brown, P. O. *Science* **1995,** 270, (5235), 467-470.

7.   Mendoza, L. G.; McQuary, P.; Mongan, A.; Gangadharan, R.; Brignac, S.; Eggers, M. *Biotechniques* **1999,** 27, (4), 778-780.

8.   Giljohann, D. A.; Mirkin, C. A. *Nature* **2009,** 462, (7272), 461-464.

9.   Famulok, M.; Mayer, G. *Accounts of Chemical Research* **2011,** 44, (12), 1349-1358.

10.   Nedev, S.; Urban, A. S.; Lutich, A. A.; Feldmann, J. *Nano Letters* **2011,** 11, (11), 5066-5070.

11.   Celebrano, M.; Rosman, C.; Soennichsen, C.; Krishnan, M. *Nano Letters* **2012,** 12, (11), 5791-5796.

12.   Jayasena, S. D. *Clinical Chemistry* **1999,** 45, (9), 1628-1650.

13.   Anker, J. N.; Hall, W. P.; Lyandres, O.; Shah, N. C.; Zhao, J.; Van Duyne, R. P. *Nature Materials* **2008,** 7, (6), 442-453.

14.   Stoltenburg, R.; Reinemann, C.; Strehlitz, B. *Biomolecular Engineering* **2007,** 24, (4), 381-403.

15.   O'Sullivan, C. *Anal Bioanal Chem* **2002,** 372, (1), 44-48.

16.   Novo, C.; Funston, A. M.; Mulvaney, P. *Nat Nano* **2008,** 3, (10), 598-602.

17.   Sönnichsen, C.; Geier, S.; Hecker, N. E.; von Plessen, G.; Feldmann, J.; Ditlbacher, H.; Lamprecht, B.; Krenn, J. R.; Aussenegg, F. R.; Chan, V. Z. H.; Spatz, J. P.; Moller, M. *Applied Physics Letters* **2000,** 77, (19), 2949-2951.

18.   Ament, I.; Prasad, J.; Henkel, A.; Schmachtel, S.; Sönnichsen, C. *Nano Letters* **2012,** 12, (2), 1092-1095.

19.   Saha, K.; Agasti, S. S.; Kim, C.; Li, X.; Rotello, V. M. *Chemical Reviews* **2012,** 112, (5), 2739-2779.

20.   Li, Y.; Lee, H. J.; Corn, R. M. *Nucleic Acids Research* **2006,** 34, (22), 6416-6424.

21. Ament, I.; Prasad, J.; Henkel, A.; Schmachtel, S.; Soennichsen, C. *Nano Letters* **2012,** 12, (2), 1092-1095.

22. Macaya, R. F.; Schultze, P.; Smith, F. W.; Roe, J. A.; Feigon, J. *Proceedings of the National Academy of Sciences* **1993,** 90, (8), 3745-3749.

23. Prescott, S. W.; Mulvaney, P. *Journal of Applied Physics* **2006,** 99, (12), 123504; **2008**, *103*, 119901.

24. Rosman, C.; Prasad, J.; Neiser, A.; Henkel, A.; Edgar, J.; Sönnichsen, C. *Nano Letters* **2013,** 13, (7), 3243-3247.

25. Starodub, N. F.; Dzantiev, B. B.; Starodub, V. M.; Zherdev, A. V. *Analytica Chimica Acta* **2000,** 424, (1), 37-43.

26. Osterfeld, S. J.; Yu, H.; Gaster, R. S.; Caramuta, S.; Xu, L.; Han, S.-J.; Hall, D. A.; Wilson, R. J.; Sun, S.; White, R. L.; Davis, R. W.; Pourmand, N.; Wang, S. X. *Proceedings of the National Academy of Sciences* **2008,** 105, (52), 20637-20640.

27. Liu, N.; Langguth, L.; Weiss, T.; Kaestel, J.; Fleischhauer, M.; Pfau, T.; Giessen, H. *Nature Materials* **2009,** 8, (9), 758-762.

28. Wu, C.; Khanikaev, A. B.; Adato, R.; Arju, N.; Yanik, A. A.; Altug, H.; Shvets, G. *Nature Materials* **2012,** 11, (1), 69-75.

29. Raschke, G.; Kowarik, S.; Franzl, T.; Sönnichsen, C.; Klar, T. A.; Feldmann, J.; Nichtl, A.; Kürzinger, K. *Nano Letters* **2003,** 3, (7), 935-938.

Chapter 4

Simultaneous Detection of Protein-protein Interaction by Ni²⁺-NTA Functionalised Gold Nanorods

Most of current techniques used for the quantification of protein-protein interactions require the analysis of one pair of binding partners at a time. In this chapter, I present a label-free, simple, fast and cost-effective route to characterize binding affinities between multiple macromolecular partners simultaneously, using optical dark-field spectroscopy and individual protein-functionalized gold nanorods as sensing elements. In this work, I successfully functionalised gold nanorods with just eleven-mer DNA strands and modified the other end of the DNA with NTA. This novel strategy to prepare NTA functionalised nanorods in high ioinic strength buffer solution proved invalable to our research. With this technique, I was able to attach his-tag proteins to gold nanorods with high specificity and perform protein-protein interaction studies along with Dr. Ruben Ahijado-Guzman. I believe that NanoSPR method could easily become a simple and standard tool in biological, biochemical and medical laboratories.

This work resulted from a collaboration with Rubén Ahijado-Guzmán, Christina Rosman, Andreas Henkel, and others and is submitted as ' Plasmonic Nanosensors for Simultaneous Quantification of Multiple Protein-Protein Binding Affinities' in Nanoletters .

4.1 Introduction

The dynamics in living organisms is governed by a complex network of interacting macromolecules.[1-3] For example, in a process like cell division, a dozen of proteins interact in a subtle and interconnected way of sub-processes to finally define a division place or to generate the constriction force in the cell wall.[4-6] To fully understand, model and potentially influence such a process, it is important to quantify binding affinities between all possible partners, preferentially without introducing fluorescent labels. Popularly techniques to do so are surface plasmon resonance (SPR) biosensors,[7] quartz crystal microbalance,[8] fluorescence correlation spectroscopy,[9] isothermal titration calorimetry,[10] or analytical ultracentrifugation.[11] However, most of the label-free techniques used to study binding affinities require the analysis of one pair of binding partners at a time, making the

quantification of a complex interaction network a laborious and slow effort. While there are some approaches described to increase the throughput by effectively building several experiments into one device, *e.g.* electro-switchable sensors,[12] multi-flow-channel SPR chips,[13] or microring resonators,[14] these approaches are expensive compared with nanoparticles and not as easily up-scalable.

4.2 Our sensing platform

We have tackled this problem in a novel way by employing individual gold nanorods as sensing elements. Each gold nanorod responds to binding events near its surface by a shift in the plasmon resonance wavelength.[15-17] The nanorods are connected to proteins via specific tags, making it simple to generate a library of nanoparticles, each functionalized with a different type of protein P_1 ...P_i. Particles from this library are deposited on a common substrate for simultaneous quantification of the interaction of proteins P_1 ...P_i with a common target molecule T. We demonstrate the power of this easily up-scalable approach by determining the binding affinities of three essential cell division proteins to the target FtsZ, a protein involved in constriction of the cell envelope during prokaryotic cell division.[4, 5]

Our 'NanoSPR' method provides a simple, fast and cost effective route to characterize binding affinities between many macromolecular partners simultaneously. This technique could become a simple standard tool in biological, biochemical and medical laboratories, where protein interactions with multiple partners is studied, *e.g.* in drug discovery projects, when active substances are screened for potential interference with cellular processes.

4.2.1 Nanosensor functionalisation strategy

The main challenge to develop plasmonic nanosensors as a general tool for the characterization of macromolecular binding affinities is to develop a general functionalization strategy to connect the nanoparticles with a given protein P_i. In protein biochemistry, (reversible) protein adsorption via so-called 'His-tags' is well-established, where histidine residues (His) complex a metal (*e.g.* Ni^{2+}) ion bound to a nitrilotriacetic acid (NTA) group. Since this method is often used in protein purification, numerous physiologically relevant proteins are already available with genetically fused His-tags. It is well established that the reversible Ni^{2+} - His interaction does (in most cases) not interfere with protein function. Therefore, we developed a strategy for the functionalization of gold nanorods with NTA while keeping the nanoparticles stable in solution (Figure 4.1a). A stable stock of NTA-

functionalized gold nanorods (AuNRs@Ni-NTA) provides an easy way to create a library of His-tagged protein-functionalized nanorods by simply adding proteins P_i to small aliquots of the (AuNRs@Ni-NTA) stock solution.
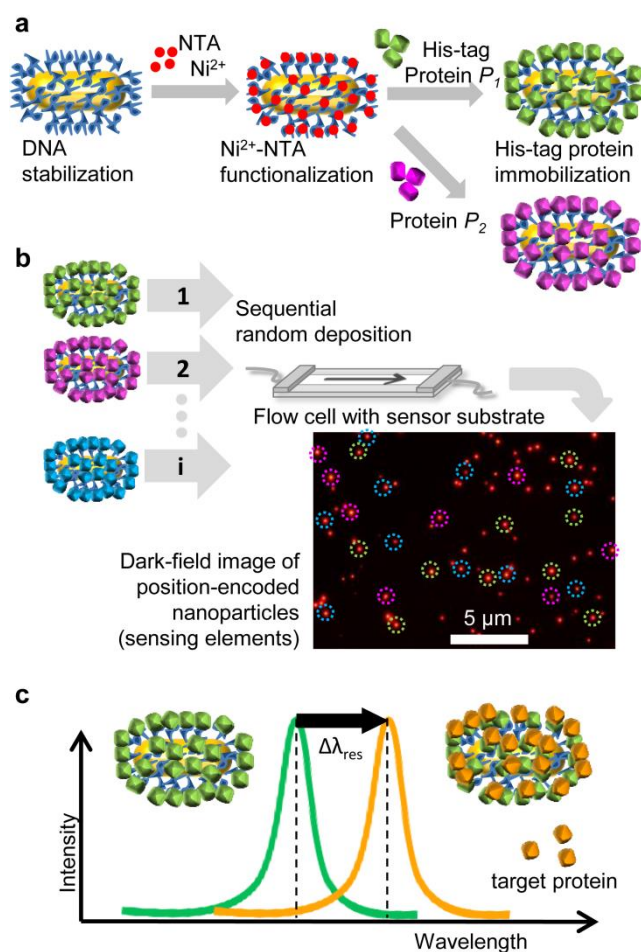
Figure 4.1. Principle of NanoSPR: particle functionalization, sensor fabrication, and detection principle. a, Scheme of the two-step functionalization strategy used to immobilize a protein P_i on gold nanoparticles. **b**, consecutive deposition of particles 1...i while recording their positions after each deposition step creates a position encoded sensor (inset). The inset shows a dark-field image of the resulting randomly deposited gold nanorods. Each nanorod serves as a sensing element for a specific protein-target interaction. **c**, The binding of target proteins T injected into the flow cell to nanoparticles covered by proteins P_i produces a shift $\Delta\lambda_{res}$ in the plasmon resonance.

4.2.2 Strategic assets of sensor preparation

However, the NTA functionalization must provide sufficient colloidal stability in buffers commonly used in a biological settings.[18] From synthesis, gold nanorods are typically stabilized with the surfactant cetyltrimethylammonium bromide (CTAB), which does, however, not prevent particle aggregation in saline buffers at physiological ionic strength. Direct substitution of CTAB by NTA does not yield sufficiently stable particles as well.

Therefore, we stabilize the gold nanorods first with short bifunctional DNA strands, consisting of eleven thymidine bases and a thiol/amine group at their ends. The thiol group readily binds to gold whereas the amine group is used to specifically couple with isothiocyanobenzyl-NTA in buffered aqueous solution. Established methods for the conjugation of gold nanorods with proteins employ either surfactants,[19] polyelectrolytes[20] or small thiolated molecules. In the first two cases, a surfactant (Brij 56) or polyelectrolyte (PAA) is first adsorbed onto the CTAB layer. In the third method, the CTAB layer on the gold nanorod is exchanged with small ligand molecules, such as cystamine,[21] mercaptoundecanoic acid[22] or thiolated polyethylene glycols.[23] Additionally, thiolated proteins can directly bind to the gold nanorod surface via ligand exchange.[23] The drawback of all above methods is that a random site on the protein is conjugated to the gold surface, which could lead to some loss of the protein's function. Moreover, direct attachment of proteins via ligand exchange could even lead to protein denaturation on the gold surface.

4.2.3 Strategy for creating mapped random deposited sensors

To proof the concept of our novel multiplexed NanoSPR method, we deposit four batches of gold nanorods on our sensor substrate, three functionalized with different proteins P_1, P_2, P_3 and one non-functionalized as reference. By flowing in one batch at a time while recording the position of each randomly deposited nanoparticle, we know the specific functionalization for each particle on the sensor surface, thus effectively generating a position-encoded sensor, similar to a spotted array but without any geometrical order (Figure 4.1b).[24]

4.2.4 Detection principle of NanoSPR

The binding of a common target protein T to the previously deposited functionalized gold nanorods causes a shift in the plasmon wavelength $\Delta\lambda_{res}$ as schematically shown in Figure 4.1c. The plasmon shift of each single gold nanoparticle sensor is recorded by optical dark-field spectroscopy for every particle in the field of view, using a fully automated, temperature stable, user friendly and fast optical microscopy system optimized for spectral precision. This system allows routinely recording the response of hundreds of particles with a precision of about 0.3 nm. [24]

4.3 Experimental Results

In this section, the main results on simultaneous detection of multiple protein-protein interactions by optical dark-field microscopy will be presented.

4.3.1 Proof of concept of simultaneous bait-prey type protein interactions

We demonstrate our NanoSPR concept by studying the interaction of three bacterial division proteins (MinC and two soluble variants of ZipA, s1- and s2-ZipA, lacking its transmembrane domain - see Appendix B) with its target protein, FtsZ (a 40 kDa soluble GTPase, homolog of eukaryotic tubulin),[4, 5] an essential element of the division machinery of most bacterial systems. In *Eschericia coli*, FtsZ is anchored to the cytoplasmic membrane by the action of the membrane protein ZipA (a 36.4 kDa trans-membrane protein, containing the FtsZ binding-domain at the globular cytoplasmic C-terminal region)[25] and the amphitropic protein FtsA. Together they form the initial assembly of the division machinery (the proto-ring complex), which drives cytokinesis at midcell, where FtsZ polymers form a dynamic Z-ring active in division.[26] The MinCDE system, is one of the two control mechanisms that cooperate in the correct positioning of the division ring by inhibiting ring formation in wrong places. MinC is a 24 kDa protein that prevents FtsZ assembly.[27, 28]

To evaluate the binding affinities of these three interacting pairs (FtsZ-s1ZipA, FtsZ-s2ZipA and FtsZ-MinC), the sensor was exposed to solutions with increasing FtsZ concentrations, similar to the titration method described by Schuck.[29] FtsZ aliquots were flowed into the flow cell until the interaction with the sensors reached equilibrium.[7] After about 20 min, we recorded the wavelength shift $\Delta\lambda_{res}$ of about 200 particles, which gave about 30 to 50 data points for each interaction pair. Figure 4.2 shows the average plasmon shift $\Delta\lambda$ as a function of FtsZ concentration, *i.e.* the binding isotherms, for each of the three interacting pairs and the non-functionalized reference particles. The flat response of the reference particles demonstrated that unspecific interactions between the sensors and FtsZ are negligible.

4.3.2 Deciphering the K_D

The experimental data are well described by the Langmuir equation $\Delta\lambda /\Delta\lambda_{max} = c\ K_D/(1+c\ K_D)$, which allows us to extract the equilibrium dissociation constants K_D for each pair. The

values for the three interacting pairs are listed in Table 4.1 and are in excellent agreement with values previously obtained by composition-gradient static light scattering (CG-SLS), sedimentation equilibrium-analytical ultracentrifugation (SE-AUC), fluorescence anisotropy (FA)[30-32] or in independent titration measurements performed with the conventional SPR (Appendix B, Figure B4). In contrast to all other techniques, our NanoSPR results were obtained simultaneously on a single sensor, providing binding affinities for all three proteins and the reference.

Interacting proteins	NanoSPR	SPR	GC-SLS	SE-AUC	FA
FtsZ-s1ZipA	5.2 ± 0.2	5.4 ± 0.1	5.8 ± 0.1^{32}	5.4^{32}	-
FtsZ-s2ZipA	5.3 ± 0.1	5.3 ± 0.2	-	-	-
FtsZ-MinC	5.1 ± 0.1	5.0 ± 0.1	-	-	4.9 ± 0.1^{30}
FtsZ-ZipA wt	-	-	-	6.1 ± 0.5^{31}	-

Table 4.1. log K_D values obtained in present work by NanoSPR and SPR together with literature values determined by composition gradient-static light scattering (CG-SLS), sedimentation equilibrium-analytical ultracentrifugation (SE-AUC) and fluorescence anisotropy (FA).
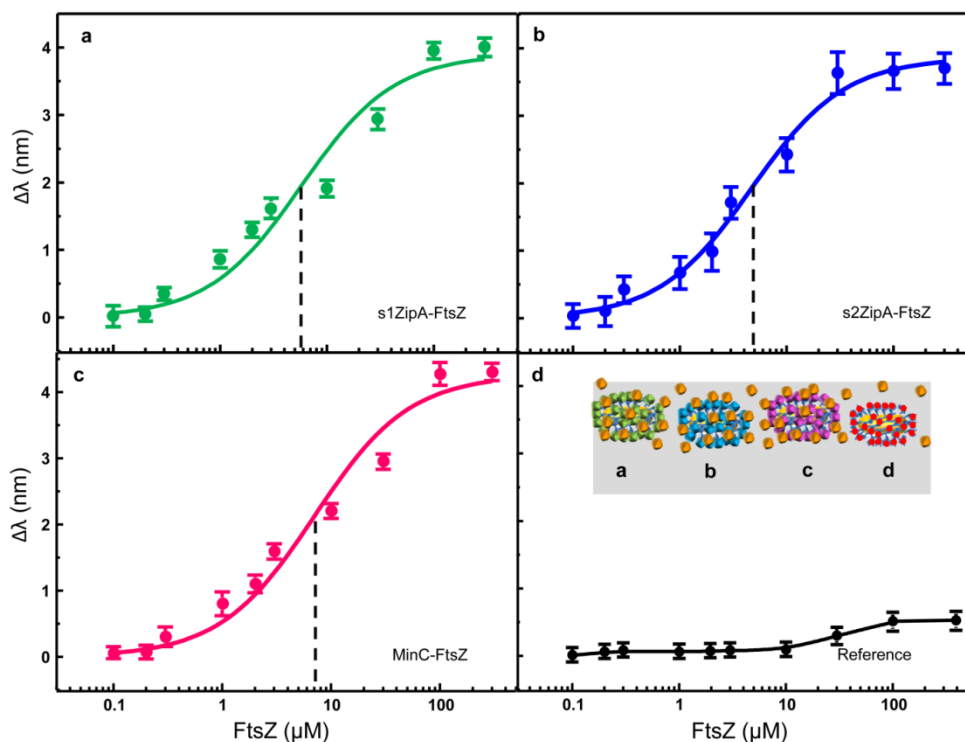
Figure 4.2. Binding affinity of multiple protein-protein interactions. The data points in the four subpanels correspond to the mean plasmon shift $\Delta\lambda_{res}$ measured on 20-50 nanoparticles covered by: a) s1-ZipA b) s2-ZipA c) MinC and d) no protein. The error bar indicates the standard error of the mean. The plasmon shifts $\Delta\lambda_{res}$ are measured for increasing concentrations of the target protein FtsZ (after equilibration) and obtained on a single NanoSPR sensor. The solid lines correspond to the best fit of a Langmuir equation to the experimental data, used to extract the K_D values listed in Table 4.1 (dashed lines).

4.3.3 Regeneration of Ni²⁺-NTA surface

Regeneration and reusability are important aspects of sensors. It is well known that NTA-Ni²⁺-His-tag complexes are easily broken up by adding an excess of the Ni²⁺-complexing imidazole. To demonstrate that this also works in case of the NanoSPR, we tested the removal of s1ZipA from Ni-NTA functionalized gold nanorods by washing with imidazole. Addition of s1ZipA to the nanorods leads to the expected plasmon shift $\Delta\lambda$, which fully reversed to its original position after washing with imidazole (Figure 4.3a). Repeating this cycle three times showed very little degeneration of the sensor. However, we should mention that a multiplexed sensor, containing groups of particles functionalized with different proteins, cannot be recycled in this way because subsequent protein addition will affect all particles simultaneously. More sophisticated orthogonal binding chemistry or microfluidic control of protein placement would be necessary to recycle multiplexed sensors. However, the fast and

simple fabrication process of our sensors by random deposition does, in our opinion, not make this effort worthwhile.
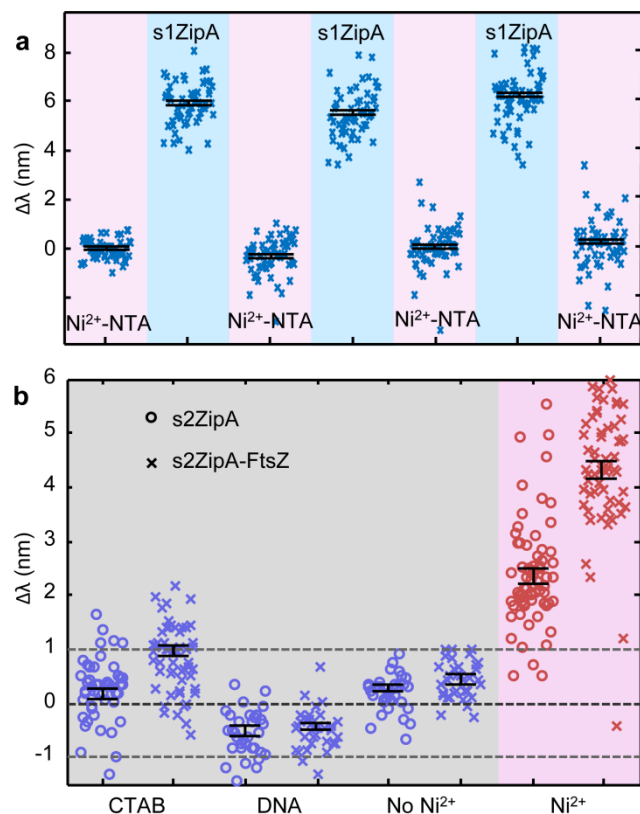
Figure 4.3. **Control experiments. a)** Sensor response after repeated incubation with s1ZipA (1 µM, light blue shaded areas) and imidazole (800 mM, pink shaded areas). The actual measurements were conducted, in both cases, in the same working buffer. Each small cross represents the response of an individual nanoparticle and the black symbols the median and its standard error for all 47 particles. The plasmon shift $\Delta\lambda_{res}$ reversed to its original value after each cycle. **b)** To demonstrate the power of the two-step functionalization strategy, we exposed four kinds of particles to the proteins. These particles where covered with: 1. CTAB, 2. DNA, 3. DNA+NTA, 4. DNA+NTA+Ni^{2+}. Upon addition of the His-tagged protein s2ZipA (0.5 µM) the last group showed the expected large plasmon shift, indicative of an efficient protein immobilization. The CTAB particles showed some smaller nonspecific affinity, whereas the DNA coating completely prevents unspecific protein binding. The fact that addition of FtsZ (2 µM) leads to an additional shift proves that s2ZipA maintains its FtsZ binding affinity after immobilization on the nanoparticle surface.

4.3.4 Assessment of binding specificity

To demonstrate the effectiveness of our two-step protein functionalization procedure, we expose four types of gold nanorods first to a protein with a His-tag (s2ZipA) and then to FtsZ: gold nanorods directly from synthesis (presumably with a CTAB layer), nanorods stabilized with DNA, and NTA functionalized nanorods in the absence and presence of Ni^{2+} ions. Only the NTA functionalized nanorods in the presence of Ni^{2+} ions show large plasmon shifts after

adding s2ZipA (Figure 4.3b), indicating the successful immobilization of s2ZipA via the His-tag. The gold nanorods used directly from synthesis show a small plasmon shift, presumably from unspecific adsorption of s2ZipA to the (more or less) unprotected gold surface. The DNA stabilization seems to protect the nanoparticles from this unspecific adsorption, as evident from the plasmon shifts. The fact that further addition of FtsZ leads to an additional plasmon shift only in the case of NTA functionalized gold nanorods in the presence of Ni^{2+} ions demonstrates that the immobilized s2ZipA maintains its FtsZ binding function.

4.4 Discussion

In this section, I will discuss about the about the scale-up considerations of our nanoSPR system. Furthermore, I will also mention about the potential applications of this method.

4.4.1 Key elements of our technique

Taking the results presented in Figure 4.2 and 4.3 together, we successfully demonstrated how NanoSPR provides a new and powerful tool for the parallel study of many macromolecular interactions. It is made possible by the combination of our fast and automated optical dark-field spectroscopy system with the flexible particle functionalization via His-tags. For this functionalization, it turned out to be important to first stabilize the gold nanorods with short DNA oligomers, which prevent aggregation in saline solutions.

4.4.2 Upscaling consideration

Assuming the availability of a large library of His-tagged proteins and an automated sensor fabrication process, we see no fundamental or practical limitations to extend the parallelization over at least 2 orders of magnitude. Currently, we have a maximum of 1000 particles or sensing elements in the field of view, which would limit the number of different proteins to study to 20-50. Considering that the field of view represents only a very small fraction of the actual flow cell device we use, a larger scan area could easily extend the number of investigated particles. The limitations of NanoSPR, regarding the measurable range of K_D values, should be equivalent to those for conventional SPR. At the lower end, it is limited by the measurement accuracy and the time needed to reach equilibrium. In our current system, the detection limit was estimated to be around 1 nM,[24] providing a lower limit of measurable K_D values one order of magnitude higher, *i.e.* with values of around 10 nM.[33] The

upper limit (for low affinity interactions) is difficult to estimate and should be limited mostly by the solubility of the target molecule. With regards to the limit to measure low molecular mass molecules, NanoSPR should have advantages over conventional SPR because the sensing volume is better matched to molecular dimensions.[34, 35] Tuning the nanorod dimensions affects the sensing volume can be used to optimize the NanoSPR sensors for either low or high molecular mass target molecules.[34]

4.4.3 NanoSPR as a potential tool for the future

We see at least three more possible advantages of NanoSPR compared to conventional SPR: the nanoscopic dimension of the sensing elements drastically reduces the problem of non-uniform surface functionalization across the SPR sensor surface,[7] drastically reduces the required sample volume, and provides a build-in statistics without the need to repeat the measurement. These advantages make NanoSPR a simple, fast and cost effective route to characterize binding affinities between many macromolecular partners simultaneously. We envision NanoSPR to be especially useful for the study of biochemical and biomedical processes *in vitro* and envision it to be useful for screening applications, *e.g.* for lead generation in the drug discovery process.

References

(1) Han, J.-D. J.; Bertin, N.; Hao, T.; Goldberg, D. S.; Berriz, G. F.; Zhang, L. V.; Dupuy, D.; Walhout, A. J. M.; Cusick, M. E.; Roth, F. P.; Vidal, M. *Nature* **2004,** 430, 88-93.

(2) Howell, J. M.; Winstone, T. L.; Coorssen, J. R.; Turner, R. J. *Proteomics* **2006,** 6, 2050-69.

(3) Pandey, A.; Mann, M. *Nature* **2000,** 405, 837-846.

(4) Erickson, H. P.; Anderson, D. E.; Osawa, M. *Microbiol. Mol. Biol. Rev.* **2010,** 74, 504-528.

(5) Mingorance, J.; Rivas, G.; Vélez, M.; Gómez-Puertas, P.; Vicente, M. *Trends Microbiol.* **2010,** 18, 348-356.

(6) Vicente, M.; Rico, A. I. *Mol. Microbiol.* **2006,** 61, 5-8.

(7) Schuck, P. *Annu. Rev. Biophys. Biomol. Struct.* **1997,** 26, 541-566.

(8) Fee, C., *Methods Mol. Biol.* **2013**, 996, 313-322.

(9)   Bleicken, S.; Otsuki, M.; García-Sáez, A. J. *Curr. Protein Pept. Sci.* **2011,** 12, 691-8.

(10)   Velázquez-Campoy, A.; Leavitt, S. A.; Freire, E. *Methods Mol. Biol.* **2004,** 261, 35-54.

(11)   Howlett, G. J.; Minton, A. P.; Rivas, G. *Curr. Opin. Chem. Biol.* **2006,** 10, 430-6.

(12)   Knezevic, J.; Langer, A.; Hampel, P. A.; Kaiser, W.; Strasser, R.; Rant, U. *J. Am. Chem. Soc.* **2012,** 134, 15225-8.

(13)   Homola, J.; Vaisocherová, H.; Dostálek, J.; Piliarik, M. *Methods* **2005,** 37, 26-36.

(14)   Washburn, A. L.; Bailey, R. C. *Analyst* **2011,** 136, 227-236.

(15)   Anker, J. N.; Hall, W. P.; Lyandres, O.; Shah, N. C.; Zhao, J.; Van Duyne, R. P. *Nat. Mat.* **2008,** 7, 442-53.

(16)   McFarland, A. D.; Van Duyne, R. P. *Nano Lett.* **2003,** 3, 1057-1062.

(17)   Sönnichsen, C.; Franzl, T.; Wilk, T.; von Plessen, G.; Feldmann, J.; Wilson, O.; Mulvaney, P. *Phys. Rev. Lett.* **2002,** 88, 077402-(1-4).

(18)   Ahijado-Guzmán, R.; Gómez-Puertas, P.; Alvarez-Puebla, R. A.; Rivas, G.; Liz-Marzán, L. M. *ACS Nano* **2012,** 6, 7514-20.

(19)   Wang, Y.; Tang, L.-J.; Jiang, J.-H. *Anal. Chem.* **2013,** 85,, 9213-9220.

(20)   Wang, J.; Dong, B.; Chen, B.; Jiang, Z.; Song, H. *Dalton Trans.* **2012,** 41, 11134-11144.

(21)   Singh, A. K.; Senapati, D.; Wang, S.; Griffin, J.; Neely, A.; Candice, P.; Naylor, K. M.; Varisli, B.; Kalluri, J. R.; Ray, P. C. *ACS Nano* **2009,** 3, 1906-1912.

(22)   Yu, C.; Nakshatri, H.; Irudayaraj, J. *Nano Lett.* **2007,** 7, 2300-2306.

(23)   Joshi, P. P.; Yoon, S. J.; Hardin, W. G.; Emelianov, S.; Sokolov, K. V. *Bioconjug. Chem.* **2013,** 24, 878-888.

(24)   Rosman, C.; Prasad, J.; Neiser, A.; Henkel, A.; Edgar, J.; Sönnichsen, C. *Nano Lett.* **2013,** 13, 3243-3247.

(25)   Ohashi, T.; Hale, C. A.; de Boer, P. A.; Erickson, H. P. *J. Bacteriol.* **2002,** 184, 4313-5.

(26)   Rico, A. I.; Krupka, M.; Vicente, M. *J.Biol. Chem.* **2013,** 288, 20830-6.

(27)   Dajkovic, A.; Lan, G.; Sun, S. X.; Wirtz, D.; Lutkenhaus, J. *Curr. Biol.* **2008,** 18, 235-44.

(28)   Hu, Z.; Mukherjee, A.; Pichoff, S.; Lutkenhaus, J. *Proc. Nat. Ac. Sci.USA* **1999,** 96, 14819-24.

(29)   Schuck, P.; Millar, D. B.; Kortt, A. A. *Anal. Biochem.* **1998,** 265, 79-91.

(30)   Hernández-Rocamora, V. M.; García-Montanés, C.; Reija, B.; Monterroso, B.; Margolin, W.; Alfonso, C.; Zorrilla, S.; Rivas, G. *J. Biol. Chem.* **2013,** 288, 24625-35.

(31)   Hernández-Rocamora, V. M.; Reija, B.; García, C.; Natale, P.; Alfonso, C.; Minton, A. P.; Zorrilla, S.; Rivas, G.; Vicente, M. *J. Biol. Chem.* **2012,** 287, 30097-104.

(32)   Martos, A.; Alfonso, C.; López-Navajas, P.; Ahijado-Guzmán, R.; Mingorance, J.; Minton, A. P.; Rivas, G. *Biochemistry* **2010,** 49, 10780-7.

(33)   Tellinghuisen, J. *Anal. Biochem.* **2012,** 424, 211-220.

(34)   Ament, I.; Prasad, J.; Henkel, A.; Schmachtel, S.; Sonnichsen, C. *Nano Lett.* **2012,** 12, 1092-5.

(35)   Otte, M. A.; Sepúlveda, B.; Ni, W.; Juste, J. P.; Liz-Marzán, L. M.; Lechuga, L. M. *ACS Nano* **2009,** 4, 349-357.

Chapter 5

Plasmonic Core-satellites as Highly Sensitive Refractive Index Sensors

Highly sensitive and spectrally tunable plasmonic nanostructure is of great demand for applications such as SERS and parallel biosensing. However, there is a lack of such nanostructures for the mid-visible spectral regions as most available nanostructures offer high sensitivity in red to far red spectrum. In this work, I developed a novel strategy for synthesising core-satellite nanoparticles in high yield. The formation of highly sensitive nanoparticle structures takes place via a hydroxylamine mediated core-satellite assembly of 20nm gold nanoparticle satellites onto 60 nm spherical gold cores. Using various concentrations of hydroxylamine, I hereby demonstrate fine tuning of number of satellites per core. report The average number of satellites allows tuning the plasmon resonance wavelength from 543 to 575 nm. Last but not the least, I deciphered the mechanism of core-satellite assembly and characterised these nanostructures to demonstrate their pH stability and a two-fold higher sensitivity than similar sized gold nanospheres.

This work resulted from a collaboration with Inga Zins, Robert Branscheid, and Jan Becker and is submitted as 'Plasmonic Core-satellites Assemblies As Highly Sensitive Refractive Index Sensors' in The Journal of Physical Chemistry C.

5.1 Introduction

Gold nanoparticles have been exploited as novel nanoscopic sensor elements in recent years, both in surface enhanced Raman scattering (SERS),[1] and plasmon shift based refractometric sensors.[2,3] For the latter, refractive index changes Δn in the nanoparticle environment are detected via the induced plasmon resonance shift $\Delta\lambda$.[4] Finding highly sensitive metal nanostructures (with large values of $S_\lambda = \Delta\lambda/\Delta n$) has been an area of importance in this field. High sensitivity can be achieved by tailoring the size and shape of particles, using for example nanospheres, nanocubes, bipyramids and nanorods[5,6] or more complex geometries such as nanobranches,[7] nanorattles,[8] nanoshells,[9] nanoflowers,[10] and nanotubes.[11] However, the plasmon resonances of most of the above structures are in the red to NIR region of the electromagnetic spectrum. For some applications (e.g. multiplexing),[12] it is desirable to have plasmonic structures with high sensitivity in the mid-visible (green to red) part of the

spectrum. Here we show a novel strategy for batch synthesis of core-satellites structures that offer high sensitivity in the mid-visible. The core-satellite structures are nearly two-fold more sensitive than gold nanospheres alone. Its refractive index sensitivity is also notably higher than gold nanocubes (λ_{max}=538 nm).[5] Moreover, the resonance wavelength of core-satellites can be tuned from 543 nm to 575 nm by adjusting the number of satellites. These nanostructures will be useful for various plasmonic applications like SERS,[13] multiplexed analyte detection[14] and colorimetric sensing.[15]

5.1.1 Challenges in nanoparticle assembly

Controlled assembly of gold nanoparticles into dimers,[16] trimers[17] and core-satellites[18,19] is an effective means to increase[20] their Raman scattering enhancement by a factor of 10^8-10^{11}. The accepted reason is that these nanostructures have sharper apexes and a gap which allow a large part of the plasmon field to penetrate the dielectric environment.[8] The same mechanism should improve the plasmonic sensitivity S_λ of core-satellites. The number of hot spots and the resonance position of core-satellites can be tuned by varying the satellite number, core and satellite size and the interparticle distance.[21,22] Sensitivity of core-satellites is inversely related to the coupling distance between the core and the satellites.[21] Conventionally, DNA has been used as a molecule of choice for creating core-satellite nanostructures.[20,23,24] Since DNA sequences used in these cases require a certain minimal length to ensure proper base pairing, the intra-assembly gap distances reaches tens of nanometers. Moreover, the distances between core and satellites are difficult to specify due to non-specific adsorption of nitrogenous bases of DNA onto gold nanoparticles.[25] Other small molecules[15,18] have been shown to assemble core-satellites onto a substrate, but in solution phase batch synthesis, these molecules produce low yield of core-satellites. Recently, p-aminothiophenol has been used to electrostatically drive the formation of core-satellites in solution.[26] These assemblies have much shorter gap distances, but they have a tendency to destabilize at near neutral or higher pH.

5.2 Experimental Results

In this section, the main results on synthesis and optical characterization of core-satellites will be presented.

5.2.1 Our Nanoassembly Approach

In our approach, we deposit 20 nm citrate capped gold nanosphere satellites on methoxy-PEG functionalized 60 nm gold nanosphere cores (Figure 5.1). The process contains a long co-incubation period followed by the addition of hydroxylamine (see materials and methods section, Appendix C). Shortly after the hydroxylamine addition, the core-satellite assemblies have formed in high yield (>98%, see TEM image in Figure 5.1c). The mechanism of assembly involves charge neutralization of citrate coated spheres with hydroxylamine, causing these particles to partially lose their colloidal stability and subsequent adsorption onto the methoxy-PEG functionalized core particles (see Figure C1, Appendix C). This simple approach for the batch synthesis of core-satellite nanostructures in high yield avoids many of the above mentioned complications.
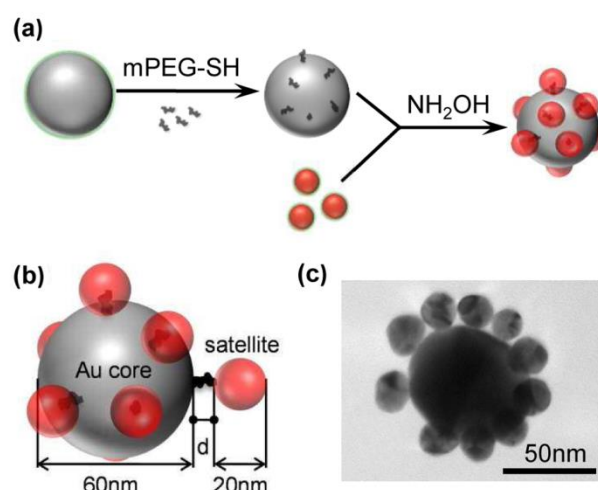
Figure 5.1. (a) Schematics of core-satellite formation procedure (b) The citrate stabilised 20nm satellite nanospheres are attached to PEGylated 60nm gold core with a gap distance *d* (c) Representative TEM image of the assembled structure.

5.2.2 Narrow Gap Distances in core-satellites

The satellites should bind at random sites on the PEG layer around the core-particles. However, traditional TEM images (as in Figure 5.1b) of dried samples typically showed a 'flower-like' pattern due to the collapse of the PEG shell upon drying. To observe the arrangement as it is present in solution, we used cryo-TEM, where a thin layer of the solution is so rapidly frozen that the native structure is preserved. Figure 5.2 shows TEM images obtained on such a frozen sample under various tilt angles. The cryo-images in Figure 5.2 conclusively demonstrate that the actual structure in solution is indeed a random arrangement

of satellites around a core particle. Furthermore, we observed a clear spacing (of ~ 7 nm) between satellites and cores (contrary to the collapsed 'flower' structures). Because the Cryo-TEM images show a projection of the randomly oriented satellites, the end to end gap distances shown in Figure 5.2a are only a lower limit to the actual distances. However, by tilting an individual assembly over a wide range of angles, we could demonstrate that even satellites appearing to touch the core in one projection are actually spaced some distance apart (see Figure 5.2c-h).
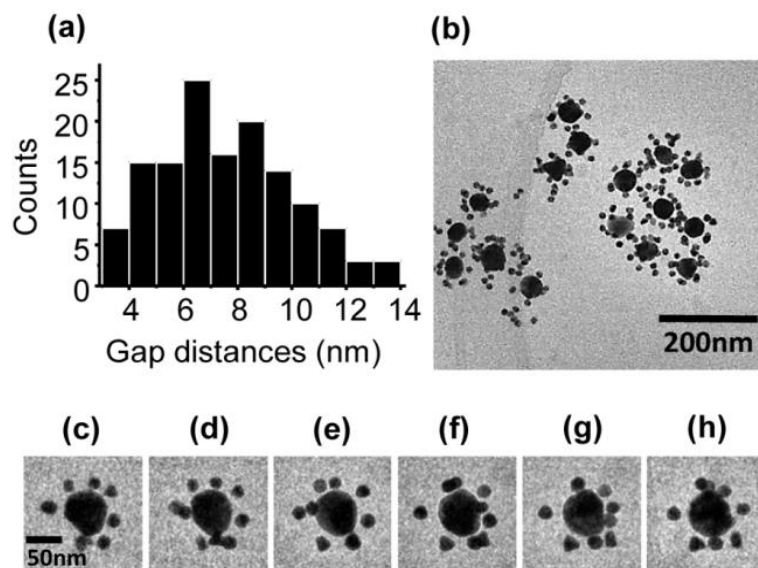
Figure 5.2. (a) Histogram of (projected) gap distances d between satellites and cores measured on Cryo-TEM images (b) at a fixed tilt angle. A single nanostructure is imaged at different tilt angles (c-h) demonstrating that even satellites appearing almost touching in one projection actually sit at a distance from the core.

5.2.3 Tuning resonance maxima of assembly

The average number of satellites per core particle can be precisely tuned by varying the concentration of hydroxylamine. Technically, it is much easier to adjust the concentration of hydroxylamine than the concentrations of nanoparticles (core or satellites) because their concentration can only be estimated indirectly. Final hydroxylamine concentrations of 70 µM, 105 µM and 140 µM lead to an average of 3, 7 and 8 satellites per core (Figure 5.3a) as determined by TEM (Figure 5.3b-d). The yield of core-satellites was >98 % (Figure 5.3a). The last value (8) is only a lower limit because not all satellites could be counted due to core-satellite-core fusion. For the highest hydroxylamine concentration (Figure 5.3d), we observed a considerable amount of uncontrolled clustering that made us cautious to use even higher hydroxylamine concentrations. The corresponding optical resonance maxima (λ_{max}) are at 543 nm, 551 nm and 575 nm respectively (Figure 5.3e). The observed trend (higher spectral shift

on increasing numbers of satellites) is expected because of increased plasmon coupling. Apart from the plasmon resonance maxima, the electrophoretic mobility of the core-satellites also depends on the number of satellites (Figure 5.3f). For higher the number of satellites, the mobility decreases as expected from the combined effect of surface charge neutralization and increasing size.[27] The gel electrophoresis experiments demonstrated the stability and robustness of the core-satellite nanostructures within the pH range of 5-9 and high ionic strength.
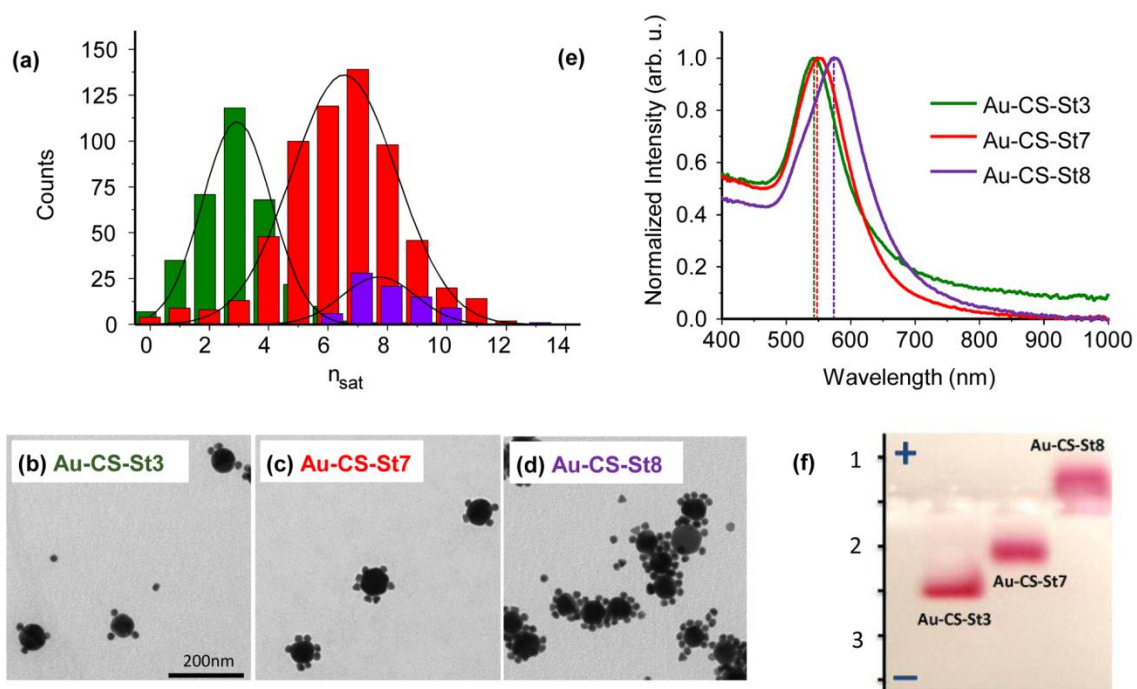
Figure 5.3. (a) Histogramm of the number of satellites per core. A Gaussian fit of the distribution leads to a median number of 3, 7, and 8 (in the last case, all satellites could not be counted due to significant levels of core-satellite-core fusion) satellites per core for Au-CS-St3 (green), Au-CS-St7 (red) and Au-CS-St8 (violet), respectively. (b-d) Electron-microscopy images of typical core-satellite samples (all images have the same magnification). (e) Ensemble-Spectra of the different core-satellite assemblies with increasing satellite number showing the red-shift with increasing number of satellites. (f) Agarose gel-electrophoresis (0.3% agarose, 0.5x TBE, 150V, 30 minutes) of 60nm mPEG-coated spheres and three core-satellite preparations showing the lower mobility of assemblies with larger number of satellites.

5.2.4 Demonstration of Core-satellite sensitivity

Our motivation to make core-satellite gold nanoparticle structures was their potential use as plasmon sensors. One of the most important parameters characterizing plasmon nanosensors is their sensitivity to refractive index changes in the surrounding. The sensitivity S_λ is defined as the shift in the plasmon resonance wavelength $\Delta\lambda_{res}$ per unit change in the surrounding

refractive index Δn ($S_\lambda = \Delta\lambda_{res}/\Delta n$). We measured the sensitivity S_λ for 60nm cores, 80nm cores and core satellite structures (with 60nm cores and an average of 7 satellites with 20nm diameter) by systematically changing the solvent refractive index using a water-glycerol mixture (Figure 5.4a). The sensitivity of 60nm cores was much lower (112 nm/RIU) than the sensitivity for core-satellite structures with the same core (188 nm/RIU). It is well known that plasmon sensitivity increases with resonance wavelength.[28] Due to this fact, we also included 80nm cores that show approximately the same resonance wavelength (see Figure C2, Appendix C). However, their plasmon sensitivity S_λ was only 134 nm/RIU, still lower than the core-satellite structure. The core-satellites also demonstrate a two-fold higher sensitivity than gold nanocubes ($S_\lambda = 83$).[5]
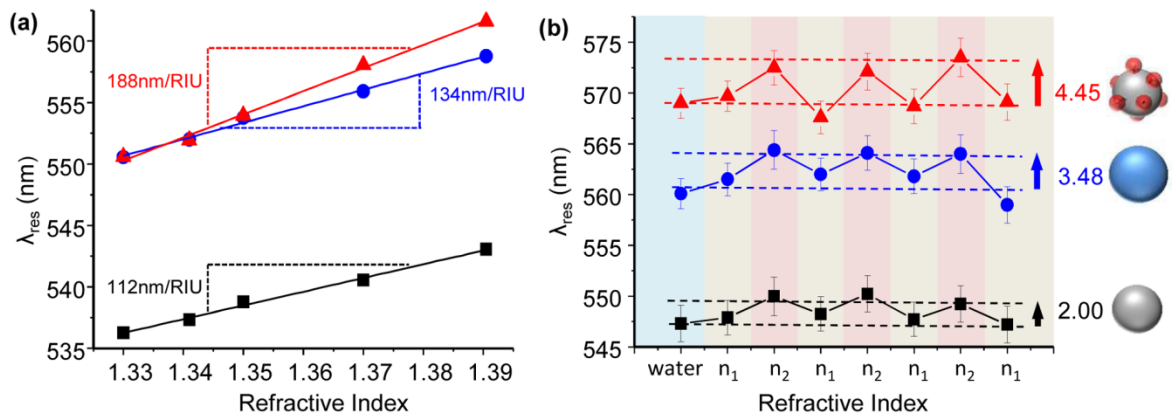
Figure 5.4. (a) Ensemble resonance position of 60nm cores (black), 80nm cores (blue) and core satellite assemblies (Au-CS-St7, red) in different refractive index media. The slope of the linear fit corresponds to the ensemble sensitivity of 112, 134, and 188nm/RIU respectively. (b) Median resonance position from single-particle measurements of 60nm cores (black), 80nm cores (blue) and Au-CS-St7 (red) in refractive index media 1.34 (n_1) and 1.38 (n_2). The shift of the resonance wavelength shows good reversibility. The median shifts are 2.00, 3.48 and 4.45nm. The error bars represent the standard deviation of the spectral shift observed in the resonance position of 30 different particles.

5.2.5 Hydrodynamic radius Vs Solvent medium

To make sure that a solvent mediated collapse of the intermediate PEG layer is not the reason for the observed plasmon shift of core-satellite structures when adding glycerol, we measured both the hydrodynamic radius (R_h) and rotational radius (R_r) of 60nm cores in different water-glycerol mixtures with polarized and depolarized photon correlation spectroscopy, respectively,[29] the latter is more sensitive to possible conformational change of PEG layer due to the R_r^3 dependence of the rotational diffusion. When correcting for the

measured viscosity of the solvent, no significant glycerol dependent change in the hydrodynamic radius was observed (see Figure C3 and Table C1, Appendix C).

5.2.6 Reversibility of sensor

One of the most promising applications of plasmon sensors is their use in single nanoparticle experiments. In such experiments, the extremely small sensing volume is taken advantage of in an optimal way. To investigate if the above results hold true for single particle measurements, we investigated the plasmon sensitivity for the same three samples as above on single particles immobilized inside of a glass capillary. The immobilization allows a repeated change of the surrounding solution (from n=1.34 to n=1.38 and back) – something we found generally to be very important when determining plasmon sensitivity as reversible effects due to changes in the environment can be discriminated from irreversible shifts caused by changes to the particles themselves.[30] In this case, however, the shifts were fully reversible, which allows to extract meaningful plasmon sensitivity values (Figure 5.4b and Figure C4). The average values obtained on about 30 nanoparticles per sample are slightly smaller than that for ensemble measurements as expected from the partial blocking of the particle surrounding by the substrate. The extracted values are $\Delta\lambda_{res}$=2.00±0.34nm, $\Delta\lambda_{res}$=3.48±0.55nm, and $\Delta\lambda_{res}$=4.45±1.97nm yielding sensitivities and figure of merit (FOM=S_λ/plasmon linewidth) as summarized in Table 5.1. The increase in the FOM for core-satellites reflects the increase in plasmon sensitivity and almost unchanged plasmon linewidth (FWHM) of the 60nm cores after assembly with the satellites.

Table 5.1. Plasmon sensitivities S_λ and figure of merit (FOM) for the core-satellite structures compared to PEGylated cores.

Nanostructure type	S_λ (ensemble)	S_λ (single particles)	FOM (single particles)
60nm cores	112	50 ± 8.5	0.69
80nm cores	134	87 ± 13.7	0.99
60nm core – 20nm satellite	188	111 ± 49	1.80

5.3 Conclusion

In both cases, ensemble and single particle measurements, the plasmonic sensitivity of core-satellite structures proved to be larger than that of similar sized spherical particles (with comparable spectral position). We believe that the enhanced sensitivity results from a larger part of the electromagnetic field connecting the induced surface charges penetrating the surrounding environment accessible to the solvent molecules – similar to the case of hollow nanorattles reported before.[8] The advantage of core-satellite structures to other high sensitivity plasmon sensors is their relatively straight forward assembly that allows a simple fine-tuning of the desired resonance wavelength by adjusting the average number of satellites. Another potential advantage is the possibility to include responsive polymers as linkers which would drastically enhance the spectrum of measureable parameters (for example temperature, pH, specific ligands, and ions). Potentially, our assembly route could be extended to nanoparticles with different materials, for example using magnetic nanoparticles,[31] for multiplexed labelling, drug delivery, SERS enhancement or completely novel physical effects.

References

1. Haes, A. J.; Haynes, C. L.; McFarland, A. D.; Schatz, G. C.; Van Duyne, R. P.; Zou, S., Plasmonic Materials for Surface-Enhanced Sensing and Spectroscopy. *MRS Bulletin* **2005**, *30*, 368-375.

2. Anker, J. N.; Hall, W. P.; Lyandres, O.; Shah, N. C.; Zhao, J.; Van Duyne, R. P., Biosensing with plasmonic nanosensors. *Nat Mater* **2008**, *7*, 442-453.

3. Jain, P.; Huang, X.; El-Sayed, I.; El-Sayed, M., Review of Some Interesting Surface Plasmon Resonance-enhanced Properties of Noble Metal Nanoparticles and Their Applications to Biosystems. *Plasmonics* **2007**, *2*, 107-118.

4. Mock, J. J.; Smith, D. R.; Schultz, S., Local Refractive Index Dependence of Plasmon Resonance Spectra from Individual Nanoparticles. *Nano Letters* **2003**, *3*, 485-491.

5. Chen, H.; Kou, X.; Yang, Z.; Ni, W.; Wang, J., Shape- and Size-Dependent Refractive Index Sensitivity of Gold Nanoparticles. *Langmuir* **2008**, *24*, 5233-5237.

6. Lee, K.-S.; El-Sayed, M. A., Gold and Silver Nanoparticles in Sensing and Imaging: Sensitivity of Plasmon Response to Size, Shape, and Metal Composition. *The Journal of Physical Chemistry B* **2006**, *110*, 19220-19225.

7. Chen, H.; Shao, L.; Woo, K. C.; Ming, T.; Lin, H.-Q.; Wang, J., Shape-Dependent Refractive Index Sensitivities of Gold Nanocrystals with the Same Plasmon

Resonance Wavelength. *The Journal of Physical Chemistry C* **2009**, *113*, 17691-17697.

8. Khalavka, Y.; Becker, J.; Sönnichsen, C., Synthesis of Rod-Shaped Gold Nanorattles with Improved Plasmon Sensitivity and Catalytic Activity. *Journal of the American Chemical Society* **2009**, *131*, 1871-1875.

9. Jain, P. K.; El-Sayed, M. A., Surface Plasmon Resonance Sensitivity of Metal Nanostructures: Physical Basis and Universal Scaling in Metal Nanoshells. *The Journal of Physical Chemistry C* **2007**, *111*, 17451-17454.

10. Xie, J.; Zhang, Q.; Lee, J. Y.; Wang, D. I. C., The Synthesis of SERS-Active Gold Nanoflower Tags for In Vivo Applications. *ACS Nano* **2008**, *2*, 2473-2480.

11. Zhu, J.; Deng, X.-c., Improve the refractive index sensitivity of gold nanotube by reducing the restoring force of localized surface plasmon resonance. *Sensors and Actuators B: Chemical* **2011**, *155*, 843-847.

12. Yu, C.; Irudayaraj, J., Multiplex Biosensor Using Gold Nanorods. *Analytical Chemistry* **2006**, *79*, 572-579.

13. Zheng, Y.; Thai, T.; Reineck, P.; Qiu, L.; Guo, Y.; Bach, U., DNA-Directed Self-Assembly of Core-Satellite Plasmonic Nanostructures: A Highly Sensitive and Reproducible Near-IR SERS Sensor. *Advanced Functional Materials* **2013**, *23*, 1519-1526.

14. Rosman, C.; Prasad, J.; Neiser, A.; Henkel, A.; Edgar, J.; Sönnichsen, C., Multiplexed Plasmon Sensor for Rapid Label-Free Analyte Detection. *Nano Letters* **2013**, *13*, 3243-3247.

15. Waldeisen, J. R.; Wang, T.; Ross, B. M.; Lee, L. P., Disassembly of a Core−Satellite Nanoassembled Substrate for Colorimetric Biomolecular Detection. *ACS Nano* **2011**, *5*, 5383-5389.

16. Sonnichsen, C.; Reinhard, B. M.; Liphardt, J.; Alivisatos, A. P., A molecular ruler based on plasmon coupling of single gold and silver nanoparticles. *Nat Biotech* **2005**, *23*, 741-745.

17. Wustholz, K. L.; Henry, A.-I.; McMahon, J. M.; Freeman, R. G.; Valley, N.; Piotti, M. E.; Natan, M. J.; Schatz, G. C.; Duyne, R. P. V., Structure−Activity Relationships in Gold Nanoparticle Dimers and Trimers for Surface-Enhanced Raman Spectroscopy. *Journal of the American Chemical Society* **2010**, *132*, 10903-10910.

18. Yoon, J. H.; Lim, J.; Yoon, S., Controlled Assembly and Plasmonic Properties of Asymmetric Core–Satellite Nanoassemblies. *ACS Nano* **2012**, *6*, 7199-7208.

19. Wang, C.; Du, Y.; Wu, Q.; Xuan, S.; Zhou, J.; Song, J.; Shao, F.; Duan, H., Stimuli-responsive plasmonic core-satellite assemblies: i-motif DNA linker enabled intracellular pH sensing. *Chemical Communications* **2013**, *49*, 5739-5741.

20. Gandra, N.; Singamaneni, S., "Clicked" plasmonic core-satellites: covalently assembled gold nanoparticles. *Chemical Communications* **2012**, *48*, 11540-11542.

21. Ross, B. M.; Waldeisen, J. R.; Wang, T.; Lee, L. P., Strategies for nanoplasmonic core-satellite biomolecular sensors: Theory-based Design. *Applied Physics Letters* **2009**, *95*, -.

22. Xu, L.; Hao, C.; Yin, H.; Liu, L.; Ma, W.; Wang, L.; Kuang, H.; Xu, C., Plasmonic Core–Satellites Nanostructures with High Chirality and Bioproperty. *The Journal of Physical Chemistry Letters* **2013**, *4*, 2379-2384.

23. Chou, L. Y. T.; Zagorovsky, K.; Chan, W. C. W., DNA assembly of nanoparticle superstructures for controlled biological delivery and elimination. *Nat Nano* **2014**, *9*, 148-155.

24. Sebba, D. S.; Lazarides, A. A., Robust Detection of Plasmon Coupling in Core-Satellite Nanoassemblies Linked by DNA. *The Journal of Physical Chemistry C* **2008**, *112*, 18331-18339.

25. Wang, Z.; Zhang, J.; Ekman, J. M.; Kenis, P. J. A.; Lu, Y., DNA-Mediated Control of Metal Nanoparticle Shape: One-Pot Synthesis and Cellular Uptake of Highly Stable and Functional Gold Nanoflowers. *Nano Letters* **2010**, *10*, 1886-1891.

26. Gandra, N.; Abbas, A.; Tian, L.; Singamaneni, S., Plasmonic Planet–Satellite Analogues: Hierarchical Self-Assembly of Gold Nanostructures. *Nano Letters* **2012**, *12*, 2645-2651.

27. Hanauer, M.; Pierrat, S.; Zins, I.; Lotz, A.; Sönnichsen, C., Separation of Nanoparticles by Gel Electrophoresis According to Size and Shape. *Nano Letters* **2007**, *7*, 2881-2885.

28. Becker, J.; Trügler, A.; Jakab, A.; Hohenester, U.; Sönnichsen, C., The Optimal Aspect Ratio of Gold Nanorods for Plasmonic Bio-sensing. *Plasmonics* **2010**, *5*, 161-167.

29. Koch, A. H. R.; Lévêque, G.; Harms, S.; Jaskiewicz, K.; Bernhardt, M.; Henkel, A.; Sönnichsen, C.; Landfester, K.; Fytas, G., Surface Asymmetry of Coated Spherical Nanoparticles. *Nano Letters* **2014**, *14*, 4138-4144.

30. Jakab, A.; Rosman, C.; Khalavka, Y.; Becker, J.; Trügler, A.; Hohenester, U.; Sönnichsen, C., Highly Sensitive Plasmonic Silver Nanorods. *ACS Nano* **2011**, *5*, 6880-6885.

31. Schladt, T. D.; Shukoor, M. I.; Schneider, K.; Tahir, M. N.; Natalio, F.; Ament, I.; Becker, J.; Jochum, F. D.; Weber, S.; Köhler, O.; Theato, P.; Schreiber, L. M.; Sönnichsen, C.; Schröder, H. C.; Müller, W. E. G.; Tremel, W., Au@MnO Nanoflowers: Hybrid Nanocomposites for Selective Dual Functionalization and Imaging. *Angewandte Chemie International Edition* **2010**, *49*, 3976-3980.

32. Becker, J.; Schubert, O.; Sönnichsen, C., Gold Nanoparticle Growth Monitored in situ Using a Novel Fast Optical Single-Particle Spectroscopy Method. *Nano Letters* **2007**, *7*, 1664-1669.

Chapter 6

Plasmonic Gold Dimers for Probing Single Molecule Conformational Dynamics

Substantial progress has been made in our understanding of cellular and molecular function by recent advances in single molecule methods. Exploration of single molecules can provide essential new information on molecular properties normally disguised in inhomogeneous distributions of an ensemble. Current techniques to monitor molecular dynamics rely on fluorophores, which despite being accurate and effective do not allow long term investigation of molecule of interest. In this chapter, I present a novel technique that utilises plasmon based rulers to detect conformational dynamics in single proteins with millisecond temporal resolution.The technique involves continuous real-time monitoring of spectral shifts in plasmonic dimers due to inherent Hsp90 activity by dark-field spectroscopy. In this work, I developed the functionalisation strategy for specifically binding Hsp90 to gold nanospheres. I also improvised glass surface functionalisation protocols for efficient dimer formation in microfluidic flow channel. With these improvements I successfully demonstrated conformational dynamics Hsp90 tethered gold nanodimers due to thermal fluctuations in the protein. I also used this plasmon ruler concept to demonstrate effect of ionic concentration on ss DNA. Our technique could potentially be used in other applications such as, to study mechanism of action of molecules (in presence of cochaperones, drugs and inhibitors) and biomolecular heterogeneity within a population.

This work resulted from a collaboration with Andreas Henkel, Markus Götz, Prof. Thörsten Hügel, Karl Wandner, Laura Mann and Sebastian Schmachtel and aims at exploring the conformational dynamics of biomolecules (such as Hsp90).

5.1 Introduction

To expand our horizon on understanding cellular processes, it is imperative to explore the dynamic-function relationships[1] of participatory biomolecules. Single molecule methods could help in obtaining interesting new information which are otherwise lost or averaged out in ensemble measurements. Commonly used techniques to explore single protein

dynamics include, single molecule FRET (sm-FRET),[2] optical tweezers,[3] mass spectroscopy (HX-MS),[4] electron spin resonance (EPR)[5] and sum frequency generation spectroscopy (SFG).[6] These methods suffer from the inability to capture protein dynamics over long hours. Moreover, time consuming and extensive multiple labelling[7] with dyes/heavy isotopes for large proteins in order to obtain finer details on dynamics. Here we show a simple system based on Hsp90 linked gold nanodimers for long term investigation of nucleotide-free N-terminal conformational dynamics in heat shock protein Hsp90. In this work, plasmonic nanodimers consisting of a single Hsp90 molecule in the gap between two gold nanospheres were produced on flow cell surface. Conformational dynamics in Hsp90 was investigated over half hour duration and longer. The preliminary results show that the protein spends more time in its open states and is in good agreement with FRET studies done on Hsp90. The dimer formation strategy will be useful for studying protein dynamics, in general, and obtain new information on response of the protein to specific cellular signals,[8] interacting partners,[9, 10] environmental perturbations or drug intervention.[7] Plasmonic dimers may also aid other applications where uninterrupted long term monitoring is required like studying cascade reactions in cellular processes,[11] long term effect of a drug on protein[7, 12] or processivity of enzymes.[13]

5.2 Our Plasmon Ruler System
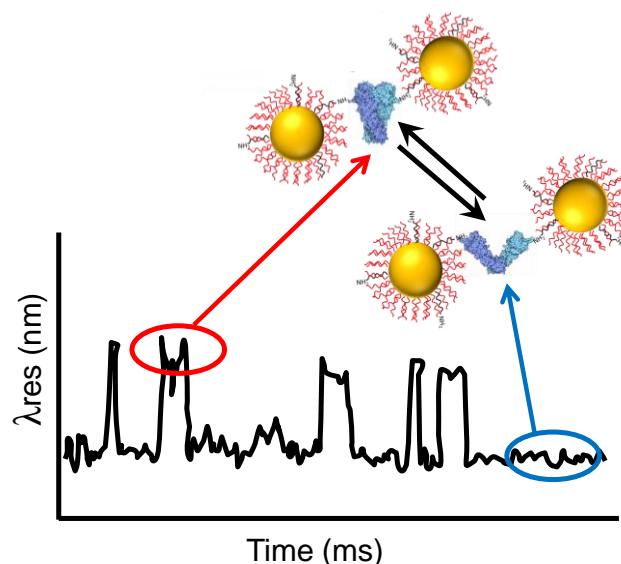
**Figure 6.1** Schematic showing working principle of Hsp90 based plasmon ruler.

Our technique makes use of plasmon coupling within dimers of gold nanospheres to study protein dynamics (Figure 6.1). The surface of gold nanoparticles was functionalised with

protein repellent layer to avoid unfavourable protein-nanoparticle interactions (such as protein unfolding, unspecific protein corona formation etc). We utilize PEG functionalised 40 nm gold spheres harbouring thiol reactive maleimide residues as building blocks for dimer formation. Genetically engineered heat shock protein 90 (containing free cysteines at both their N-terminus) is reacted to the maleimide-PEG functionalised particles in batch. The maleimide-thiol chemistry[14] is a well-known technique in protein chemistry, used to tag the protein with ligands and other proteins *in vitro*. Dimerisation of nanoparticles is favoured only when the cysteine at the other N-terminal of Hsp90 is accessible for the next incoming maleimide-PEG functionalised particles. For our experiments, the Hsp90 functionalized particles are first immobilized in a passivated glass capillary. Dimers are formed by incubating the immobilised particles in the surrounding medium highly enriched with maleimide-PEG functionalised gold spheres. This plasmon ruler system is analogous to dye labelled proteins used in FRET measurements.[15] However in contrast to fluorophores, the nanoparticle surface area is multiple order of magnitude larger and can potentially attract several proteins.[16] Therefore, in pursuit to minimise the number of protein per particle to a limit of one protein per particle, the maleimide PEG layer density was optimised (see materials and methods section, Appendix D). The dimers were investigated with dark-field microscopy[17] at 100 ms temporal resolution to detect nucleotide-free thermal fluctuations in Hsp90 protein.

5.2.1 The Detection Principle

Plasmonic dimers respond to changes in interparticle separation by expressing a spectral shift in their resonance maxima and large changes in scattering intensity. These shifts are caused due to plasmon coupling between the participating monomers.[18] In a plasmon ruler, the plasmon coupling strength decays exponentially[19] with increase in the interparticle separation. Hence to directly observe the molecular dynamics (of proteins) it is desirable to have the participating gold sphere monomers in close proximity (Figure 6.2).[19, 20] This concept has been experimentally verified by investigating the salt dependent changes in persistent length of DNA tethered plasmon rulers,[18] wherein a compression of the tether produces a corresponding red shift and intensity rise in the dimer spectra and vice versa (Appendix D, Figure D6). Potentially, a conformationally active protein (like Hsp90) could bring about similar changes in interparticle separation distances. Thus, molecular dynamics in single proteins can be studied in real time by monitoring the spectral shifts (and intensity change) in the plasmon ruler system. To achieve this we measured the light scattering

spectrum of single gold dimers under illumination from a halogen lamp. The conformational dynamics of Hsp90 (nucleotide free thermal fluctuations) on single dimers was monitored at 28°C and 100ms temporal resolution by optical dark-field spectroscopy.
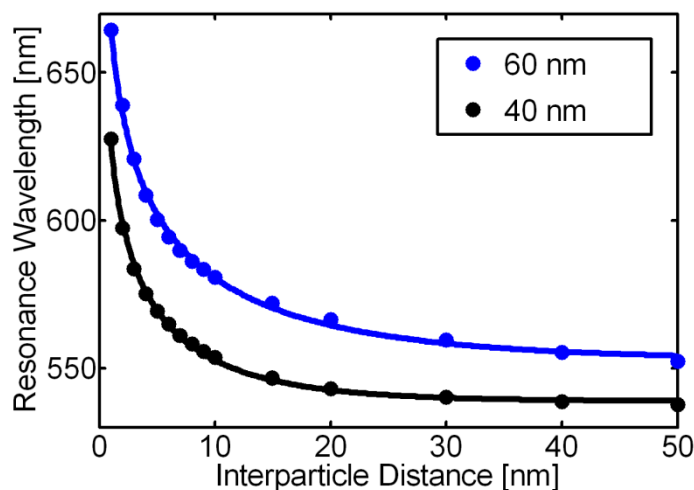
Figure 6.2. BEM simulation showing dependence of resonance position of gold dimers on interparticle gap distance.[20]

5.2.2 Key Aspects Of Plasmon Ruler System

In comparison with other techniques (FRET,[15] HX-MS[21]), the signal to noise ratio is significantly improved in our dark-field setups that allows the direct identification of single protein conformational dynamics for tens of minutes to several hours with 0.3nm precision.[17] Unlike flurophores, the plasmonic dimers do not suffer from effects such as photobleaching and photoblinking,[22] thus allowing long-term continuous measurements. The dimer preparation and sensor fabrication steps are simple, reproducible and cost-effective. All these features allow us to resolve single opening and closing states in Hsp90 (and other protein of interest), otherwise hidden in ensemble measurements. Such plasmonic dimers can be used to experimentally understand molecular movement, dynamics and function of many other biomolecules. The method could not only aid in understanding the dynamic behavior of individual molecules, but also in exploring heterogeneity among different molecules within a population and in determining mechanisms of their action.


5.3 Experimental Results

In this section, the main results on particle functionalisation, dimer synthesis and time resolved conformational dynamics of Hsp90 as detected by optical dark-field microscopy will

be presented. Several control measurements to illustrate the fidelity of our experiments are also included.

5.3.1 Proof Of Concept

We selected Hsp90 to demonstrate the functioning of plasmon ruler. Molecular chaperones Hsp90s are elongated dimers (with N- and C-terminal dimerization sites) that aid in folding of 5-10% of cellular proteins (called 'client' proteins). The members of this class include- human (Hsp90α) and yeast (yHsp90) isoforms, bacterial HtpG, mitochondrial Trap1 and endoplasmic reticulum Grp94.[23] Structural characterization of Hsp90s reveal the presence of an ATP binding cleft at N-terminal domain that bind and hydrolyze ATP, a hydrophobic cleft in middle domain for recruitment of client proteins and a C-terminal domain involved in dimerization and autophosphorylation.[24] Recently, FRET measurements has shown that cycling of Hsp90 between open (nucleotide free form) and closed (ATP bound state dimerised at N-terminii) states is a thermally driven phenomena weakly regulated by the nucleotides.[15] Whereas bacterial HtpG stays mainly in the closed compact state,[25] its yeast counterpart yHsp90 stays more in the open state and is less dependent on nucleotide[26] for regulation. Hsp90α has been identified as a protein required for cancer invasiveness, therefore a deeper understanding of its dyanamics could be useful in the generation of potential therapeutics to treat cancer.[27]
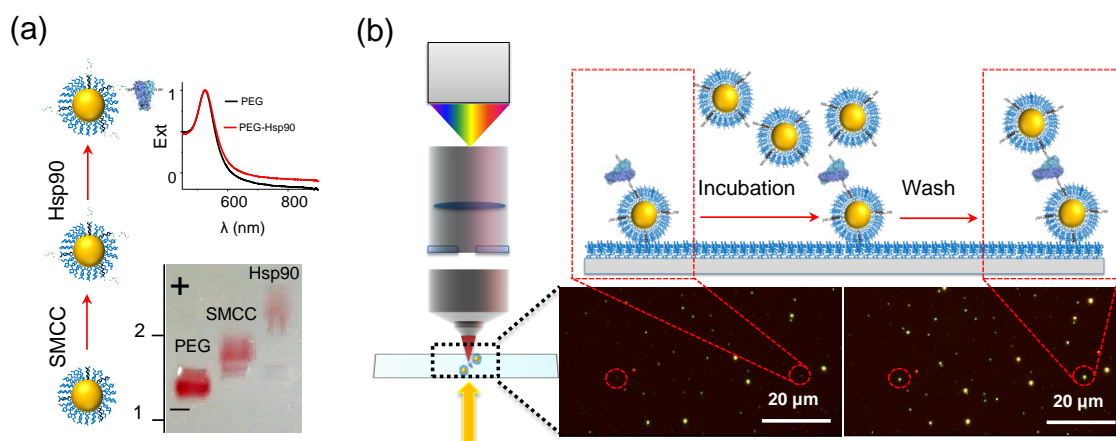

Figure 6.3. (a) The three step process for the synthesis of Hsp90 dimers: 40 nm gold spheres are functionalized with PEG mixture (1mM of NH2-PEG-SH: 30mM Meo-PEG-SH), the NH2 group reacts with NHS of SMCC molecule, the maleimide of SMCC reacts with a cysteine of Hsp90. The particles are characterized by UV-vis spectroscopy and gel electrophoresis on the basis of their surface coverage, size and charge. (b) Schematic showing the dimer formation steps on the PEG passivated glass flow cell channel: Hsp90 functionalized gold

spheres are immobilized into the passivation defects, immobilised particles are inubated with 10x concentrated maleimide-PEG functionalized particles to allow thiol-maleimide coupling, excess maleimide-PEG particles are removed by buffer wash. The as-synthesised dimers are characterized by their higher intensity and spectral shifts (not shown).

To investigate the N-terminal molecular dynamics of yHsp90 (molecular weight: 90 kDa) by plasmon ruler concept, its C-terminal domains were kept dimerized with the DmKHC coiled coil motif.[15] Gold nanospheres (40 nm) were functionalised with a mixed monolayer of PEG (3 kDa NH_2-PEG-SH and 2 kDa Meo-PEG-SH) and their protein-repellent behaviour were ascertained (Figure 6.3). Terminal amines of PEG were modified with SMCC (a bifunctional crosslinker) to enable the specific binding of yHsp90. In our experiments, yHsp90 tagged 40 nm gold spheres (SH-HspAu) were dimerized with maleimide-PEG functionalised 40 nm gold spheres (Mal-Au) on a passivated glass surface (passivated with APTES-PEG or crosslinked BSA, see Figure 6.3). The dimerisation efficiency was reduced to 3% by optimising the two PEG ratios on SH-HspAu particles to make multiple tether/nanoparticle attachments less probable (Appendix D, Figure D8).

5.3.2 Temporally Resolved Polymer Dynamics

Dimers formed via different linkers (like Hsp90, DNA and PEG linkers) were monitored at ~28°C with 100 ms time resolution under static-flow conditions for 30 min duration. The time resolved spectra were fitting with a Lorentzian, wherein the fit was only applied onto the top 20% region from the peak position of the spectra. Dimers linked via conformationally inactive moleules (DNA and PEG) do not show any appreciable changes (spectral shift ≤ noise level of the dark field setup) in their resonance position and scattering intensity (Appendix D, Figure D7 and Figure D13). However, dimers with Hsp90 shows pronounced discrete changes in λ_{res} ($\Delta\lambda_{res}$ ~2-3 nm) and intensity profiles (Figure 6.4 and Appendix D Figure D11- D12). Such effects in Hsp90 dimers could only be explained by conformational changes known to exist at around 30°C in Hsp90 (even under nucleotide-free conditions).[15] These spectral shifts in Hsp90 dimers successfully demonstrate for the first time, the utility of plasmon ruler for investigation of single protein dynamics. Figure 6.4 also indicates that the protein prefers to spend more time in its open states than in its closed states. The duration for which the protein stays in a particular state can also vary.
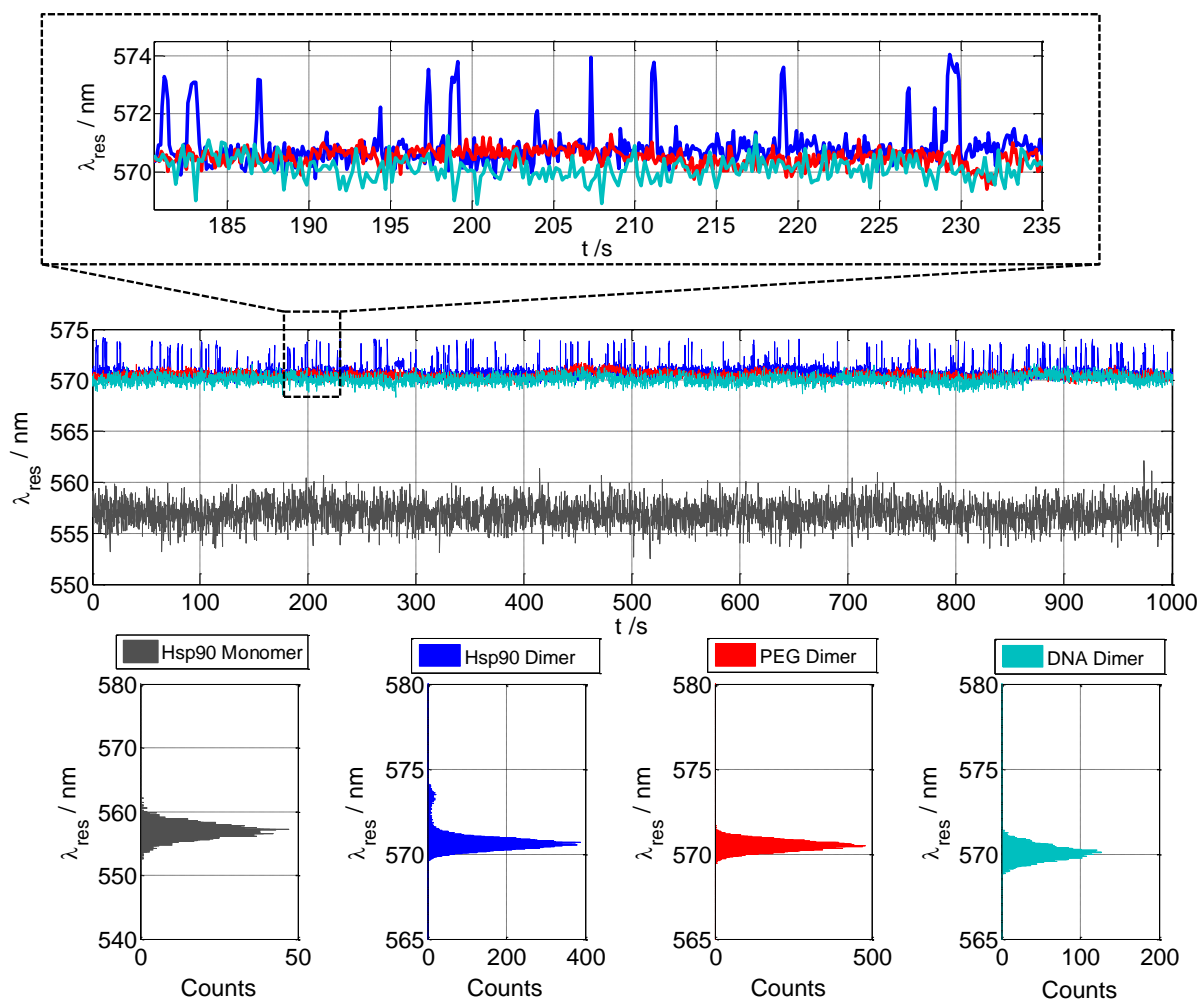
Figure 6.4. Hsp90 dimers demonstrating the distance dependent plasmon coupling as a result of thermally driven conformational dynamics of the protein. Open and closed states of Hsp90 results in spectral shift in the resonance position of Hsp90 dimer. The Hsp90 functionalized gold nanospheres and dimers tethered by other linker molecules (PEG, DNA), in contrast, show no significant linker dynamics over time.

## 5.3.3 Free Energy (K_BT) Landscapes Of Studied Polymers

The possible conformational states for the Hsp90, PEG and DNA dimers can be mapped by their free energy landscapes (Figure 6.5). The free energies are obtained by translating the spectral shifts into gap distance changes for all three kinds of dimers using the relation, $D = -15.2 \cdot \log (1 - 8.564e40 / \lambda_{res}^{14.925})$.[20] The gap distances shows two major states in the Hsp90 case, as indicated by the presence of two potential minima. Since the protein is linked via the PEG molecule, the linker contribution ($\sigma = 0.2$) was subtracted to get the Hsp90 potential (shown in blue). The free energy barrier of 4 K_BT is inarguably weaker (than a covalent bond of ~80 K_BT)[28] to allow thermally driven state transitions in Hsp90.
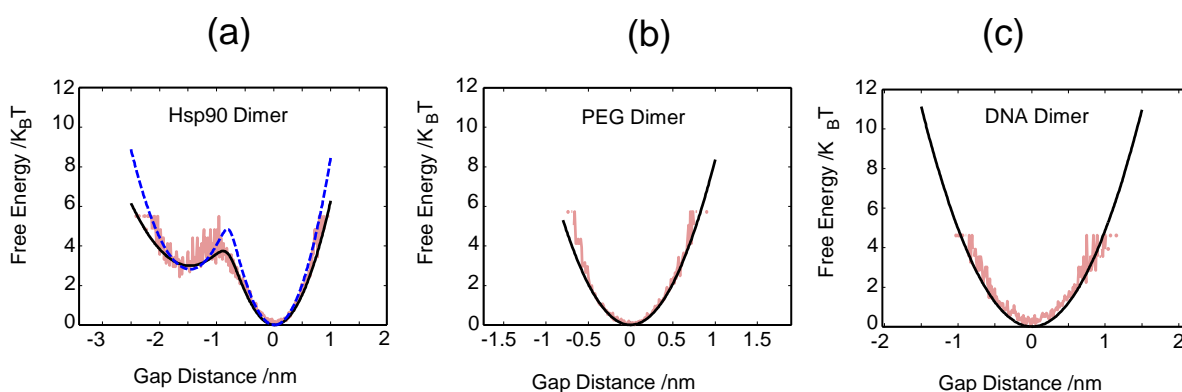
Figure 6.5. Energy landscape of the (a) Hsp90 nucleotide-free conformational states (b) PEG linked dimer (c) DNA linked dimer. The energy landscape shows two minima for Hsp90 (demonstrating two states) as opposed to one minima for PEG and DNA tethers.

5.3.4 Deciphering The Time Constants Of States (τ)

To understand the protein dynamics further, a more detailed investigation on the open and closed states were performed. The two prominent states were distinguished by setting a threshold right above the setup noise level. The dwell times for the protein in both states were calculated and all such counts were integrated to give the cumulative dwell time distribution. The resulting data was fitted with the function c_0+s $(1- e^{-t/\tau})$: where c_0 is the initial count, s is the scaling factor, t is the time and τ is the time constant. The time constant (τ) of the two states from five different measurements were extracted. Figure 6.6 shows that the dwell times for all measured dimers are at least 10 fold higher in open states. The time constants of closed states for these dimers do not deviate much, but it's highly variable for the open states (Figure 6.6). This variability could arise from the heterogeneity among the proteins within the same population.
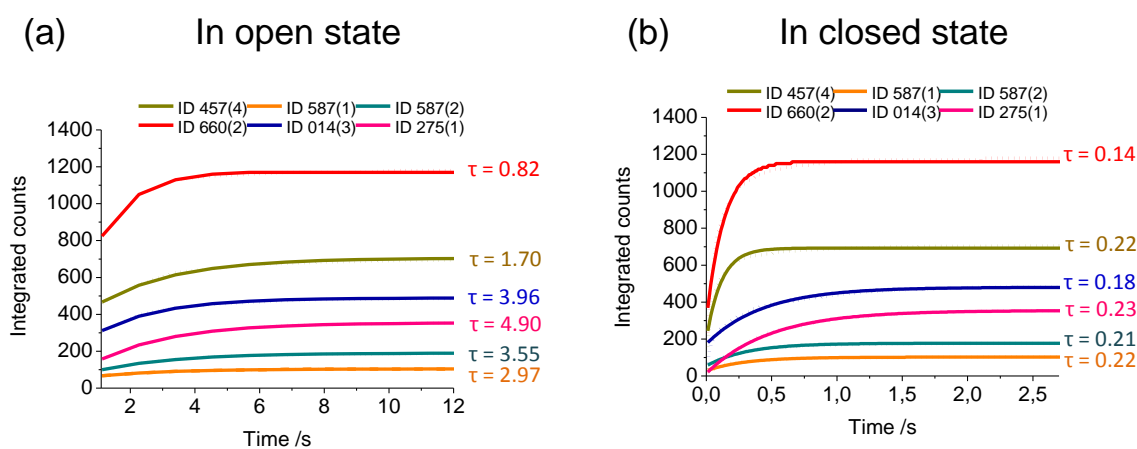
Figure 6.6. Dwell-time distributions for Hsp90 dimers measured at ~28°C in nucleotide-free environment. Integrated dwell-time distribution and time constant, τ, in the (a) open and (b) closed states for five such dimers.

76

5.4 Discussion

In this section, I will discuss about the possible ways scale-up in dimer synthesis and faster detection of molecular dynamics by single particle spectroscopy along with potential applications of this method.

5.4.1 Perspective for further improvements

Our method can track the large scale conformational changes in proteins in milliseconds to few seconds regime for a sufficiently long time. However, to explore faster dynamics in proteins and to better resolve the opening and closing state transitions,[29] a setup with much higher spatial and temporal resolution in microseconds time regime will be required.[16] Additionally, further improvements in the dimerisation efficiency and more robust surface passivation strategies is needed to minimise the formation of false dimers and higher order aggregates. This could be achieved by approaches that lead to either screening and purification of dimer forming particles or forming dimers in batch[30] to minimise the time consuming steps in the current strategy. Besides, batch synthesis of Hsp90 harbouring dimers should offer higher statistics on the measured data and help in understanding the heterogeneity within the protein population.

5.4.2 Plasmon ruler as a potential tool for future

Detection of single molecule dynamics with individual plasmonic dimers is a new step towards understanding the behaviour of molecules involved in cellular processes. With our new scheme, we can monitor open and closed states of conformationally active proteins in real time on a single molecule basis that otherwise average out in large ensembles of molecules. Plasmon rulers can also be utilized to study fundamental phenomena on the molecular level such as cascade reactions in cellular processes, molecular heterogeneity among proteins and protein behaviour under various environmental perturbations.

References

1.   Micheletti, C. *Physics of Life Reviews* **2013,** 10, (1), 1-26.
2.   Roy, R.; Hohng, S.; Ha, T. *Nat Meth* **2008,** 5, (6), 507-516.
3.   Grier, D. G. *Nature* **2003,** 424, (6950), 810-816.
4.   Kaltashov, I. A.; Eyles, S. J. *Mass Spectrometry Reviews* **2002,** 21, (1), 37-71.

5. Borbat, P. P.; Costa-Filho, A. J.; Earle, K. A.; Moscicki, J. K.; Freed, J. H. *Science* **2001,** 291, (5502), 266-269.

6. Fu, L.; Liu, J.; Yan, E. C. Y. *Journal of the American Chemical Society* **2011,** 133, (21), 8094-8097.

7. Ratzke, C.; Hellenkamp, B.; Hugel, T. *Nat Commun* **2014,** 5.

8. Hall, W. P.; Modica, J.; Anker, J.; Lin, Y.; Mrksich, M.; Van Duyne, R. P. *Nano Letters* **2011,** 11, (3), 1098-1105.

9. Reinhard, B. M.; Sheikholeslami, S.; Mastroianni, A.; Alivisatos, A. P.; Liphardt, J. *Proceedings of the National Academy of Sciences* **2007,** 104, (8), 2667-2672.

10. Wiener, D. M.; Lionberger, T. A. *Analytical Chemistry* **2013,** 85, (10), 5095-5102.

11. Jun, Y.-w.; Sheikholeslami, S.; Hostetter, D. R.; Tajon, C.; Craik, C. S.; Alivisatos, A. P. *Proceedings of the National Academy of Sciences* **2009,** 106, (42), 17735-17740.

12. Zhao, R.; Leung, E.; Grüner, S.; Schapira, M.; Houry, W. A. *PLoS ONE* **2010,** 5, (4), e9934.

13. Liu, G. L.; Yin, Y.; Kunchakarra, S.; Mukherjee, B.; Gerion, D.; Jett, S. D.; Bear, D. G.; Gray, J. W.; Alivisatos, A. P.; Lee, L. P.; Chen, F. F. *Nat Nano* **2006,** 1, (1), 47-52.

14. Ravi, S.; Krishnamurthy, V. R.; Caves, J. M.; Haller, C. A.; Chaikof, E. L. *Acta Biomaterialia* **2012,** 8, (2), 627-635.

15. Mickler, M.; Hessling, M.; Ratzke, C.; Buchner, J.; Hugel, T. *Nat Struct Mol Biol* **2009,** 16, (3), 281-286.

16. Ament, I.; Prasad, J.; Henkel, A.; Schmachtel, S.; Sönnichsen, C. *Nano Letters* **2012,** 12, (2), 1092-1095.

17. Rosman, C.; Prasad, J.; Neiser, A.; Henkel, A.; Edgar, J.; Sönnichsen, C. *Nano Letters* **2013,** 13, (7), 3243-3247.

18. Sonnichsen, C.; Reinhard, B. M.; Liphardt, J.; Alivisatos, A. P. *Nat Biotech* **2005,** 23, (6), 741-745.

19. Jain, P. K.; Huang, W.; El-Sayed, M. A. *Nano Letters* **2007,** 7, (7), 2080-2088.

20. Becker, J. *Springer Theses* **2012**.

21. Graf, C.; Stankiewicz, M.; Kramer, G.; Mayer, M. P. *The EMBO Journal* **2009,** 28, (5), 602-613.

22. Burnette, D. T.; Sengupta, P.; Dai, Y.; Lippincott-Schwartz, J.; Kachar, B. *Proceedings of the National Academy of Sciences* **2011,** 108, (52), 21081-21086.

23. Chiosis, G.; Dickey, C. A.; Johnson, J. L. *Nat Struct Mol Biol* **2013,** 20, (1), 1-4.

24. So˝ti, C.; Vermes, Á.; Haystead, T. A. J.; Csermely, P. *European Journal of Biochemistry* **2003,** 270, (11), 2421-2428.

25. Ratzke, C.; Berkemeier, F.; Hugel, T. *Proceedings of the National Academy of Sciences* **2012,** 109, (1), 161-166.

26. Ratzke, C.; Nguyen, M. N. T.; Mayer, M. P.; Hugel, T. *Journal of Molecular Biology* **2012,** 423, (3), 462-471.

27. Trepel, J.; Mollapour, M.; Giaccone, G.; Neckers, L. *Nat Rev Cancer* **2010,** 10, (8), 537-549.

28. Peter, C.; Kremer, K. *Faraday Discussions* **2010,** 144, (0), 9-24.

29. Chung, H. S.; Eaton, W. A. *Nature* **2013,** 502, (7473), 685-688.

30. Lim, D.-K.; Jeon, K.-S.; Kim, H. M.; Nam, J.-M.; Suh, Y. D. *Nat Mater* **2010,** 9, (1), 60-67.

SUMMARY

Through the chapters of my thesis, I have placed emphasis on the potential of plasmonic gold nanoparticles as sensors for a range of biomedical applications. I have also conveyed the importance of a robust surface functionalization of these gold nanoparticles and fast optical setups to realise their sensing application. To conclude, a brief summary of major accomplishments and milestones achieved during the PhD period is presented herewith.

Chapter 2 describes how the surface of unfunctionalized CTAB capped gold nanorods can perform the detection of proteins with the ultimate detection limit of single molecule. Commonly, fluorescent dye labels or enzymatic amplification are employed for single molecule sensing which modifies the species under investigation and therefore influences biological processes. In this chapter , a novel technique was presented for detection of single unlabeled fibronectin proteins with extremely high temporal resolution in milliseconds regime. Fibronectin molecules could also be desorbed from the nanorod surface with the help of anionic surfactants. This technique could potentially resolve equilibrium coverage fluctuations, opening a window into Brownian dynamics of unlabeled macromolecules.

Surfactant-capped gold nanorods attract proteins non-specifically. To perform an efficient and cost-effective multiplexed detection for proteins in small liquid samples, the gold nanorods were functionalised with DNA aptamers. In chapter 3, I have presented a novel multiplexed sensor with randomly deposited aptamer functionalized gold nanorods. The spectral position of plasmon resonances of individual nanorods, monitored by dark-field spectroscopy, respond specifically to different proteins. Using four different aptamers, I have demonstrated nanomolar sensitivity, sensor recycling and the potential to upscale to hundreds or thousands of targets. The applications for inexpensive multiplexed sensors are abundant like identifying human, animal and plant diseases, monitoring food composition, quality and safety, screening for explosives, drugs or environmental hazards.

Multiplexed gold nanorod sensors are not only limited to the detection of aptamer specific targets, but they also be tailor made to perform simultaneous detection of protein-protein interactions. Most of current techniques used for the quantification of protein-protein interactions require the analysis of one pair of binding partners at a time. In chapter 4, I have presented a label-free, simple, fast and cost-effective route to characterize binding affinities between multiple macromolecular partners simultaneously, using optical dark-field

spectroscopy and individual protein-functionalized gold nanorods as sensing elements. A stable stock of NTA DNA-functionalized gold nanorods was used to create a library of His-tagged protein-functionalized nanorods by simply adding proteins to small aliquots of the nanorod stock solution. As a proof of concept, the binding affinities of three interacting pairs (FtsZ-s1ZipA, FtsZ-s2ZipA and FtsZ-MinC) were successfully determined.

Multiplexed analyte detection schemes can largely benefit from highly sensitive and spectrally tunable plasmonic nanostructure. However, there is a lack of such nanostructures for the mid-visible spectral regions as most available nanostructures offer high sensitivity in red to far red spectrum. In chapter 5, I have reported a simple strategy to produce highly sensitive gold nanostructures that work in the mid-visible electromagnetic region. These structures were produced by the assembly of 20nm gold nanoparticle satellites onto 60 nm spherical gold cores under the influence of hydroxylamine. Due to plasmon coupling between interacting nanoparticles, the core-satellite structures show a two-fold higher sensitivity than similar sized gold nanospheres.

Plasmon coupling also forms the basis for distance dependent sensing by plasmon rulers or dimers. Plasmonic dimers respond to changes in interparticle separation by expressing a spectral shift in their resonance maxima and large changes in scattering intensity. In chapter 6, I have presented a system consisting of a single protein sandwiched between two functionalised gold nanospheres to exploit this distance dependent spectral shifts in monitoring conformatioanl dynamics of the protein. The plasmonic gold nanoparticle dimers have been used for long term investigation of nucleotide-free N-terminal conformational dynamics in heat shock protein Hsp90 with millisecond temporal resolution. This work demonstrates the first proof of concept for detection of protein conformational dynamics by plasmon rulers.

APPENDIX

APPENDIX A

A. Multiplexed Analyte Sensing by Aptamer Functionalised Gold Nanorods

A.1 Materials and Methods

A.1.1 Materials

Reagents, metallic salts, buffers, tris(2-carboxyethyl)phosphine (TCEP) , sodium dodecylsulphate (SDS), cetyltrimethylammonium bromide (CTAB) and other analytical grade chemicals were acquired from Sigma-Aldrich, Fluka or Merck. Aptamer DNA oligonucleoides were purchased from Biomers.net GmbH (Germany). Polyethylene glycols (mPEG-SH M_W 3000 Da, mPEG-SH M_W 5000 Da) were ordered from Iris Biotech. The proteins (Bovine Serum Albumin, Fibronectin, Streptavidin, Immunoglobulin E, Thrombin and Trypsin and others) were purchased from Sigma or Merck. Deionized water from a Millipore system (> 18 MΩ, Milli Q) was used in all experiments.

A.1.2 Methods

A.1.2.1 Synthesis of CTAB capped gold nanorods.

Gold nanorods of aspect ratio 2.2 (67.8 x 31.1) were synthesized by slight modification in the reported procedure.[1,2] Briefly, seeds were prepared by adding an ice cold solution of 0.01 M sodium borohydride rapidly and under vigorous stirring to a solution of 0.1 mM $HAuCl_4$ (tetrachloroauric acid) and 25 mM CTAB (hexadecyltrimethyl ammonium bromide). A 1 mL of this seed solution was inoculated into a 1 L growth solution (0.1 M CTAB, 0.5 mM $HAuCl_4$, 0.6 mM ascorbic acid and 70 µM $AgNO_3$) and stirred for one hour at 30°C. The nanorods were centrifuged three times at 2,790 g for 20 min and resuspended in 0.05M CTAB solution after completion of each round.

A.1.2.2 Synthesis of Aptamer functionalised gold nanorods

A 50 µL suspension of 0.14 nM CTAB stabilized AuNRs was centrifuged at 6,290g for 5 min. The pellet of gold nanorods was recovered from the bottom after discarding the supernatant. In the meantime, 50µl of reaction mixture (consisting of 50µM DNA aptamer,

0.4% SDS and 5mM TCEP) was prepared in binding buffer (20 mM Tris acetate, 140 mM sodium chloride, 5 mM potassium chloride, 2.5 mM magnesium chloride, 1 mM calcium chloride, pH 7.4) and stored at room temperature for 30 min to allow reduction of disulfide bonds in aptamers. The mixture was then heated at 95°C for 10 min and subsequently incubated room temperature for 30 minutes. The DNA aptamers showing specificity against either of the four targets- Fibronectin,[3] Streptavidin,[4] Immunoglobulin E (IgE)[5] or Thrombin[6] were used. The pellet of gold nanorods was resuspended in this reaction mixture and incubated at room temperature overnight. The stock of aptamer functionalized gold nanorods was aliquoted and diluted to 1:800 in binding buffer to just before performing the experiments.

A.1.2.3 Sensor fabrication and target detection

The microfluidic flow cell was constructed by two coverslips (the former one patterened to have three small holes on either ends while the latter was unpatterned) sandwiched together with a piece of Nescofilm (exhibiting channel patterns). The flow cell was mounted in a holder and thin tubings (acting as inlets and oulets) were connected to the holes in the patterned coverslip. The assembled flow cell was lodged onto the dark-field microscope stage. The channels in the flow cell were cleaned with a short rinse of 100 µL solution of 50% Hellmanex II in water. Aptamer functionalized AuNRs were immobilised in the flow cell channel by flowing in one nanoparticle batch at a time. Position enoding of each aptamer-gold nanorod batch is done by the software to group their responses accordingly. For the target detection, the binding buffer was supplemented with 450 µg/mL (6.82µM) bovine serum albumin to provide an 'unspecific' protein background. Spectra of all immobilised particles are recorded in BSA binding buffer to designate the reference position. Then, a solution containing one or several target proteins was added (typical target molecule concentration was 20 µg/mL) in BSA binding buffer for 30 min. After washing with BSA binding buffer for 15 min, the plasmon resonance wavelengths were recorded again to calculate the shifts $\Delta\lambda$.

A.1.2.4 Regeneration of sensor surface

Sensor regeneration was achieved by rinsing the flow cell with 20µM trypsin protease in regeneration buffer (20 mM Tris acetate, 140 mM sodium chloride, 5 mM potassium chloride, pH 8.0) for 25 minutes. Trypsin chops the bound targets into fine fragments that no longer retain shape complementarity with the aptamer and hence gets washed away with 10 min buffer rinse.

A.2 Experiments and Controls

A.2.1 Electrophoretic characterization of functionalized nanorods

Different sets of controls were done in order to test the successful functioanlisation of gold nanorods with DNA aptamers. The electrophoretic mobility of aptamer functionalized nanorods were performed alongside other controls in a 0.5% Agarose gel.[7] Figure A1 shows the resulting unstained gel for the differently functionalized nanoparticles. Lane 6-9 contains functionalized particles prepared by the method above, lane 1-5 various controls. None of the controls (incubated in buffer) except for methoxy-PEG functionalized gold nanorods migrated in the gel, while SDS stabilized nanorods only show migration when incubated in water (buffer addition leads to their aggregation). The migration of thiolated m-PEG-AuNR conjugates to the negative end proves that SDS did not compete or interfere during the PEG-binding process.
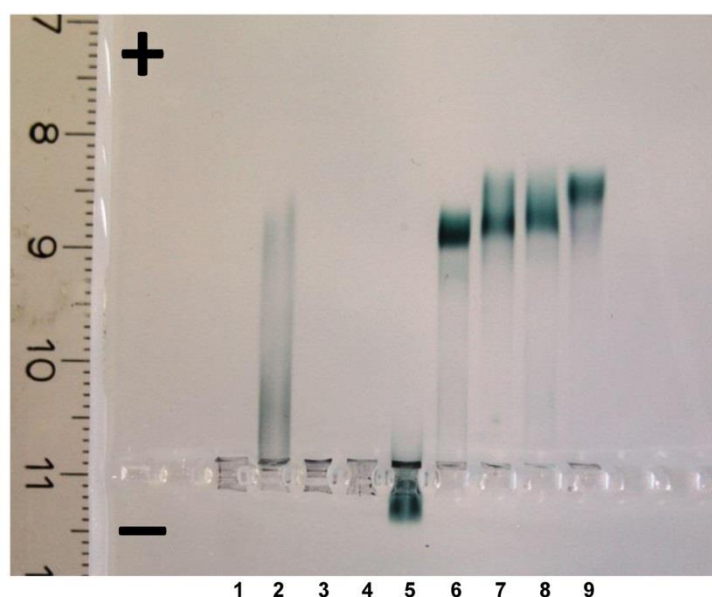
Figure A1. Electrophoretic mobility of gold nanorods in 0.3% agarose gel (150V, 25 min). The SAM layer on gold nanorods tested here are as folows

Lane 1: Cetyltrimethylammonium bromide-AuNR

Lane 2: Sodium dodecylsulphate- AuNR (in water)

Lane 3: Sodium dodecylsulphate- AuNR (in buffer)

Lane 4: 50μM non-thiol DNA-AuNR (in SDS + buffer)

Lane 5: 50μM thiol-methoxy-PEG-AuNR (in SDS + buffer)

Lane 6: 50μM thiol-antifibronectin aptamer-AuNR (in SDS + buffer)

Lane 7: 50μM thiol-antistreptavidin aptamer-AuNR (in SDS + buffer)

Lane 8: 50μM thiol-antiimmunoglobulin E aptamer-AuNR (in SDS + buffer)

Lane 9: 50μM thiol-antithrombin aptamer-AuNR (in SDS + buffer).

A.2.2 Verification of target specificity of aptamers

As many as 11 different aptamer sequences were obtained from the literature for this work. The aptamers were tested with conventional SPR measurements (Reichert SPR instrument) for their target specificity. Measurements were done in a dual channel microfluidic system. One of the channels (the sample channel) was functionalized with active aptamer in binding buffer, whereas the other channel (reference channel) was passivated with the thiolated mPEG (M_W 5000 Da) to prevent unspecific protein binding to the gold surface. The procedure was performed in binding buffer throughout.

The microfluidic channels were successively injected with BSA, non-target proteins and the target protein, each for about 20 minutes. Only those aptamers which showed minimum to no affinity for non-targets were selected for further experiments . Table A1 depicts the results with aptamers used in the study.

Table A1: Cross-talk studies on 11 different aptamers

Target	Sequence of DNA Aptamer	Cross reactivity
Thrombin	5'-SH-(T_{10})-GGTTGGTGTGGTTGG-3' [8] 5'-SH-(T_{10})-AGTCCGTGGTAGGGCAGGTTGGGGTGACT-3' [6]	Lysozyme
Fibronectin	5'-SH-(T_{10})-CATGCGCCTTCCCCCTGTGGTTGGTGTCAGTCGGCCTGTG-3' [3]	Lysozyme
IgE	5'-SH-(T_{10})-GGGGCACGTTTATCCGTCCCTCCTAGTGGCGTGCCCC-3' [5]	HNE and Lysozyme
Streptavidin	5'-SH-(T_{10})-ATTGACCGCTGTGTGACGCAACACTCAAT-3' [4]	HNE and Lysozyme
HNE	5'-SH-(T_{10})-CACGGTAGTGCTACCAGATGGTTATGTTAC-3' [9]	Lysozyme
Lysozyme	5'-SH-(T_{10})-ATCTACGAATTCATCAGGGCTAAAGAGTGCAGAGTTACTTAG-3' [10]	-
Insulin	5'SH-(T_{10})-GGTGGTGGGGGGGGGTTGGTAGGGTGTCTTC-3' [11]	Target binding Failed
PDGF	5'-SH-(T_{10})-CAGGCTACGGCACGTAGAGCATCACCATGATCCTG-3' [12]	Bovine Serum Albumin Target binding Failed
VEGF	5'-SH-(T_{10})-TGTGGGGGTGGACGGGCCGGGTAGA-3' [13]	Bovine Serum Albumin Target binding Failed
L-Selectin	5'-SH-(T_{10})-CAAGGTAACCAGTACAAGGTGCTAAACGTAATGGCTTCG-3' [14]	Bovine Serum Albumin Target binding Failed
Nucleolin	5′-SH-(T_{10})-GGTGGTGGTGGTTGTGGTGGTGGTGG-3' [15]	Bovine Serum Albumin Target binding Failed

The SPR sensograms of only 6 out of 11 aptamer sequences showed significant response towards their targets. However, we observed undesirable cross-talk of some of these target responsive aptamers with lysozyme and human neutrophil elastase. Lysozyme was found to bind transiently to the most other aptamers at a concentration of 2.85 μM. A plausible explanation could be the positive charge of Lysozyme under the specified set of conditions that allows the protein to electrostatic interacts with DNA. Apparently, these non-specific interactions were weak in nature as they could be removed by prolong rinse with binding buffer (Figure A2). As the binding of Lysozyme and HNE were non-specific in nature, therefore these proteins were excluded from our study. We believe that their meticulous detection demands either an appropriate modification in existing aptamers or replacing aptamers with more reliable Photoaptamers[16] and SOMAmers[17].
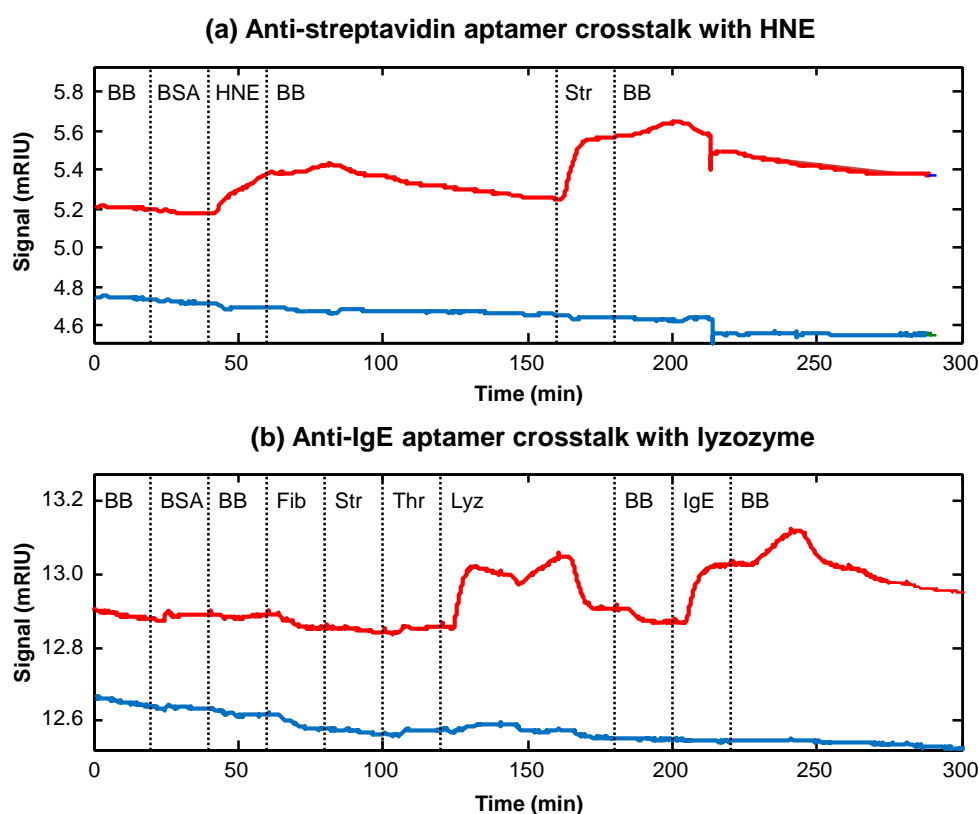
Figure A2. SPR response showing **a**, HNE cross talk in anti-streptavidin aptamer, **b**, Lysozyme cross talk in anti-IgE aptamer. Green - reference, blue - sample. BB: binding buffer, BSA: Bovine Serum Albumin, Fib: Fibronectin, Str: Streptavidin, Thr: Thrombin, Lyz: Lysozyme, HNE: human neutrophil elastase.

A.2.3 Demonstration of a parallel sensing approach
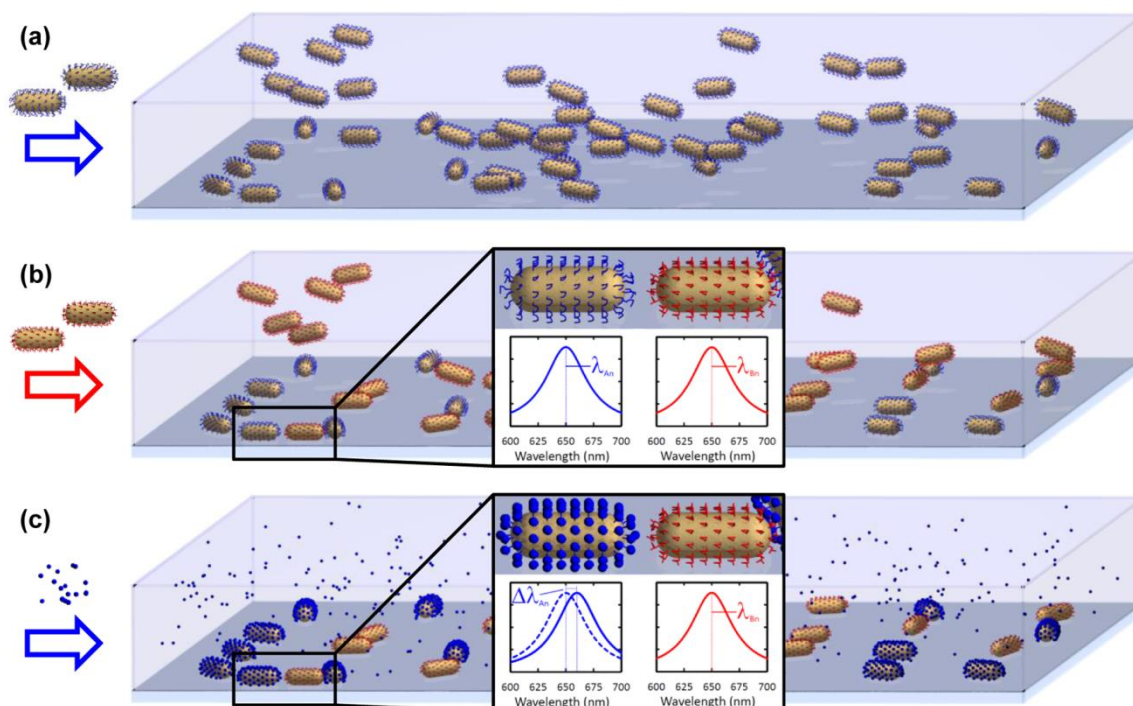
Figure A3. Sensor fabrication strategy and detection method. a,**b** To fabricate a position encoded sensor, aptamer coated nanoparticles are deposited sequentially (recording their positions after each step) in a microfluidic flow cell.. **c**, To detect an analyte in a solution, it is injected into the flow cell (in both cases), the targets bind specifically to their corresponding aptamer coated nanoparticles and induce shifts $\Delta\lambda_{res}$ in their plasmon resonances.

For many existing multiplexed sensors, the sensor fabrication strategy requires to deposit prefabricated nanoparticles by micro-spotting, a slow serial process resulting in expensive sensors with integration densities far below the theoretical limit. Our approach is to simply deposit nanoparticles functionalised with receptors for specific targets T_i randomly from solution disregarding the order and control of spotted arrays. By flowing in one nanoparticle batch at a time while recording the position of each deposited nanoparticle, we know the specific target for each particle. This serial process results in a 'mapped sensor' with a position encoding similar to a spotted array but without the geometric order (Figure A3).

To demonstrate the proof of concept of our sensing strategy, we chose aptamers against Fibronectin, Streptavidin, IgE and Thrombin, as these were not found to cross talk with each other. The microfluidic flow cell was fabricated as illustrated in Figure A3 to form four groups of aptamer functionalised particles, each group responsive towards its own target. No significant shift was observed in the absence of targets after a repeat measurement on the

same particles were performed. Injection of a target lead to a spectral shift in the resonance position of the corresponding group of aptamer functionalised nanorods (Figure A4).
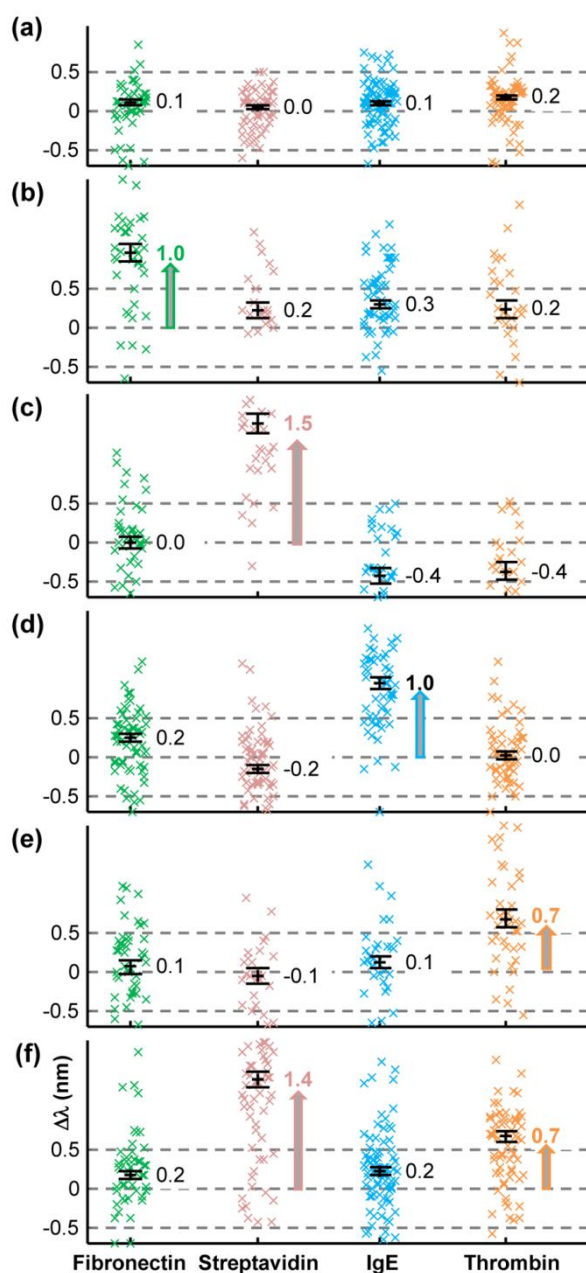
Figure A4. Target detection in a multiplexed sensor. (a-f) show the plasmon shifts of 147-272 particles in a multiplexed sensor after exposure to **a**, no analyte (control), **b**, Fibronectin (Fib), **c**, Streptavidin (Str), **d**, IgE, **e**, Thrombin (Thr), **f**, Streptavidin and Thrombin. Each cross represents the response of an individual nanoparticle. The four columns on the left show the response of particles grouped according to their functionalisation (23-90 particles per group) with the median and its error (s.e.m.) indicated by black symbols and numbers. Median responses above the detection limit $L = 0.5$, indicated with arrows, correctly identify the analytes in all cases.

The remaining groups do not show a change in resonance position above the threshold level (L=0.5nm, set by analysing results from 15 different experiments as shown in Figure A5). The magnitude of spectral shifts was different for each aptamer-target group. This could be

due to the combined effect of size difference among the four aptamer groups used and different packing density (or refractive index) of four targets used in our study. The shift size remains unaffected in a more complex media containing multiple different targets (Figure A4f).
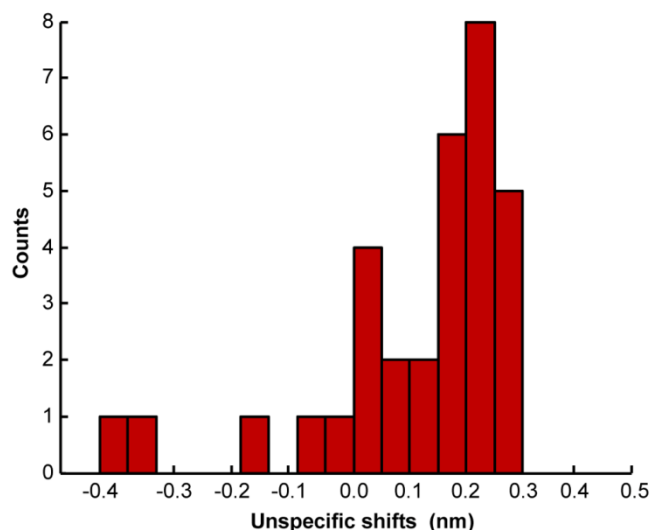
Figure A5. Histogram for 15 experiments showing non-specific sensor response.

References

(1)   Jana, N. R.; Gearheart, L.; Murphy, C. J. *J. Phys. Chem. B* **2001,** *105*, 4065-4067.

(2)   Nikoobakht, B.; El-Sayed, M. A. *Chem. Mater.* **2003,** *15*, 1957-1962.

(3)   Ogawa, A.; Tomita, N.; Kikuchi, N.; Sando, S.; Aoyama, Y. *Bioorgan. Med. Chem. Lett.* **2004,** *14*, 4001-4004.

(4)   Bing, T.; Liu, X.; Cheng, X.; Cao, Z.; Shangguan, D. *Biosens. Bioelectron.* **2010,** *25*, 1487-1492.

(5)   Wang, Z.; Wilkop, T.; Xu, D.; Dong, Y.; Ma, G.; Cheng, Q. *Anal. Bioanal. Chem.* **2007,** *389* (3), 819-825.

(6)   Tasset, D. M.; Kubik, M. F.; Steiner, W. *J. Mol. Biol.* **1997,** *272*, 688-698.

 (7)   Hanauer, M.; Pierrat, S.; Zins, I.; Lotz, A.; Sönnichsen, C. *Nano Lett.* **2007,** *7*, 2881-2885.

(8)   Bock, L. C.; Griffin, L. C.; Latham, J. A.; Vermaas, E. H.; Toole, J. J. *Nature* **1992,** *355* (6360), 564-566.

(9)   Charlton, J.; Sennello, J.; Smith, D. *Chem. Biol.* **1997,** *4*, 809-816.

(10)   Cheng, A. K. H.; Ge, B.; Yu, H.-Z. *Anal. Chem.* **2007,** *79*, 5158-5164.

(11)   Cha, T.-G.; Baker, B. A.; Sauffer, M. D.; Salgado, J.; Jaroch, D.; Rickus, J. L.; Porterfield, D. M.; Choi, J. H. *ACS Nano* **2011,** *5*, 4236-4244.

(12)   Fang, X.; Sen, A.; Vicens, M.; Tan, W. *Chem. Bio. Chem.* **2003,** *4*, 829-834.

(13)   Nonaka, Y.; Sode, K.; Ikebukuro, K. *Molecules* **2010,** *15*, 215-225.

(14)   Hicke, B. J.; Watson, S. R.; Koenig, A.; Lynott, C. K.; Bargatze, R. F.; Chang, Y. F.; Ringquist, S.; Moon-McDermott, L.; Jennings, S.; Fitzwater, T.; Han, H. L.; Varki, N.; Albinana, I.; Willis, M. C.; Varki, A.; Parma, D. *J. Clin. Invest.* **1996,** *98*, 2688-2692.

(15)   Soundararajan, S.; Chen, W.; Spicer, E. K.; Courtenay-Luck, N.; Fernandes, D. J. *Cancer Res.* **2008,** *68*, 2358-2365.

(16)   Bock, C.; Coleman, M.; Collins, B.; Davis, J.; Foulds, G.; Gold, L.; Greef, C.; Heil, J.; Heilig, J. S.; Hicke, B.; Nelson Hurst, M.; Husar, G. M.; Miller, D.; Ostroff, R.; Petach, H.; Schneider, D.; Vant-Hull, B.; Waugh, S.; Weiss, A.; Wilcox, S. K.; Zichi, D. *Proteomics* **2004,** *4*, 609-618.

(17)   Gold, L.; Ayers, D.; Bertino, J.; Bock, C.; Bock, A.; Brody, E. N.; Carter, J.; Dalby, A. B.; Eaton, B. E.; Fitzwater et al. *PLoS ONE* **2010,** *5*, e15004.

B. Simultaneous Detection of Protein-protein Interaction by Ni^{2+}-NTA Functionalised Gold Nanorods

B.1 Materials and Methods

B.1.1 Materials

Reagents, metallic salts, buffers, guanosine 5´-diphosphate (GDP) and other analytical grade chemicals were acquired from Sigma-Aldrich or Merck. Deionized water from a Millipore system (> 18 MΩ, Milli Q) was used in all experiments. Isothiocyanobenzyl-NTA was purchased from Dojindo EU GmbH. T-linker-DNA (5'-SH-TTTTTTTTTTT-3') and Thiolated-DNA (5'-SH-TTTTTTTTTTT-NH$_2$-3') were purchased from Biomers.net GmbH. The proteins were equilibrated against the working buffer (50 mM Tris-HCl pH 7.5, 100 mM KCl, 5 mM MgCl$_2$). For FtsZ we additionally incorporate to the buffer 0.05 mM of GDP.

B.1.2 Methods

B.1.2.1 Protein purification

Escherichia coli wild-type FtsZ was expressed and purified by the calcium-induced precipitation method.[1] Mutagenesis of the ZipA gene, overexpression, and purification were carried out by removing the part ranging of the N-terminal domain of wild type ZipA (amino acids 1-25 for s1ZipA, and amino acids 1-188 in the case of s2ZipA).[2,3] For MinC, the plasmid pWM2688, encoding His-tagged MinC, was generated by amplifying the *minC* gene with primers 890 (GCGAGCTCTCAAACACGCCAATCGAGC) and 803 (CGGGATCCTCAATTTAACGGTTGAACGG) and cloning it as a *Sac*I-*Bam*HI restriction digested fragment into the equally restriction digested plasmid pWM2619 to render pWM2622 and then into *Nco*I-*Bam*HI-cleaved pET28a.[4,5] After purification, FtsZ, MinC, s1ZipA and s2ZipA were dialyzed against the working buffer, frozen and stored at -80 °C in 20 μL aliquots.

B.1.2.2 Synthesis of gold nanorods

A stock of gold nanorods (AuNRs) was synthesized as follows. Seeds were prepared by rapid addition of ice cold 0.01 M sodium borohydride to a solution of 0.1 mM HAuCl$_4$ (tetrachloroauric acid) and 25 mM CTAB (hexadecyltrimethyl ammonium bromide) under vigorous stirring. 1 mL of this seed solution was stirred into 1000 mL of growth solution

containing 0.1 M CTAB, 0.5 mM $HAuCl_4$, 0.6 mM ascorbic acid and 70 mM $AgNO_3$. The reaction was allowed to proceed for one hour at 30°C. The nanorods were separated from the excess of surfactant by centrifugation at 2,800 *g* for 20 min. Centrifugation was repeated twice, the supernatant was discarded each time and replaced with 0.05 M CTAB. The resulting gold nanorods have a width of 31.1 nm ± 5.6 nm and a length of 67.8 nm ± 9.2 nm (values are mean and standard deviation determined from TEM images of 486 particles, Figure B1).
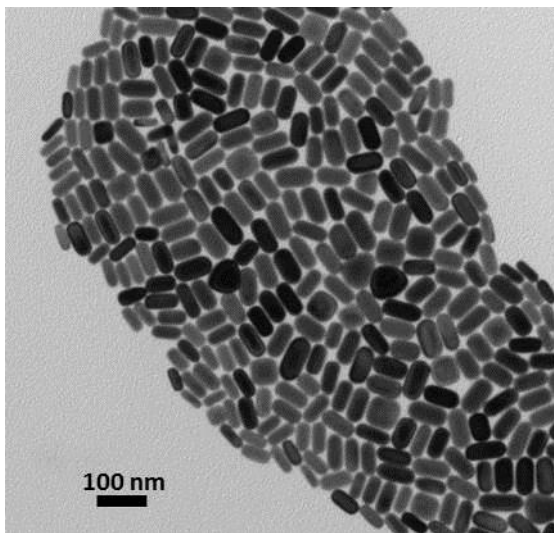
Figure B1. Transmission electron microscopy image of the gold nanorods used in our sensor. These rods have a width of 31.1 nm ± 5.6 nm and a length of 67.8 nm ± 9.2 nm (values are mean and standard deviation determined from 486 particles).

B.1.2.3 Particle functionalization

B.1.2.3.1 DNA Stabilization

500 µL of CTAB-stabilized gold nanorods were centrifuged at 6300 *g* for 5 minutes. After carefully removing the supernatant, the nanorods were resuspended for 10 minutes in a solution containing 5 µL of 500 µM T-Linker DNA-SH (5'-SH-TTTTTTTTTTT-3') with 5 µL of 100 mM TCEP and 20 µL of MilliQ water. Then 40 µl of 1% SDS solution were added to resuspend nanorod aggregates. After an additional centrifugation step, a pellet of nanorods was incubated for 1 hour in a solution containing 10 µL of 500 µM NH_2-DNA-SH (5'-SH-TTTTTTTTTTT-NH_2-3'), 10 µL of 100 mM TCEP, 30 µL of 1% SDS and 40 µL of MilliQ water. After one hour, 2 µL of 4 M NaCl were added to this mixture with gentle shaking and this step was repeated seven times. The resulting mixture was incubated overnight at room temperature.

B.1.2.3.2 Ni-NTA-functionalization

The DNA functionalized nanorods were cleaned from unreacted molecules by four centrifugation cycles (at 6300g for 5 minutes), re-suspension in PBS buffer, and in the last cycle reacted with 2µL of 1 mg/mL of isothiocyanobenzyl-NTA in 100 µL of PBS buffer (150mM NaCl) for 3 hours. After that, 10 µL of the NTA-functionalized nanorods were washed twice with 100 µL of MilliQ water and incubated for 10 min with 50 µL of 1 mM NiCl$_2$. The resulting NTA functionalized nanorod stock was stable for more than one month.

B.1.2.3.3 His-tagged protein immobilization

For the protein immobilization, we took 10µl of the Ni^{2+}-NTA functionalized nanorod stock, centrifuged once at 6300 g for 5 min, and incubated the pellet in 100 µL of 50 nM His-tag protein (s1ZipA, s2ZipA or MinC) solution for 10 minutes. The excess of unbound protein was left in the solution.

B.1.2.4 Optical characterization

UV-Vis-NIR spectra of the gold nanorods before and after each of the three functionalization steps described above are shown in Figure B2. Clearly visible are the two plasmon resonances of the short and long nanorod axis (at 518 nm and 639 nm). The plasmon shifts from the original CTAB rods at 639 nm, to 641 nm after DNA stabilization, to 643 nm after NTA coating and to 647 nm after protein immobilization. The slight redshift at each step was expected due to the increasingly larger molecular layer around the particle. In the UV region, the presence of the DNA, NTA and s1ZipA is visible by their characteristic resonances: DNA at 260nm, NTA at around 270 nm, and protein at around 280 nm.
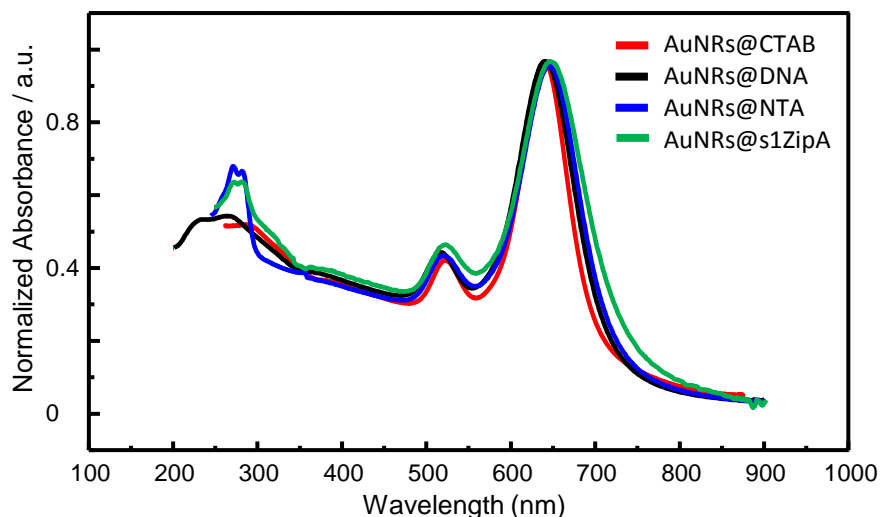
Figure B2. UV-vis-NIR spectra of gold nanorods covered with CTAB (red), DNA (black), NTA (blue), and s1ZipA (green).

B.1.2.5 Electroporetic characterization

Another check for stable particle functionalization is gel-electrophoresis, where an external electric field is used to drive particles in a gel (here, 0.5% w/v agarose). The migration speed depends on particle size and surface charge.[6] Figure B3 shows an unstained gel for nanoparticles with the following surface coverage: lane 1 with CTAB, lane 2 with DNA, lane 3 with NTA, lane 4 with Ni-NTA, and lane 5 with s2ZipA. The particles in lane 6 are the same as those in lane 5 but after treatment with imidazole. Lane 7 shows vitamin B_{12}, a commonly used indicator to correct for electroosmotic effects. The CTAB coated nanorods aggregate, indicating that CTAB does not stabilize the particles under the conditions of electrophoresis. All other particles migrate, demonstrating their successful stabilization. Their differences in mobility are too small for us to claim further insights.
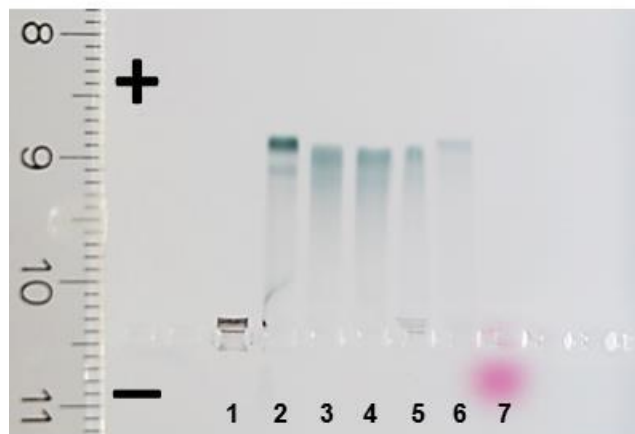
Figure B3. Electrophoretic mobility of nanorods.

B.1.2.6 Preparation of the sensor substrate

The microfluidic flow cell was constructed by two coverslips (the former one patterned to have three small holes on either ends while the latter was unpatterned) sandwiched together with a piece of Nescofilm (exhibiting channel patterns). The flow cell was mounted in a holder and thin tubings (acting as inlets and oulets) were connected to the holes in the patterned coverslip. The assembled flow cell was lodged onto the dark-field microscope stage. The channels in the flow cell were cleaned with a short rinse of 100 μL solution of 50% Hellmanex II in water. Then, His-tagged protein-functionalized AuNRs were injected and incubated until an adequate surface density of attached particles was reached. Particles were electrostatically immobilized by flushing the previously filtered working buffer in the flow cell and, at the same time, unbound nanoparticles and unbound protein were removed with this procedure. After rinsing with working buffer, we recorded the position of each deposited nanoparticle by taking a photograph of the entire field of view under dark-field illumination. Software identified bright spots and assigned them unique identification numbers. By flowing in one nanoparticle batch at a time, we know the specific functionalization of each particle in the field of view and group their responses accordingly.

B.2 Experiments

B.2.1 Titration experiments

To carry out the titration experiments of the three interacting partners (FtsZ-s1ZipA, FtsZ-s2ZipA and FtsZ-MinC), solutions with concentration from 100 nM to 300 μM of FtsZ were flushed through the flow cell until the sensor response reached an equilibrium value

after about 20 minutes. We used a flow rate of 30 µL/min to add the protein solutions, which should be high enough to avoid mass transport (diffusion) problems.

B.2.2 Sensor regeneration

The sensor was regenerated after s1ZipA binding by a treatment with a solution containing imidazole (800 mM) in buffer for 10 min. This treatment removes the His-tag protein from the interaction with Ni-NTA without deactivating the AuNRs@Ni-NTA. A 15 min rinse with working buffer removed the imidazole.

B.2.3 SPR experiments

SPR measurements were conducted on Reichert SPR Instrument to check the K_D values obtained by NanoSPR. The NTA-functionalized sensor chips (NIHCx) were purchased from Xantec Bioanalytics GmhB. Only one channel of the dual channel instrument was functionalized with His-tagged proteins, the second channel served as reference. The titration experiments were carried out following the method described by Schuck[7] in the working buffer described in the materials section (Figure B4). In three separate experiments, we tested the interaction of FtsZ with a) s1ZipA, b) s2ZipA and c) MinC.
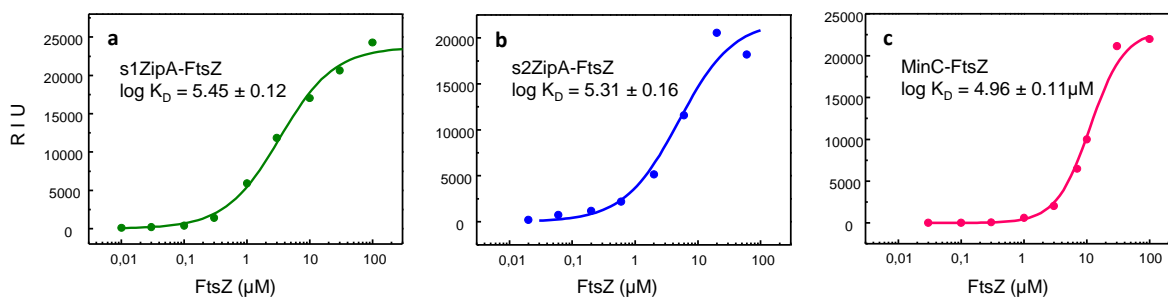
Figure B4. SPR titration curves. The values of RIU (corrected against the reference channel) in equilibrium are shown as function of FtsZ concentration as dots. The line shows Langmuir isotherms fitted to the experimental data. The fits can be used to extract K_D values (insets).

References

1. Rivas, G.; López, A.; Mingorance, J.; Ferrandiz, M. J.; Zorrilla, S., Minton, A. P.; Vicente, M.; Andreu, J. M. *J. Biol. Chem.* **2000***, 275, 11740–11749.

2. Ahijado-Guzmán, R.; Gómez-Puertas, P.; Álvarez-Puebla, R. A.; Rivas, G.; Liz-Marzán, L. M. *ACS Nano.* **2012**, 6, 7514-20.

3. Martos, A.; Alfonso, C.; López-Navajas, P.; Ahijado-Guzmán, R.; Mingorance, J.; Minton, A. P.; Rivas, G. *Biochemistry* **2010,** 49, 10780-7.

4. Hernández-Rocamora, V. M.; García-Montanés, C.; Reija, B.; Monterroso, B.; Margolin, W.; Alfonso, C.; Zorrilla, S.; Rivas, G. *J. Biol. Chem.* **2013,** 288, 24625-35.

5. Shiomi, D.; Margolin, W. *J. Bacteriol.* **2007**, 189, 236–243.

6. Hanauer, M., Pierrat, S., Zins, I., Lotz, A., Sönnichsen, C. *Nano Lett.* **2007**, 7, 2881-2885.

7. Schuck, P., Millar, D. B., Kortt, A. A. *Anal Biochem*. **1998**, 265, 79-91.

C. Plasmonic Core-satellites as Highly Sensitive Refractive Index Sensors

C.1. Materials and Methods

C.1.1 Synthesis of core-satellite nanostructures

Gold core-satellite structures (Au-CS) were assembled by a novel 'hydroxylamine mediated assembly method'. In a typical procedure, we centrifuged 500μL of large citrate stabilised gold spheres (60 nm, BBI International) at 2,460g for 5 min and resuspended them in 200 μL of 2 mM mPEG-SH (5000g/mol, Iris Biotech). The mixture was incubated overnight at room temperature to ensure complete PEGylation. To remove excess unbound PEG molecules, the particles were centrifuged down at 4,820g for 5 min, leaving a pellet of PEGylated gold nanoparticles at the bottom. The pellet was resuspended twice in 200 μl of deionized water and centrifuged down (at 4,820g for 5 min). After the last washing step, the pellet was diluted with 30 μL of water. Three such batches were prepared. Deionized water from a Millipore system (MilliQ) was used throughout. Next, 270 μL of small citrate stabilised gold spheres (20 nm, BBI International) were centrifuged in a separate microfuge tube at 4,820g for 10 min and the pellet was diluted in 10 μL of deionised water. Again three such batches were prepared. Each batch of 10μl 20 nm gold spheres were mixed together with a partner batch of 30 μl PEGylated 60 nm cores and vigorously stirred and incubated overnight on a shaking table. Finally, nanoparticle assembly into core-satellites was induced by adding 0.5, 0.75 and 1.0 μL of 70 mM Hydroxylamine into these three batches. All three samples were diluted to 100 μL after 10 min of reaction. After one hour, the volume of the reaction mixture was further diluted to 500 μL with water in order to deactivate remaining traces of hydroxylamine.

C.1.2 Particle Characterization

Optical extinction spectra ('UV-VIS') of core-satellite nanostructures (Au-CS), mPEG5000g/mol functionalised 60 nm gold spheres (60 nm cores) and mPEG500g/mol functionalised 80 nm gold spheres (80 nm cores) were recorded with a fiber optic spectrometer (Ocean Optics, USB2000) coupled to a tungsten light source (Ocean Optics,

FL-2000-FHSA) using a Spectro Pipetter (Ocean Optics). Low-resolution TEM images and cryo- TEM images of the core-satellite samples were acquired to investigate the number of satellites on core particles. Electrophoretic mobility of the core-satellite structures was determined in 0.3% Agarose gels (150V, 30 min) to verify the assembly strength under dynamic conditions. Photon correlation spectroscopy, both polarized and depolarized (PCS)[1] was used to record the hydrodynamic radius (R_h) and rotational radius (R_r) of 60 nm cores in different water-glycerol mixtures.

C.1.3 Ensemble sensitivity measurements

A quantitative comparison of the refractive index sensitivity of Au-CS, 60 nm cores and 80 nm cores was performed by systematically varying the refractive index of the solvent. To vary the refractive index, different water-glycerol mixtures were prepared. The refractive index (n) of the solvent was checked with a digital refractometer (Refracto 30PX). The plasmon resonance wavelength (λ_{res}) of the nanoparticles was determined for several changes in refractive index (n) with the fiber-optic spectrometer. The slope of the resulting linear trend gives the ensemble sensitivity of the nanostructures ($S_\lambda = \Delta\lambda_{res}/\Delta n$).

C.1.4 Single Particle Spectroscopy

To record the plasmon shifts ($\Delta\lambda_{res}$) of single nanoparticles, we use a dark-field microscope coupled to a spatially addressable liquid crystal display as an entrance to an imaging spectrometer, which allows the simultaneous investigation of many particles with high temporal resolutions (fastSPS).[2] The typical procedure involved rinsing a 1:20 diluted suspension of the nanoparticles for 5 min through a flat glass capillary connected to PET tubing. Subsequent rinsing with of 1 M NaCl solution for another 40 minutes immobilized the particles on the capillary walls. The glass capillary was then rinsed for 20 minutes with MilliQ water to remove excess salt and loosely bound particles. Now the setup recorded the reference scattering spectra of all the particles in the field of view, followed by a cyclic rinsing of the flow cell with water-glycerol mixtures having refractive indices of 1.34 and 1.38. In every cycle, the corresponding spectral shifts of each individual particle in the field of view were recorded. Only fully reversible spectral shifts were considered to quantify plasmonic sensitivity.

C.2 Experiments and Controls

C.2.1 Mechanism of core-satellite formation

The formation of core-satellite structures does not take place in the absence of hydroxylamine (Figure C1 a,b). No change in the ensemble spectra of 60nm cores occur, when measured before and after overnight co-incubation with 20nm satellites. The electrophoretic mobility also stays the same for 60nm cores, with unbound satellites migrating faster through the gel to form a separate band. This scenario changes only when hydroxylamine is present in the sample. Hydroxylamine has different effects on core and satellite forming particles. In separate sets of experiments, hydroxylamine was found to cause aggregation of the satellite forming particles (Figure C1c). The cores, however, demonstrated no color change at the same hydroxylamine concentration of 7mM. We believe that this aggregation results from the charge neutralization at the surface of 20nm satellite particles, since the same effect is observed also with other amines such as ammonia (Figure C1d). The extent of charge neutralization is dependent on the concentration of hydroxylamine added to the particles. Because of the neutralization process, the satellites lose their colloidal stability and tend to deposit onto the PEGylated 60nm cores. By carefully optimizing the ratio of the core and satellite mixtures (as well as the hydroxylamine concentration), we were able to reduce the amount of unbound 20nm nanoparticles and achieve a high yield of core-satellite nanostructures in solution.
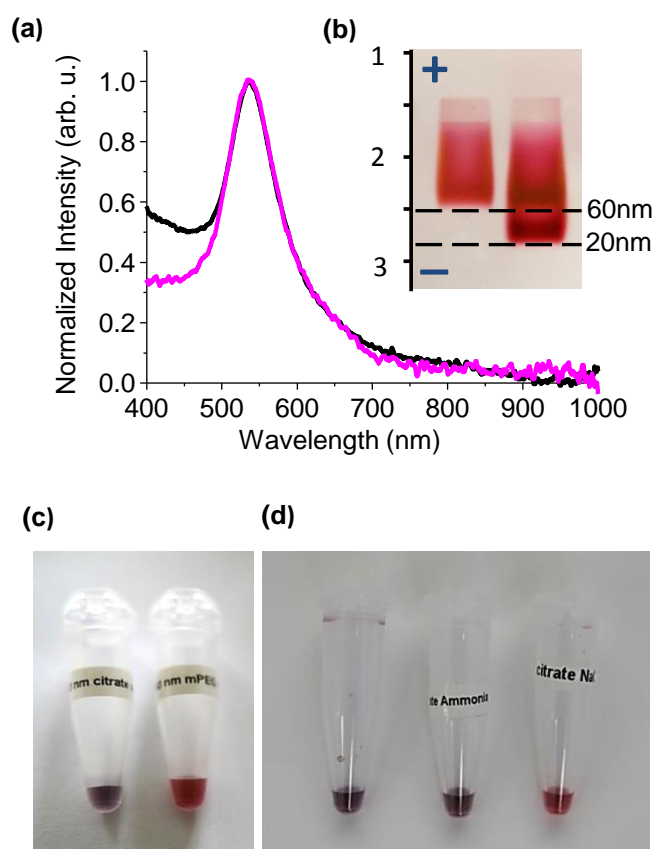
Figure C1. (a) Ensemble spectra of 60nm m-PEG coated cores in the absence of hydroxylamine before (black) and after satellite incubation (magenta). (b) Agarose gel-electrophoresis (0.3% agarose, 0.5x TBE, 150V, 30 minutes) of 60nm mPEG-coated cores and co-incubated cores and satellite forming particles. (c) Effect of Hydroxylamine separately on cores and satellite forming particles. Hydroxylamine leads to aggregation of citrate stabilized 20 nm gold spheres (7mM) visible from the purple color, whereas the m-PEG coated 60 nm cores remain unaffected. (d) Similar effect produced with 70mM ammonia, no effect with 70mM NaCl.

C.2.2 Resonance positions of cores and core-satellites

Size and shape of nanostructures have an impact on their sensitivity (S_λ). In order to demonstrate that the higher sensitivity of core-satellites is not just due to increase in their size (with respect to 60 nm cores), we included PEGylated 80nm cores in our study. Both 80nm cores and core-satellite nanostructures (Au-CS-St7) have exactly the same resonance maxima in water (Figure C2a). The resonance maxima for these two nanostructures shifts differently, when they are immobilized on the glass substrate for single particle measurements (Figure C2b). The change in the resonance maxima can be explained by the percentage of

nanostructure surface accessible to the surrounding media. Core-satellites have more surface area accessible to the surrounding media and therefore can have higher resonance maxima than 80nm cores on glass substrate.
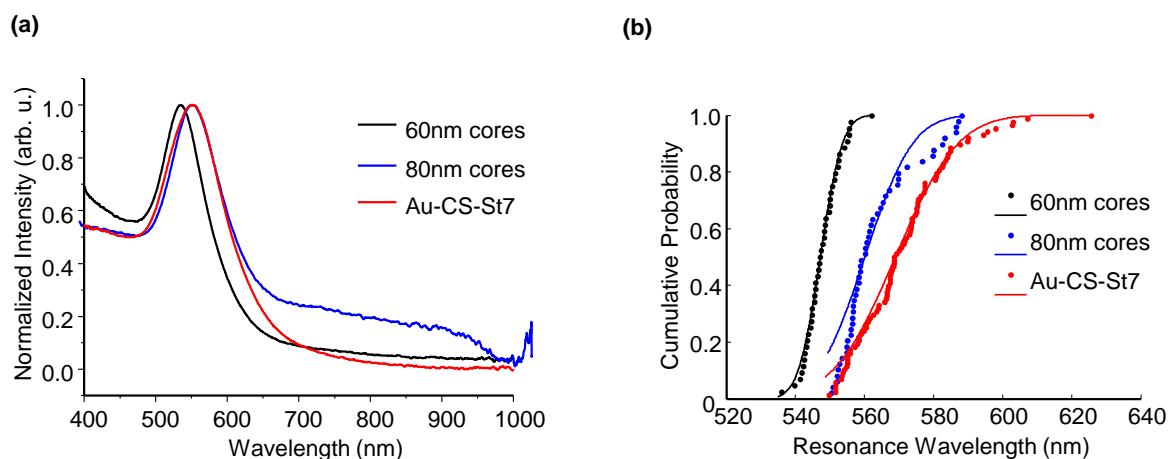
Figure C2. a) Ensemble spectra of 60nm mPEG-coated cores (black) and 80nm mPEG-coated cores (blue) gold nanospheres, as well as core-satellite assemblies (red, Au-CS-St7). The resonance position of both, 80nm spheres and core-satellites, is 14 nm red-shifted compared to the 60nm spheres. b) Distribution of the resonance positions measured in single-particle spectroscopy.

C.2.3 Effect of solvent on PEG linker

Photon correlation spectroscopy (PCS) was performed on 60 nm cores in three different refractive index solutions (1.33, 1.34 and 1.38) to determine whether glycerol (used in refractometric solutions) has any effect on the PEG linkers in the core-satellite nanostructures.[1] A sensitive index of possible conformational changes of PEG is the hydrodynamic R_h and rotational R_r radii. PCS experiments were performed at 20 °C using lasers with two different wavelengths $\lambda = 632$ nm (HeNe laser) and $\lambda = 532$ nm (Compass 215M, Coherent, Santa Clara, CA) to check possible heating effects (at 532nm). We have used both polarized (VV) and depolarized (VH) PCS to measure the translational $D_t=kT/(6\pi\eta R_h)$ and rotational $D_r= kT/(8\pi\eta R_h^3)$ diffusion coefficients, where k is the Boltzmann's constant, T is the temperature and η is the solvent viscosity: note the higher sensitivity of D_r to the size. For the VV scattering geometry, both the incident laser beam and the scattered light were vertically (V) polarized to the scattering plane. For the VH scattering the incident laser beam was vertically, while the scattered light was horizontally (H) polarized to the scattered plane were recorded.
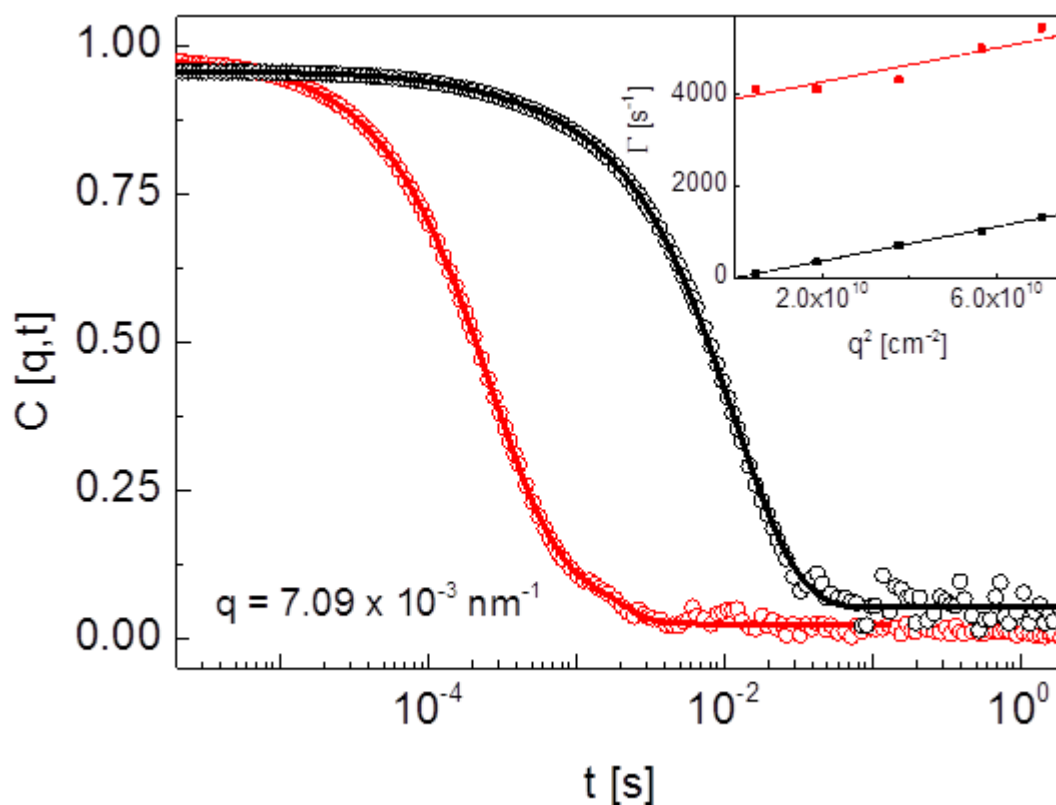
Figure C3. Relaxation functions for the translational $C_{VV}(q,t)$ and rotational $C_{VH}(q,t)$ dynamics of dilute 60 nm cores in glycerol/water with n=1.38 recorded at a the scattering wave vector q=7.09x10^{-3}nm^{-1} (scattering angle 30° and laser with 632nm) at 20°C. Inset: The linear q^2-dependence of the relaxation rates Γ_{VV} and Γ_{VH}.

Typical experimental relaxation functions C_{VV} (q,t) and C_{VH} (q,t) recorded at a scattering angle 30° (scattering wave vector q=7.09x10^{-3}nm^{-1} at 632nm) are shown in Figure D3 and the exponential decay rates $\Gamma_{VV} = D_t q^2$(solid squares) and $\Gamma_{VH} = 6D_r + D_t q^2$ are shown in the inset. The measured solvent viscosity, refractive and the two sizes obtained at two laser wavelengths for the three 60nm cores solutions are listed in Table C1. Clearly no solvent mediated collapse of PEG linker took place in these refractive index solutions as the characteristic dimensions of 60nm cores remained similar in all three cases, summarized in Table C1.On the average, R_h=39±0.5nm and R_r=44±0.5nm with ratio $\rho = R_r/R_h$=1.12. Clearly no measurable conformational change with variation of the solvent mixture is observed, hence excluding solvent mediated collapse of PEG linker. The deviation of the ratio ρ from one is due to the small asphericity of the 60nm core particle.[1]

Table C1. Characteristic dimensions (R_h= Hydrodynamic radius, R_r= Rotational radius) of 60nm cores at two wavelengths in refractive index (n) with viscosity (η).

60nm cores	R_h (632nm) [nm]	R_h (532nm) [nm]	R_r (632nm) [nm]	R_r (532nm) [nm]
n = 1.33 (η=1.00 mPa*s)	39.4 ± 0.2	38.7 ± 0.5	44.8 ± 0.9	42.7 ± 0.2
n = 1.34 (η=1.15 mPa*s)	39.3 ± 0.3	38.0 ± 0.5	45.3 ± 0.4	43.0 ± 0.3
n = 1.38 (η=2.87 mPa*s)	40.6 ± 0.3	39.7 ± 0.3	44.0± 0.8	42.6 ± 0.2

C.2.4 Single particle spectra core-satellites

The plasmon shifts ($\Delta\lambda_{res}$) of single nanoparticles were recorded with our fastSPS dark-field setup. A typical single particle spectrum is illustrated in Figure C4. These spectra were acquired in two different refractive indices (n=1.34 and n=1.38).
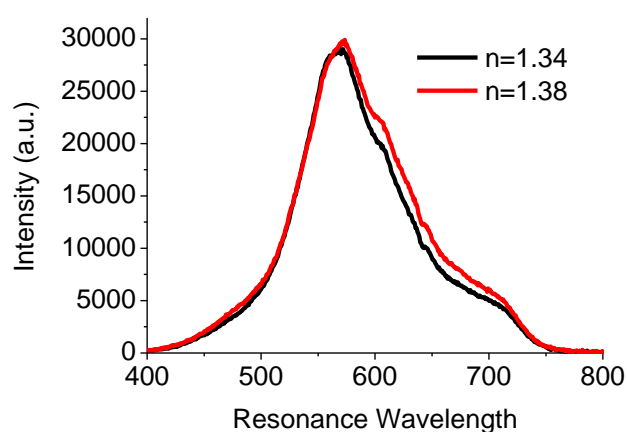
Figure C4. Single particle spectrum of a core-satellite nanostructure measured in two different refractive indices.

References

1. Koch, A. H. R.; Lévêque, G.; Harms, S.; Jaskiewicz, K.; Bernhardt, M.; Henkel, A.; Sönnichsen, C.; Landfester, K.; Fytas, G., Surface Asymmetry of Coated Spherical Nanoparticles. *Nano Letters* **2014**, *14*, 4138-4144.

2. Becker, J.; Schubert, O.; Sönnichsen, C., Gold Nanoparticle Growth Monitored in situ Using a Novel Fast Optical Single-Particle Spectroscopy Method. *Nano Letters* **2007**, *7*, 1664-1669

APPENDIX D

D. Plasmonic Gold Dimers for Probing Single Molecule Conformational Dynamics

D.1 Materials and Methods

D.1.1 Materials

Reagents, metallic salts, buffers streptavidin (66 kDa) and other analytical grade chemicals were acquired from Sigma-Aldrich or Merck. Deionized water from a Millipore system (> 18 MΩ, Milli Q) was used in all experiments. Thiolated methoxy PEG (MW: 2000 Da) , thiolated amine PEG (MW: 3000 Da) and dithiolated-PEG (MW: 5000 Da) were purchased from Iris Biotech. T-linker-DNA (5'-SH-TTTTTTTTTTT-3'), C18-T-linker-DNA (5'-SH-TTTTTTTTTTT-$(CH_2)_{12}O_6$-3'), T17-linker-DNA (5'-SH-TTTTTTTTTTTTTTTTT-3'), Amine-T-linker-DNA(5'-SH-TTTTTTTTTTT-NH_2-3') and Biotin-DNA (5'-Biotin- CTC ACG CTA CGA CTG ACA CCT TTTTTTTTTT -SH-3' and 5'-Biotin- $(T)_{40}$-SH-3') were purchased from Biomers.net GmbH. yeast Hsp90 was a generous gift from Prof. Dr. Thorsten Hügel (Technical University of Munich, Germany). yHsp90 protein was equilibrated against the working buffer (40mM Hepes, 150mM KCl, 10mM $MgCl_2$, pH 7.4).

D.1.2 Methods

D.1.2.1 Synthesis of gold nanospheres

Seed particle solutions were prepared by the standard citrate reduction method.[1] Briefly, 2.5 mL of a H[$AuCl_4$]$_3$.3H_2O solution (0.2% w/v) in 50 mL of water were heated to boiling and then preheated 2 mL of sodium-citrate solution (1% w/v) were added quickly under vigorous stirring. The solution was kept boiling for 5 min and was then allowed to cool down.The general procedure for growing the seeds was as follows. 3 ml of seed solution was placed into a three-necked flask. A 10 mL aliquot of gold growth solution (2 ml of 0.2% w/v of H[$AuCl_4$]$_3$.3H2O solution in 8 ml of MilliQ water), and 10 mL of the reducing solution (containing 0.25 ml of 1% w/v trisodium citrate and 0.5 ml of 1% w/v ascorbic acid in 9.25 ml of MilliQ water), were added to the seed solution at the rate of 0.222 ml/min at room temperature through Teflon tubes via a peristaltic pump under vigorous stirring. Directly after the addition was complete, the mixture was brought to boiling (at ~75-80 ^{o}C) and maintained

at this temperature for about 45 min. Finally the solution was allowed to cool down and UV/vis and TEM investigations (Figure D1) were carried out.
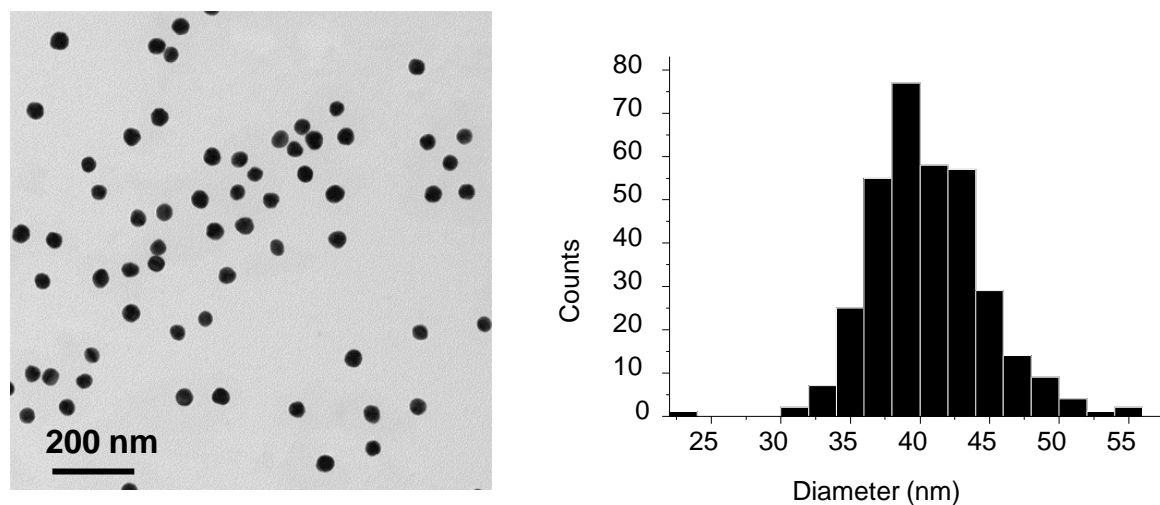
Figure D1. Transmission electron microscopy image of the gold nanospheres used in our sensor. These spheres have a mean diameter of 40 nm (determined from 341 particles).

D.1.2.2 Particle functionalization

### D.1.2.2.1 DNA functionalised gold spheres - Hsp90 conjugates

A 1mL solution of 40 nm citrate-stabilized gold nanospheres was centrifuged at 6300 *g* for 10 minutes. After carefully removing the supernatant, the spheres were resuspended in a solution containing 10 µL of 500 µM T-Linker DNA-SH (5'-SH-TTTTTTTTTTT-3'), 1µl of 167 µM amine-T-Linker DNA-SH (5'-SH-TTTTTTTTTTT-NH$_2$-3'), 5 µL of 100 mM TCEP and 30µl of MilliQ water. Then 35 µl of 1% SDS solution were added and the nanospheres were incubated for 1 hour. After one hour, 2 µL of 4 M NaCl were added to this mixture with gentle shaking and this step was repeated seven times. The resulting mixture was incubated overnight at room temperature. The spheres were centrifuged seven times to remove excess unbound DNA and finally resuspended in 500µl of MilliQ water. To carry out Hsp90 functionalisation, 30µl of these DNA functionalised gold nanospheres were centrifuged at 6300 g for 10 min. The pellet was then incubated in 100µl of 1mg/ml sulfo-SMCC solution (pH: 7.4) for 1.5 hours. The NHS part of SMCC reacts with amine terminated DNA and imparts maleimide moiety to this terminus. The spheres were centrifuged at 6300 g for 5 min and resuspended in 500µl of MilliQ water. Seven rounds of centrifugation were performed to remove excess sulfo-SMCC. The maleimide functionalised DNA-gold spheres are centrifuged one last time and the pellet is added to 5µM solution of Hsp90 (treated with 10mM TCEP for

1 hour). Hsp90 is allowed to react for 2 hours with the maleimde groups present on the DNA. The Hsp90-DNA functionalised gold nanospheres (Figure D2) are stored at -80°C for further use.
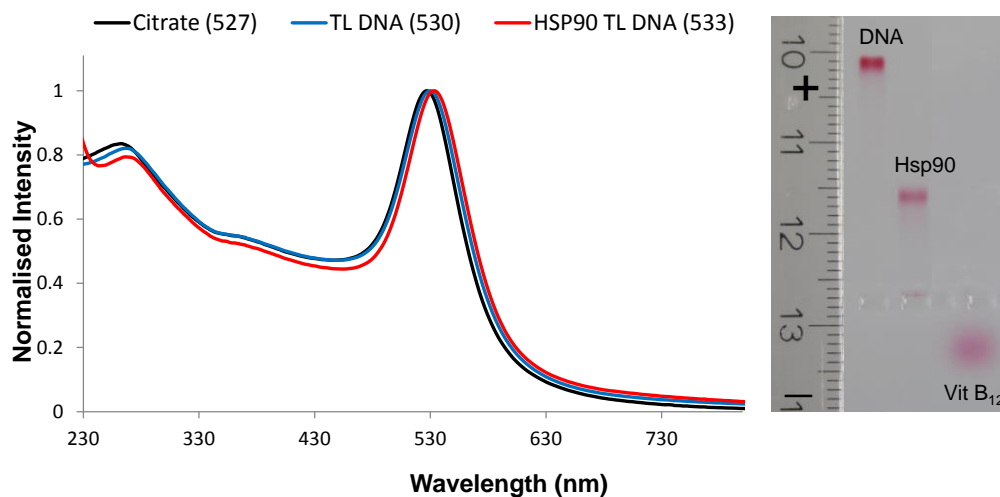
Figure D2. UV-vis-NIR spectra and agarose gel image of gold nanospheres covered with citrate (black), DNA (blue), and Hsp90 (red). A spectral shift of +3 nm was recorded after each functionalization step.

D.1.2.2.2 PEG functionalised gold spheres -Hsp90 conjugates

A 1ml solution of 40 nm citrate-stabilized gold nanospheres was centrifuged at 6300 *g* for 10 minutes. After carefully removing the supernatant, the spheres were resuspended in a solution containing 30 µL of 30 mM methoxyPEG-SH (MW: 2000g/mol), 1µl of 30 mM aminePEG-SH (MW: 3000g/mol) and 70 µL of 100 mM TCEP. The resulting mixture was incubated overnight at room temperature. The PEG functionalised spheres were dialyzed for 24 hours in pure-a-lyzer dialysis tube (cutoff MW: 100 kDa) and then centrifuged at 6300 g for 10 minutes. The pellet was resuspended in 500µl of MilliQ water and stored at 4°C. To carry out Hsp90 functionalisation, 30µl of these PEG functionalised nanospheres were centrifuged at 6300 g for 10 minutes. The pellet was then incubated in 100µl of 1mg/ml sulfo-SMCC solution (pH: 7.4) for 1.5 hours. The NHS part of SMCC reacts with amine terminated PEG and imparts maleimide moiety to this terminus. The spheres were centrifuged at 6300 g for 5 min and resuspended in 500µl of MilliQ water. Seven rounds of centrifugation were performed to remove excess sulfo-SMCC. The maleimide functionalised PEG-gold spheres are centrifuged one last time and the pellet is added to 5µM solution of Hsp90 in buffer A (40mM Hepes, 150mM KCl, 10 mM $MgCl_2$, pH: 7.4) treated with 10mM TCEP for 1 hour).

Hsp90 is allowed to react for 2 hours with the maleimide groups present on the PEG. The Hsp90-PEG functionalised gold nanospheres are stored at -80°C for further use.

D.1.2.2.3 Biotin-DNA functionalised gold spheres

A 1 mL solution of 40 nm citrate-stabilized gold nanospheres was centrifuged at 6300 g for 10 minutes. After carefully removing the supernatant, the spheres were resuspended in a solution containing 10 μL of 500 μM T-Linker DNA-SH (5'-SH-TTTTTTTTTT-3'), 1μl of 500 μM Biotin- DNA-SH (5'-Biotin -(T)$_{40}$-SH -3') , 5 μL of 100 mM TCEP and 30μl of MilliQ water. Then 35 μl of 1% SDS solution were added and the nanospheres were incubated for 1 hour. After one hour, 2 μL of 4 M NaCl were added to this mixture with gentle shaking and this step was repeated seven times. The resulting mixture was incubated overnight at room temperature. The spheres were centrifuged seven times to remove excess unbound DNA and finally resuspended in 500μl of MilliQ water and stored at 4°C for further use.

D.1.2.2.4 Dithiol-PEG functionalised gold spheres

A 1ml solution of 40 nm citrate-stabilized gold nanospheres was centrifuged at 6300 g for 10 minutes. After carefully removing the supernatant, the spheres were resuspended in a solution containing 30 μL of 30 mM methoxyPEG-SH (MW: 2000g/mol), 1μl of 30 mM SH-PEG-SH (MW: 5000g/mol) and 70 μL of 100 mM TCEP. The resulting mixture was incubated overnight at room temperature. The PEG functionalised spheres were centrifuged twice at 6300 g for 10 minutes. The pellet was resuspended in 500μl of MilliQ water and stored at 4°C.

D.1.2.2.5 Streptavidin functionalised gold spheres

In order to bind streptavidin covalently to the 40 nm gold nanospheres, disulfide groups are introduced to the protein via 3,3´-Dithiobis(sulfosuccinimidylpropionate) (DTSSP, Pierce). 50 μl of a 1 mg/ml streptavidin solution (Sigma) in phosphate buffered saline (PBS, 0.01 M, Sigma) are incubated for 30 minutes at room temperature with 50 μl 0.3mM DTSSP in PBS. Afterward, the unreacted DTSSP is removed with a Zeba Spin Desalting Column 7K MWCO (Pierce). To clean the gold nanoparticles from their storage solution, 500 μl are centrifuged (6300 g, 5min) and the supernatant is removed. 50 μl of the modified streptavidin was added and the spheres and the mixture was incubated at 4°C overnight (Figure D3). The streptavidin functionalised gold nanoparticles were centrifuged at 6300 g for 5 minutes and the resulting pellet was diluted in PBS buffer and stored at 4°C for further use.
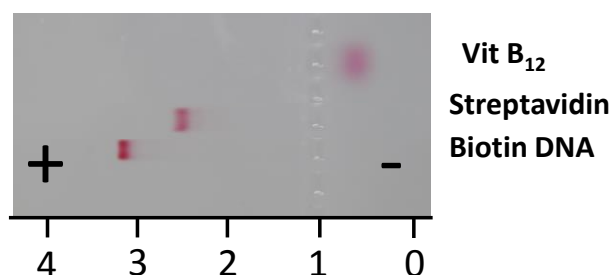
Figure D3. Electrophoretic mobility of 40 nm gold nanospheres functionalised with biotinylated DNA and DTSSP-streptavidin in 0.3% agarose gel (150V, 30 min).

D.1.2.3 Flow cell surface passivation

D.1.2.3.1 Passivation with BSA

We use a flow cell consisting of two cover slips held together by a piece of Nescofilm with a void area. One cover slip has two small holes for the connection of thin tubings as in- and outlet. The flow cell was cleaned by rinsing with 100 µL of 50% Hellmanex II special cleaning concentrate and then with 12 mL of MilliQ water. Then, the flow cell surface was shortly rinsed with 300µL of 100mM sodium acetate buffer (pH: 5.0). A 10mg/ml solution bovine serum albumin (BSA) in 100mM sodium acetate buffer (pH: 5.0) was prepared and filtered with a 20µm pore size filter (VWR). The flow cell was rinsed with 500µL of freshly prepared BSA solution and incubated in BSA solution for 1 hour.

D.1.2.3.2 Passivation with cross-linked BSA

The flowcell surface was passivated with BSA in sodium acetate buffer as mentioned earlier. 1 ml of 1% v/v Glutaraldehyde solution was prepared in PBS buffer (pH: 7.4) and flushed through the passivated flow cell carefully to avoid bubble formation. Glutaraldehyde was allowed to react overnight with the amines present on the BSA and bridge them together. Excess glutaraldehyde was removed by rinsing the flow cell with 7mL of MilliQ water.

D.1.2.3.3 Passivation with Pluronic F-127

In order to passivate the coverslips, the glass surface was cleaned with 2% Hellmanex solution for 2 hours under constant sonnication. The coverslips were washed with copious amounts of MilliQ water and dried under N2 atmosphere. The dried coverslips were exposed to air plasma for 4 min. On the plasma cleaned glass surfaces, HMDS (Heamethyldisilazane) vapors were deposited at 170°C for 4 hours to make the surface hydrophobic .The coverslips

were then assembled together by a piece of Nescofilm with a void area. The resulting flow cell was rinsed with 500µl of alkaline solution of 5mg/ml Pluronic F-127 (dissolved in 1M NaOH and sonnicated for 30 minutes) for 10 minutes and incubated further for another 30 minutes. Excess pluronic was dicarded by rinsing the flow cell 5 times with MilliQ water.

D.1.2.3.4 APTES passivation

In order to passivate the glass surface, the coverslips were cleaned in piranha solution (3 volumes H_2SO_4: 1 volume H_2O_2) for 4 hours at 60^oC. Cleaned coverslips were rinsed with copious amount of MilliQ water and dried under N_2 atmosphere. APTES vapours were deposited onto the coverslips (at 170^oC, 10mbar) for 30 minutes.[2] The coverslips were then assembled together by a piece of Nescofilm with a void area. Amine groups on the APTES modified coverslips were reacted with carboxyl-PEG (MW: 5000g/mol) overnight in 200mM EDC and 50mM NHS solution (pH: 5.0).

D.1.2.4 Dark Field setup

D.1.2.4.1 Setup improvements

We equipped a Zeiss Axio Observer Z1 inverted microscope with a PI542 XY-piezo stage (200 µm x 200 µm, closed-loop) and a PI721 Z-piezo (100 µm, closed-loop). Furthermore, for VIS-NIR-spectroscopy, we added an Imspector V10E transmissive imaging spectrograph with an Andor Luca R EM-CCD. The true colour images are taken with a Canon EOS 5D Mark II (IR-filter removed). For the automated acquisition and analysis of many single particle spectra, we used MATLAB based control software.

The particle positions are saved with the spectra allowing to identify changes of plasmon peaks for each particle individually after the surrounding of the particles is altered. Particles that have a corrupt spectrum (no clear resonance peak) or are simply lost due to the exchange of solutions are sorted out in subsequent measurements.

A measurement consists of 3 steps:

1. Acquisition of a true colour image.
2. Recognition of the bright spots in the image.
3. Acquisition of spectra of each bright spot including automated position refinement in X-position and Z-position (autofocus).

D.1.2.4.2 Thermal stability of Dark-Field setup

To record the temperature on the flow cell region due to the heat of light source, we connected a thermo-sensor (Picolog recorder) onto the glass coverslip. An additional port was connected to a region far away from the microscope area to check the temperature increase in the surroundings. The temperature was recorded over duration of 24 hours with an acquisition rate of 2 seconds. Figure D4 shows an increase in the temperature at the flow cell region to 27-28°C within 3 hours. No significant increase in temperature could be observed over time after the initial increase period.
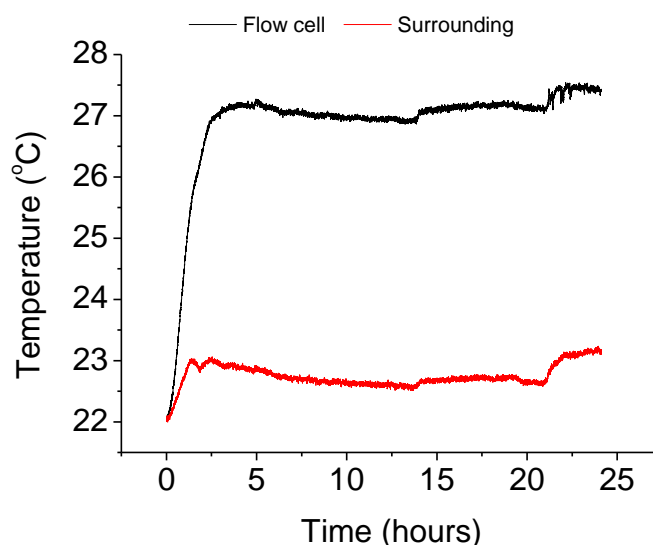
Figure D4. Temperature variation recorded by picolog recorder at the flow cell region (black) and surrounding region away from the microscope region (red).

D.2 Experiments and Controls

D.2.1 Dimer formation and measurements

D.2.1.1 Formation of DNA-Biotin-Streptavidin Dimers

The flow cell channel was passivated with BSA as mentioned elsewhere. Streptavidin functionalized 40 nm gold nanospheres in PBS buffer (pH: 7.4) were immobilized into the passivation defects. Unbound nanoparticles were washed away by short rinse with PBS buffer. The flow cell was rinsed and incubated with biotin-DNA functionalized 40 nm gold nanospheres in PBS buffer (with 1mg/ml of BSA protein) for 20 minutes. Unbound DNA-functionalised particles were removed by rinsing with PBS buffer for 30 minutes. The nanoparticle contaminated PBS buffer was changed after every 10 minutes. The dimerisation

efficiency of 100% was observed for purely biotinylated DNA functionalized gold nanospheres, whereas only ~30% dimerisation efficiency was observed with 1:10 ratio of biotinylated DNA and T-linker DNA (Figure D5)

(a)   (b)
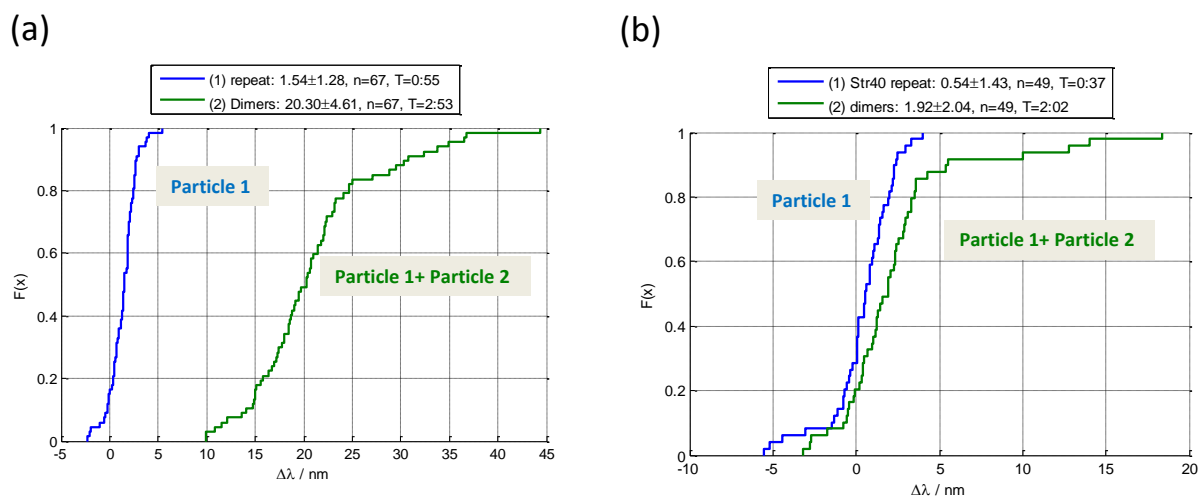
Figure D5. Dimerisation efficiency for biotinylated DNA and streptavidin linked gold dimers with (a) 100% biotinylated DNA functionalized gold spheres (b) functionalized with 10% biotinylated DNA.

D.2.1.2 Response of DNA tethered Dimers to changes in ionic strengths

We investigated the effect of buffer ionic strength on the DNA linked gold dimers (prepared with mixed monolayer of biotinylated and T-linker DNA in 1:10 ratio). It is known that cations present in the buffer mask the negative charge of the DNA backbone, leading to the contraction of DNA.[3] Cyclic changes of the surrounding medium from PBS (0.01M, pH 7.4) to water (pH 7.4) leads to an expansion in the persistent length of the DNA molecules and vice versa. The effect can be monitored by tracking the concomitant blue shift in the resonance spectra of DNA-linked gold dimers (Figure D6). Three cycles of solvent exchanges were performed. A slightly upward trend in the time trace was also observed over the measurement time. This could be due to small drifts in the peizo stage or building up of ionic shell around the particle pairs.
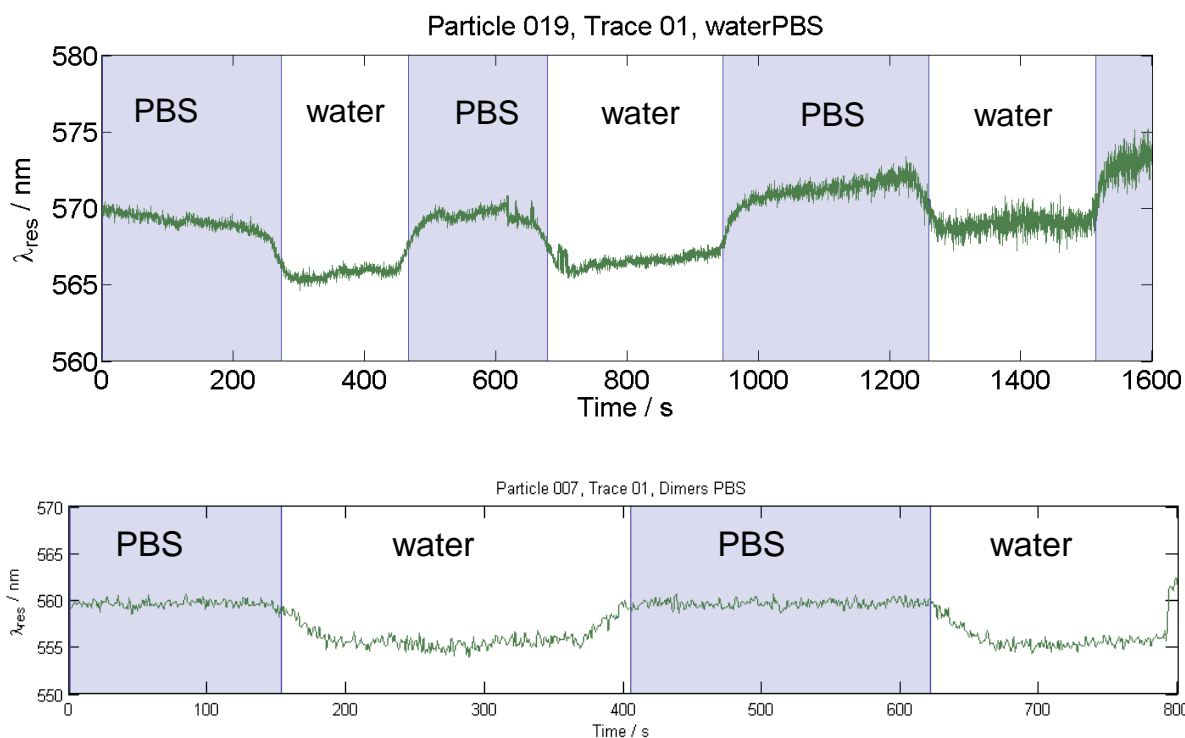
Figure D6. Response of two DNA linked gold dimer to cyclic changes in the ionic strength of the surrounding medium. At higher ionic strength the charges on the phosphate backbone of DNA is masked, leading to shrinking of DNA and red shift in resonance wavelngth due to stronger plasmon coupling within the dimer.

D.2.1.3 Response of DNA tethered Dimers in static ionic strength

Several DNA linked gold dimers were measured in tandem to observe their behaviour over duration of 30 minutes. Time traces were collected in real time by dark-field setup with the temporal resolution of 100 ms at 28°C setup temperature. No large changes in spectral shifts were observed with DNA dimers in PBS buffer. The resonance position of the dimer spectra did not change by 0.5-0.7 nm, which is within the noise level of our setups. Histograms in figure D7 show the distribution of resonance maxima of the dimers during the measurement period of 30 minutes.
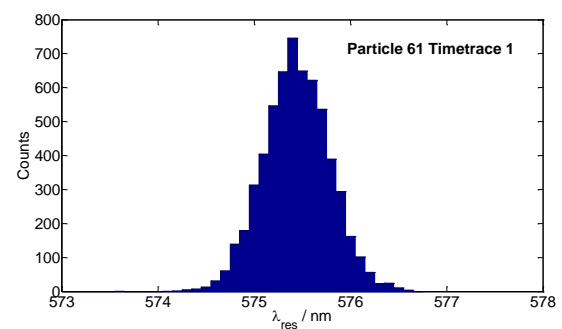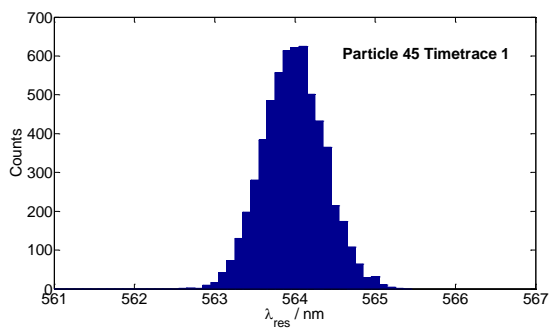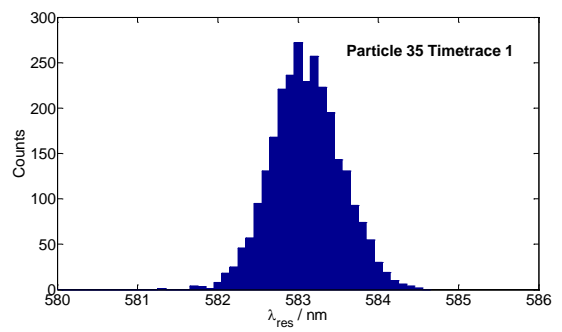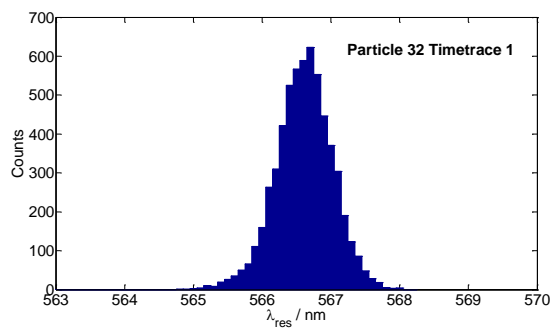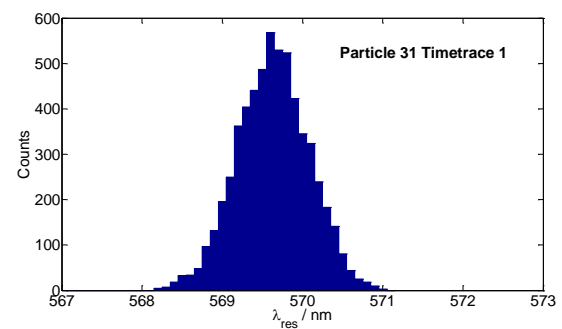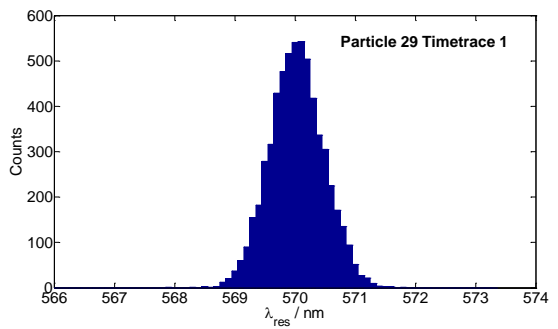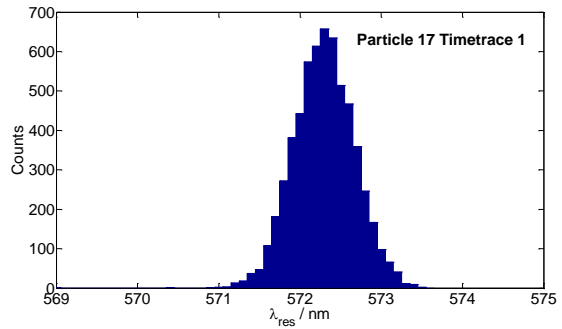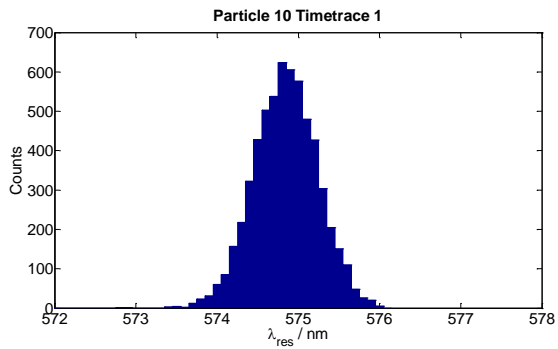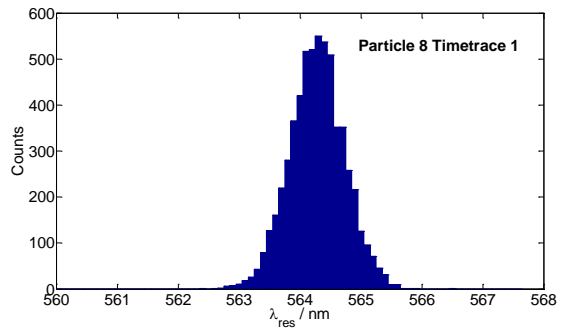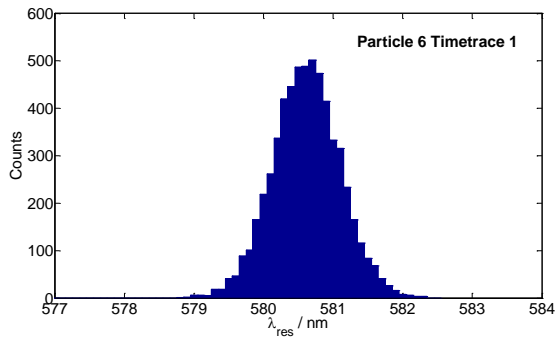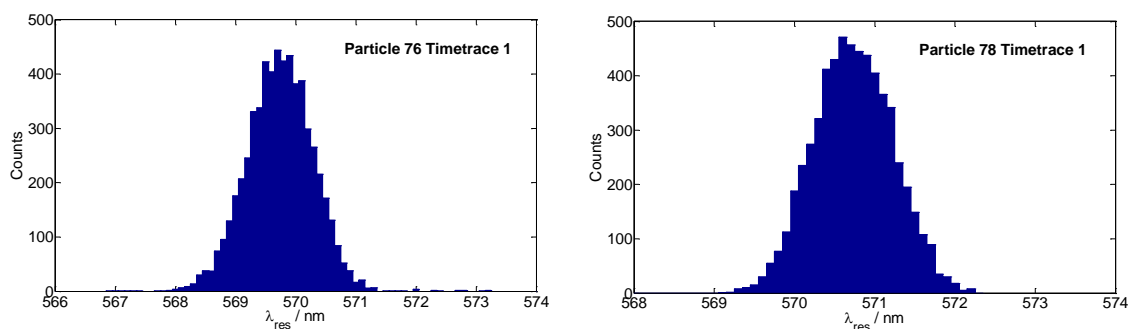
Figure D7. Histograms showing the change in resonance position of DNA linked gold dimer over 30 minutes duration in PBS buffer. At constant ionic strength no significant fluctuations in the spectral shifts were observed.

D.2.1.4 Formation of DNA-Hsp90-Biotin-Streptavidin Dimers

The flow cell channel was passivated with BSA as mentioned elsewhere. Biotin-Hsp90-DNA functionalized 40 nm gold nanospheres in buffer A (40mM Hepes, 150mM KCl, 10mM $MgCl_2$, pH: 7.4) were immobilized into the passivation defects. Unbound nanoparticles were washed away by short rinse with buffer A. The flow cell was rinsed and incubated with streptavidin functionalized 40 nm gold nanospheres in buffer A for 30 minutes. Unbound streptavidin-functionalised particles were removed by rinsing with buffer A for 30 minutes. The nanoparticle contaminated buffer A was changed every 10 minutes. The dimers were measured in buffer A to record thermally driven conformational changes in Hsp90.

D.2.1.5 Optimisation of Dimerisation efficiency

The number of dimers (and higher order structures) was minimised by tuning the ratio of amine-DNA-SH to DNA-SH on gold nanospheres. Based on prior knowledge with DNA-streptavidin dimers (Figure D5), four different combinations (1:25, 1:35, 1:40, 1:50) were investigated. The dimerization (or first and second particle conjugation) efficiency reduced from 25% dimers (1:25 ratio) down to 0% dimers (1:50 ratio). 1:35 ratio of biotin-Hsp90-DNA to DNA-SH gave the lowest possible dimers within 30 minutes of incubation with streptavidin functionalised gold spheres (Figure D8). We believe that in this proportion there is minimum probability of forming dimers with multiple tethers. This ratio was chosen for the all the experiments made thereafter.
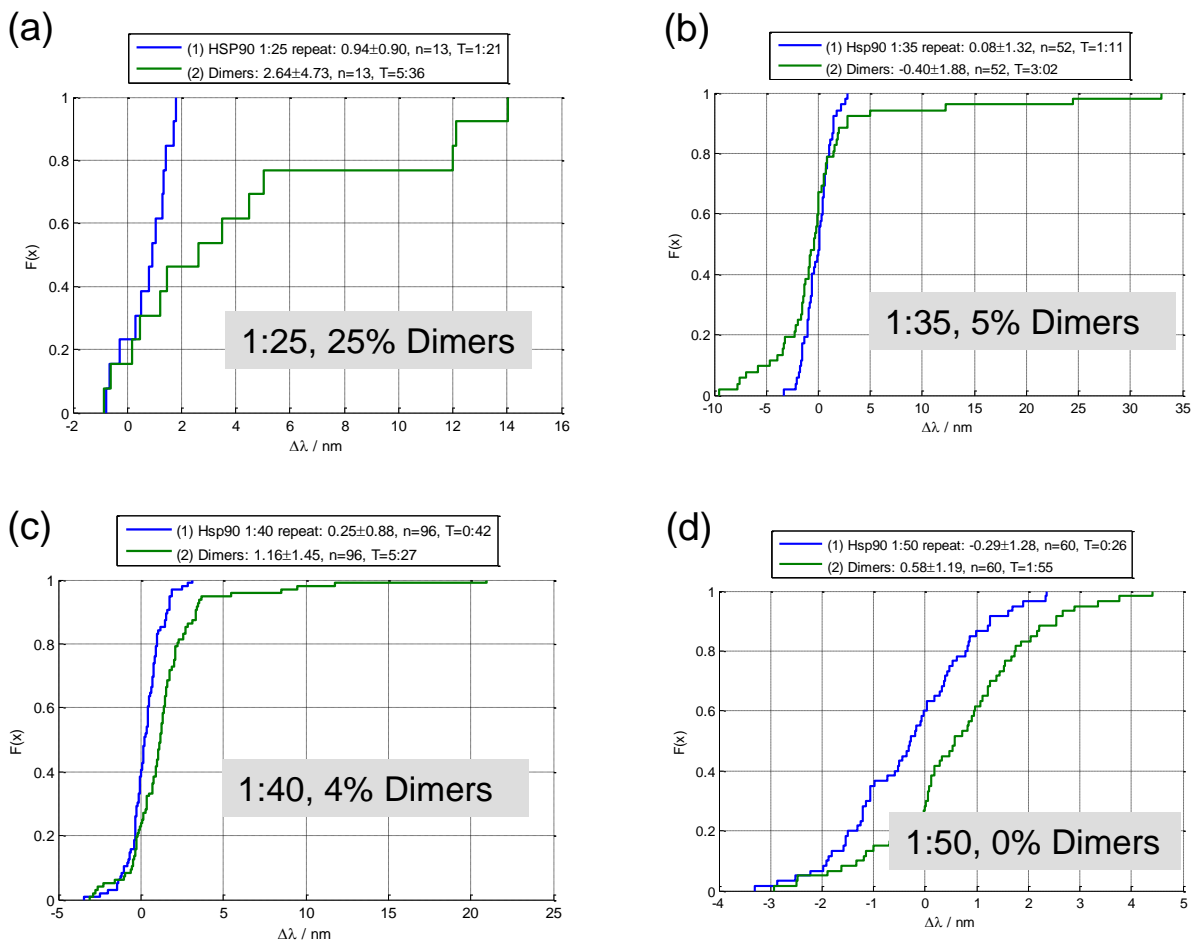
Figure D8. Cumulative probability distribution plots showing dimerization efficiency with Hsp90-DNA and T-linker DNA ratios (a) 1:25 (b) 1:35 (c) 1:40 (d) 1:50. The incubation period was 30 minutes in (a,b) and 3 hours in (c,d).

D.2.1.6 Response of DNA-Hsp90-Biotin-Streptavidin tethered dimers

Several Hsp90-DNA linked gold dimers were measured in tandem to observe their behaviour over duration of 30 minutes. Time traces were collected in real time by dark-field setup with the temporal resolution of 100 ms at 28°C setup temperature. No large changes in spectral shifts were observed with Hsp90-DNA dimers in buffer A. The resonance position of the dimer spectra did not change by 0.5-0.7 nm, which is within the noise level of our setups. Histograms in figure D9 show the distribution of resonance maxima of the dimers during the measurement period of 30 minutes. It could happen that the thermal fluctuations are Hsp90 is not observed probably because the end-to-end separation within the dimer is too high (~ 22 nm) that the fluctuations are somehow hidden within the noise level of the setup. Multiple non-specific interactions at the nanoparticle surface compromising the flexibility of Hsp90, could be another reason behind lack of conformational dynamics in Hsp90.
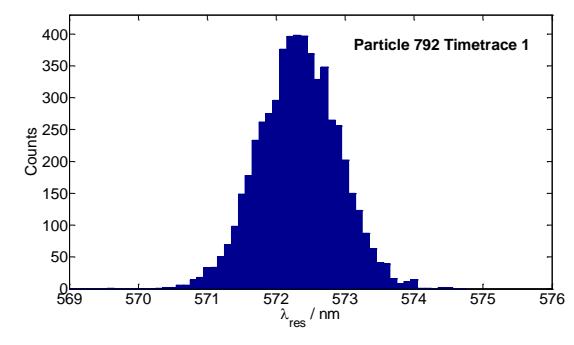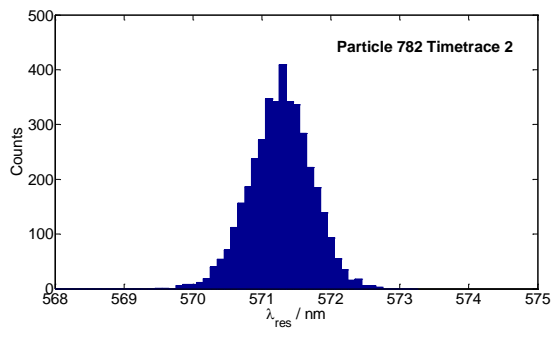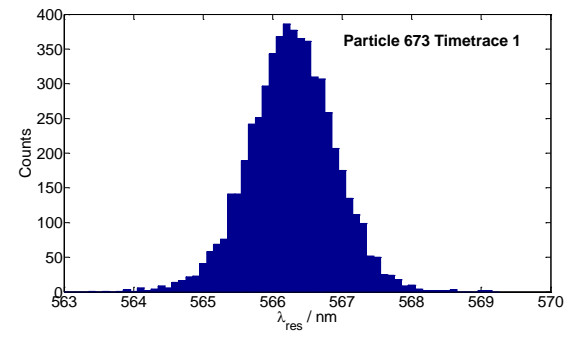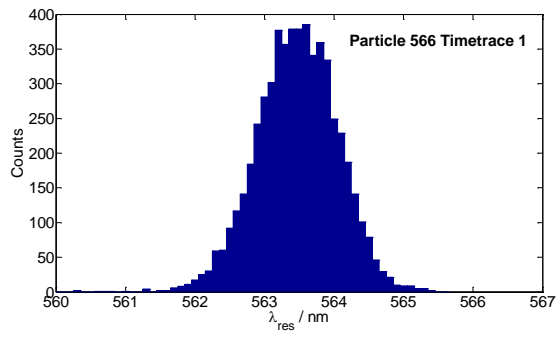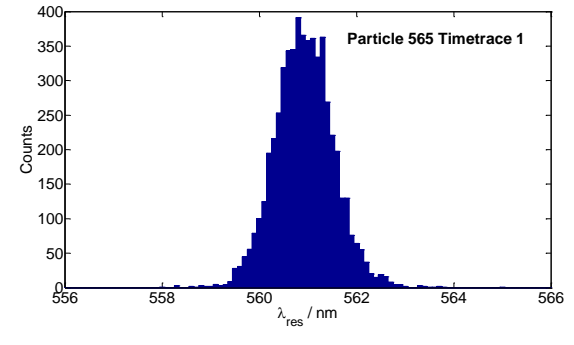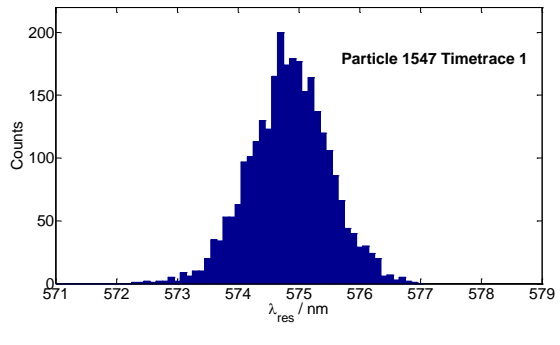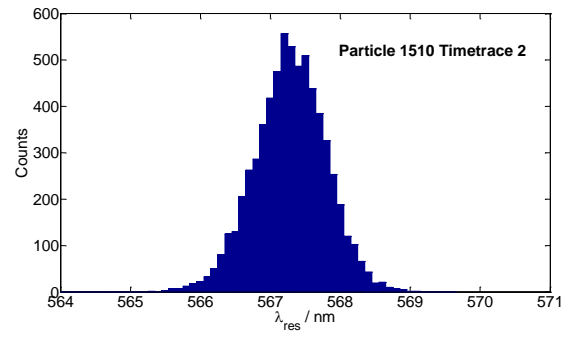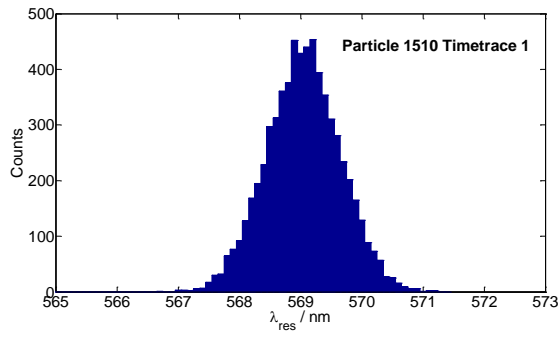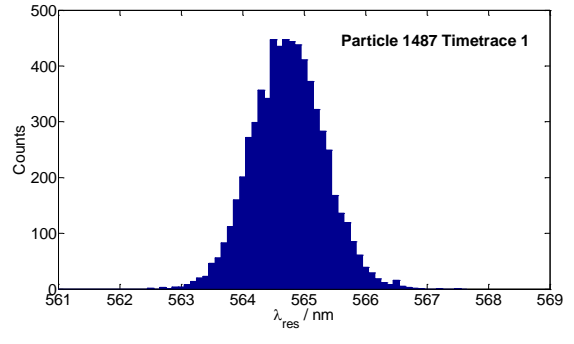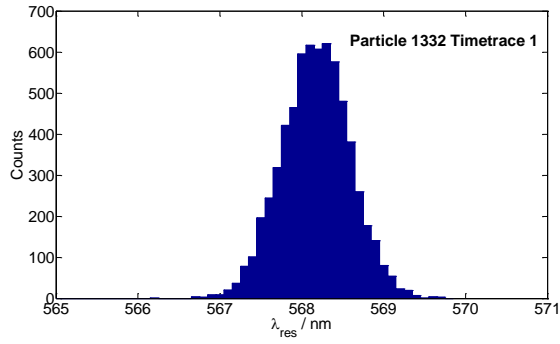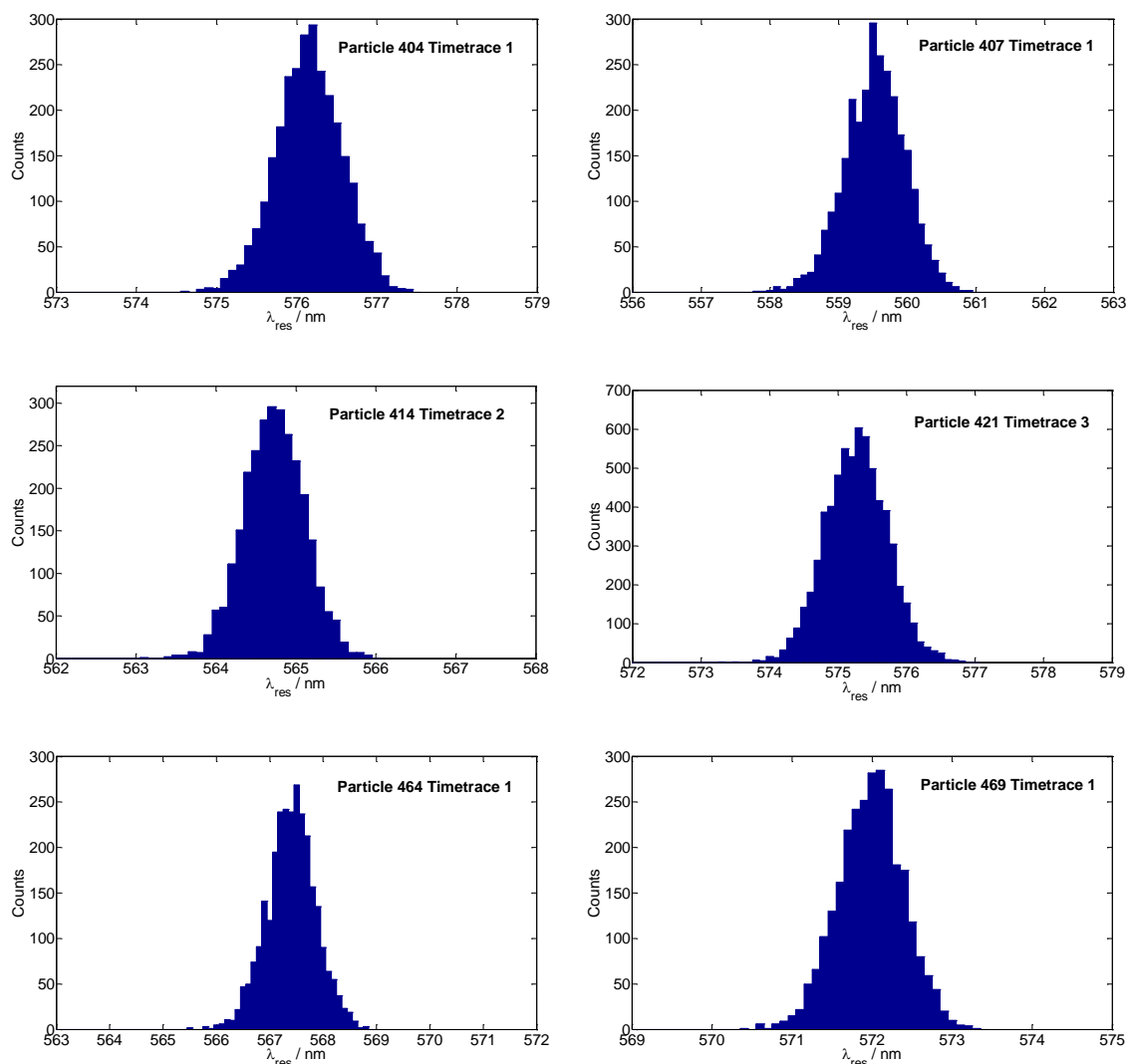
Figure D9. Histograms showing the change in resonance position of Hsp90-DNA linked gold dimer over 30 minutes duration in buffer A. At constant ionic strength no significant fluctuations in the spectral shifts were observed.

D.2.1.7 Studying Hsp90 interaction with functionalised particles

Electrophoretic mobility of DNA, DNA-PEG and PEG functionalised particles in the absence and presence of Hsp90 was studied by agarose gel electrophoresis. DNA functionalised gold nanospheres showed marked decrease in their electrophoretic mobility after 2 hours incubation with 5μM Hsp90 in buffer A. Similar changes were observed on C18 spacer-DNA and DNA-PEG mixed monolayers. The reduced mobility could arise from either non-specific interaction of Hsp90 with the DNA molecules[4] or from ligand exchange reaction onto the nanoparticle surface. There was no interaction observed between Hsp90 and PEG functionalised gold nanospheres under similar conditions (and even after 48 hour long co-incubation period). Thus, we believe that the ligand exchange has little role to play here and the decrease in mobility of DNA particles with Hsp90 is due to DNA protein interaction

(Figure D10). Since Hsp90 is also known to interact non-specifically with partially denatured proteins (like monomeric avaidin),[5] we chose not to use streptavidin-functionalised gold nanospheres as the second particle for dimer preparation.
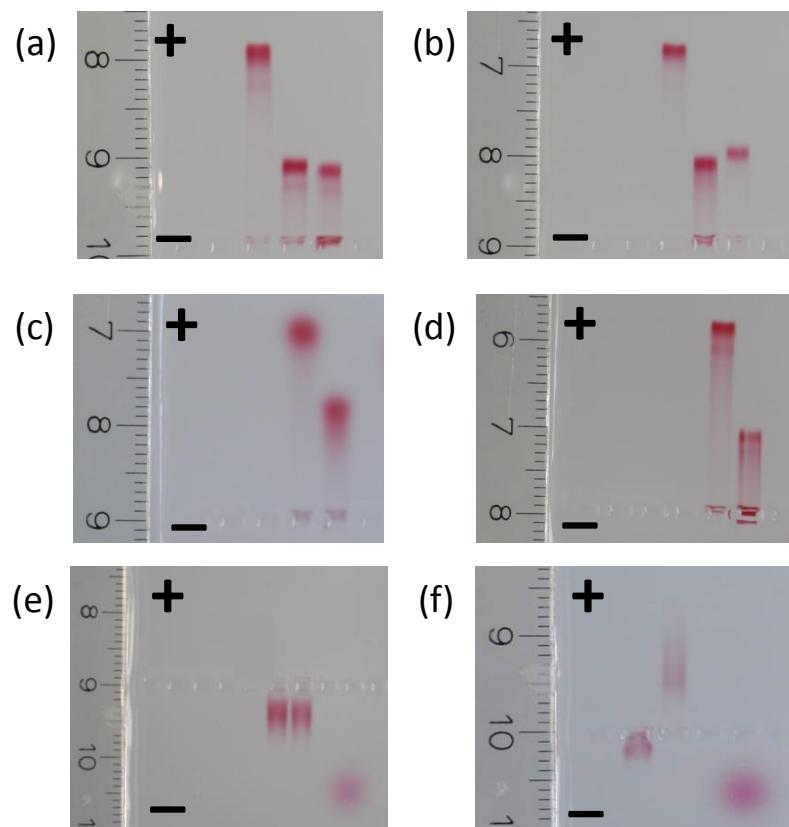
Figure D10. Agarose gel electrophoresis showing non-specific interaction of Hsp90 with (a) surfactant mediated T-linker DNA functionalised gold nanospheres; lane 1: DNA, lane 2-3: DNA incubated with Hsp90 (b) surfactant mediated C18spacerT-linker DNA functionalised gold nanospheres; lane 1: DNA, lane 2-3: DNA incubated with Hsp90 (c) surfactant mediated C18spacerT-linker DNA and PEG (1:1) functionalised gold nanospheres; lane 1: DNA-PEG, lane 2: DNA-PEG incubated with Hsp90 (d) surfactant free T-linker DNA functionalised gold nanospheres; lane 1: DNA, lane 2: DNA incubated with Hsp90. 3 with biotinylated DNA and DTSSP-streptavidin in 0.3% agarose gel (150V, 30 min). (d) No non-specific interaction was observed on PEG functionalised gold nanospheres; lane 1: PEG, lane 2: PEG incubated with Hsp90. (e) Hsp90 is linked to the SMCC modified amine termini of PEG functionalised gold nanospheres; lane 1: PEG, lane 2: PEG-SMCC incubated with Hsp90.

D.2.1.8 Formation of PEG-Hsp90-PEG Dimers

The flow cell channel was passivated with crosslinked BSA or APTES-PEG as mentioned elsewhere. Hsp90-PEG functionalized 40 nm gold nanospheres in buffer A (40mM Hepes, 150mM KCl, 10mM MgCl$_2$, pH: 7.4) were immobilized into the passivation defects. Unbound nanoparticles were washed away by short rinse with buffer A. The flow cell was

rinsed for 5 min with 10mM TCEP in buffer A and incubated further for 1hour. TCEP was flushed away by rinsing the flow cell with buffer A for 5 minutes. The flow cell was rinsed with 100μl of maleimide-PEG functionalised particles (obtained by reacting PEG functionalised particles with SMCC for 1.5 hours in pH 7.4) for 5 minutes. Co-incubation of immobilised Hsp90-PEG particles with maleimide-PEG particles for 2 hours leads to formation of dimers with 3% effciency. Unreacted maleimide-functionalised particles were removed by rinsing with buffer A for 30 minutes. The nanoparticle contaminated buffer A was changed every 10 minutes. The dimers were measured in buffer A to record thermally driven conformational changes in Hsp90.

D.2.1.9 Response of PEG-Hsp90-PEG tethered dimers

Several PEG-Hsp90-PEG linked gold dimers were measured in tandem to observe their behaviour over duration of 30 minutes. Time traces were collected in real time by dark-field setup with the temporal resolution of 100 ms at 28°C setup temperature. Large spectral shifts of 1-3 nm due to opening and closing of the Hsp90 molecule were observed with Hsp90 dimers in buffer A. The variation in spectral shifts observed among dimers could come from the 10% polydispersity of gold nanosphere solution synthesized by wet chemical approach. Histograms in figure D11 show the distribution of resonance maxima of the dimers during the measurement period of 30 minutes.
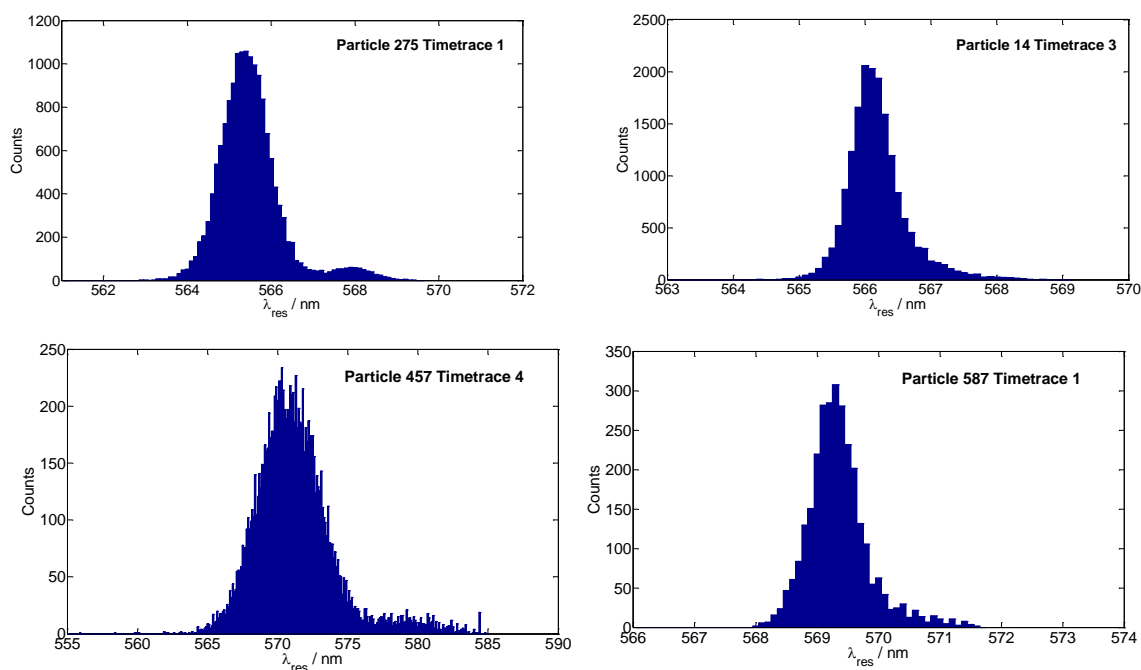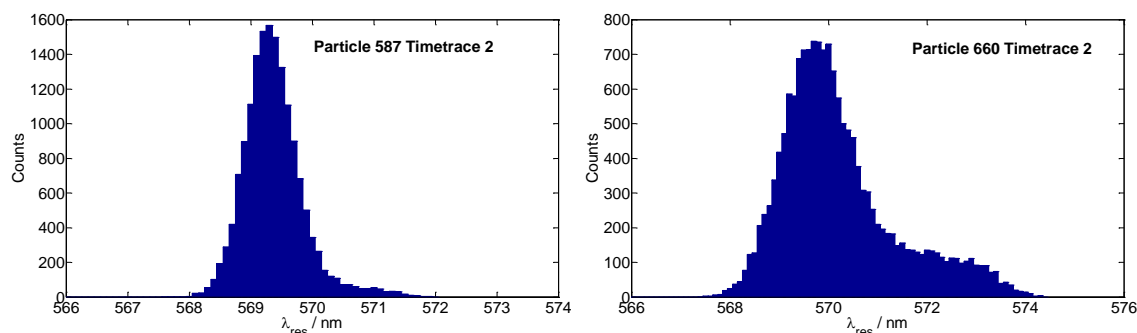
Figure D11. Histograms showing the change in resonance position of PEG-Hsp90-PEG linked gold dimer over 30 minutes duration in buffer A. At constant ionic strength the spectral shifts in λ_{res} were observed.

D.2.1.10 Spectral shift in Hsp90 dimer due to conformational changes in the protein

To make sure that the effects observed due to conformational changes in Hsp90 are real, the time resolved spectras in the open and closed states were sorted and averaged. The average spectra in the closed state shifts by 2.3 nm as compared to the open state. The spectral shift is also accompanied by intensity change (Figure D12).
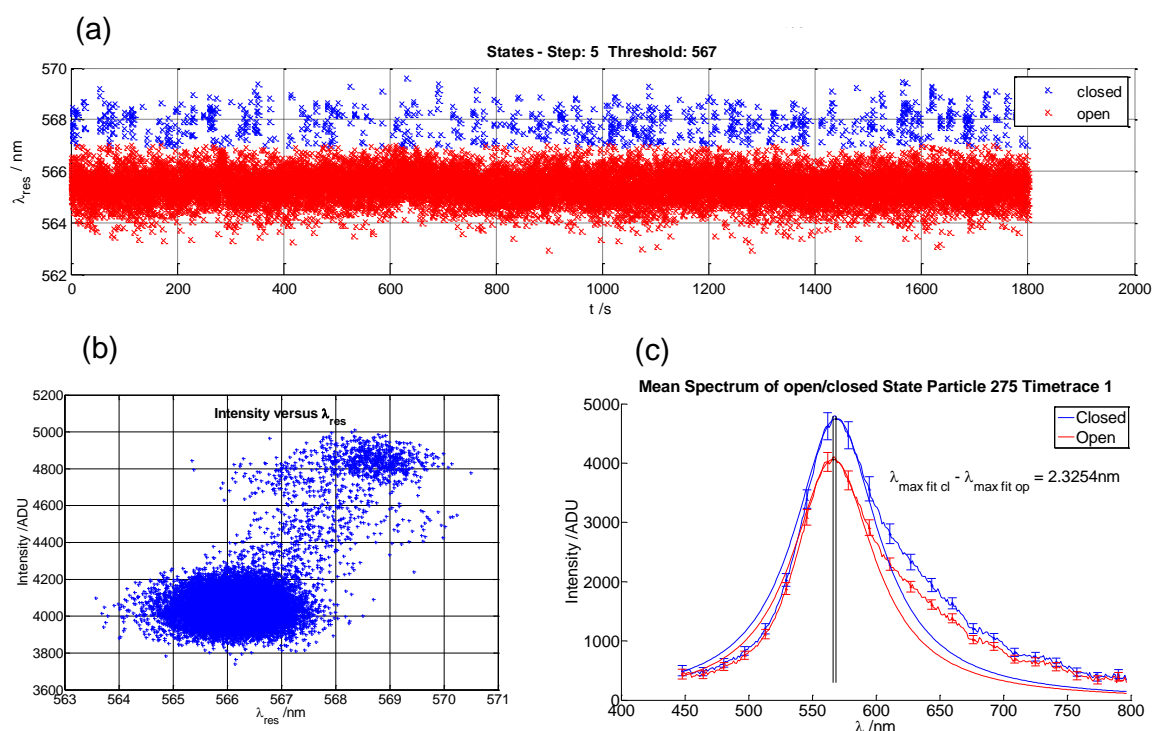
Figure D12. (a) A typical time trace of Hsp90 dimer showing open (red) and closed (blue) states (b) the spectrum in the closed state is marked by a spectral red shift and higher intensity (c) the average spectra in the closed state is spectrally shifted by 2.3 nm with respect to the open state (spectra is fitted with Lorentzian, only top 20% region from the peak position of the spectrum is fitted).

D.2.1.11 Formation of PEG Dimers

The flow cell channel was passivated with crosslinked BSA or APTES-PEG as mentioned elsewhere. Dithiol-PEG functionalized 40 nm gold nanospheres (see particle functionalisation section) in buffer A (40mM Hepes, 150mM KCl, 10mM $MgCl_2$, pH: 7.4) were immobilized into the passivation defects. Unbound nanoparticles were washed away by short rinse with buffer A. The flow cell was rinsed for 5 min with 10mM TCEP in buffer A and incubated further for 1hour. TCEP was flushed away by rinsing the flow cell with buffer A for 5 minutes. The flow cell was rinsed with 100µl of maleimide-PEG functionalised particles (obtained by reacting PEG functionalised particles with SMCC for 1.5 hours in pH 7.4) for 5 minutes. Co-incubation of immobilised dithiol-PEG particles with maleimide-PEG particles for 2 hours lead to formation of dimers with 3% effciency. Unreacted maleimide-functionalised particles were removed by rinsing with buffer A for 30 minutes. The nanoparticle contaminated buffer A was changed every 10 minutes. The dimers were measured in buffer A to record any linker dynamics in PEG monolayer.

D.2.1.12 Response of PEG tethered Dimers in buffer A

Several PEG linked gold dimers were measured in tandem to observe their behavior over duration of 30 minutes. Time traces were collected in real time by dark-field setup with the temporal resolution of 100 ms at $28^{o}C$ setup temperature. No large changes in spectral shifts were observed with PEG dimers in buffer A (40mM Hepes, 150mM KCl, 10mM $MgCl_2$, pH: 7.4). The resonance position of the dimer spectra did not change by 0.5-0.7 nm, which is within the noise level of our setups. Histograms in figure D13 show the distribution of resonance maxima of the dimers during the measurement period of 30 minutes.
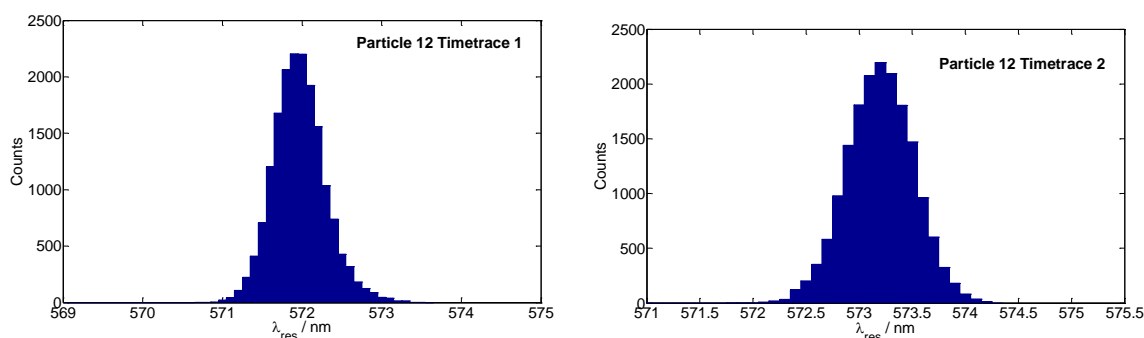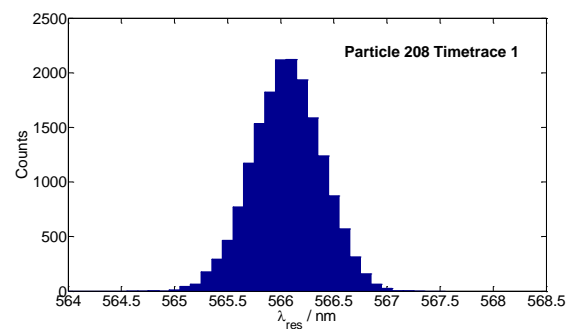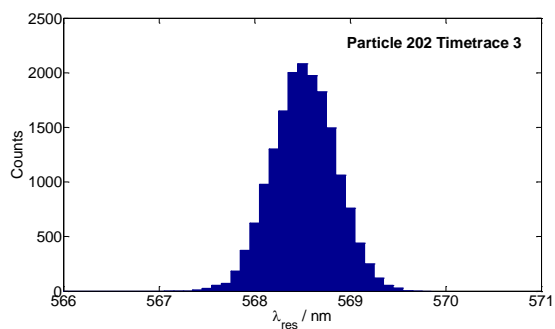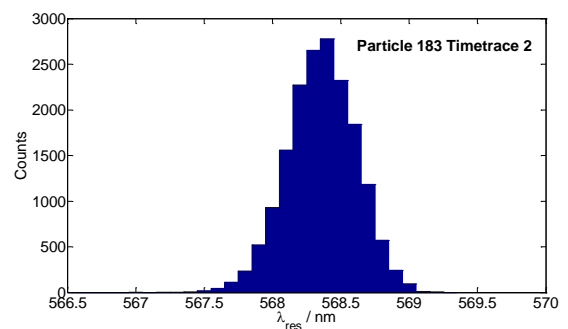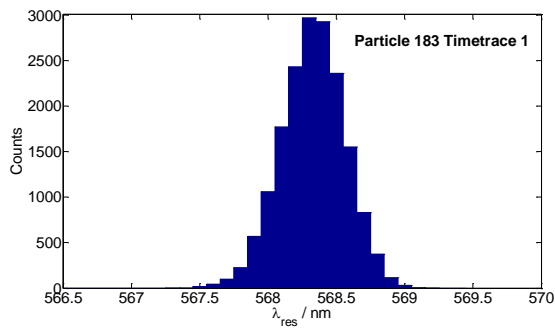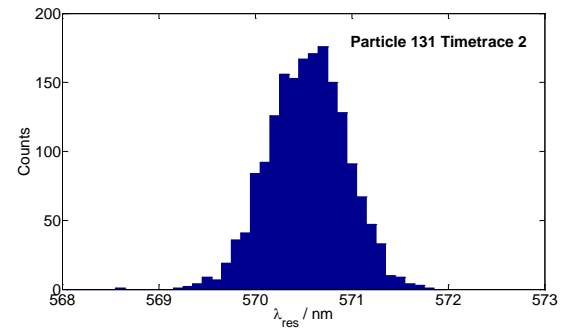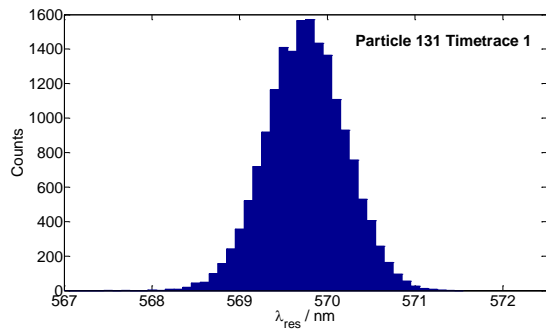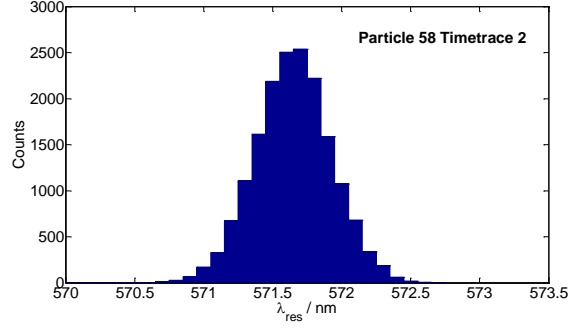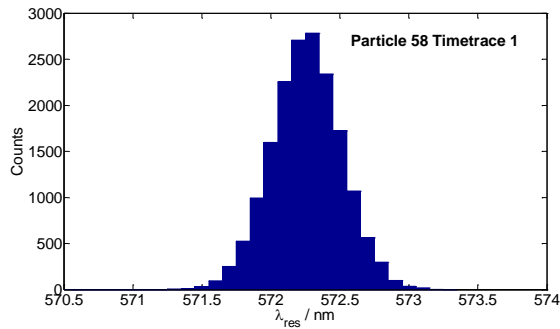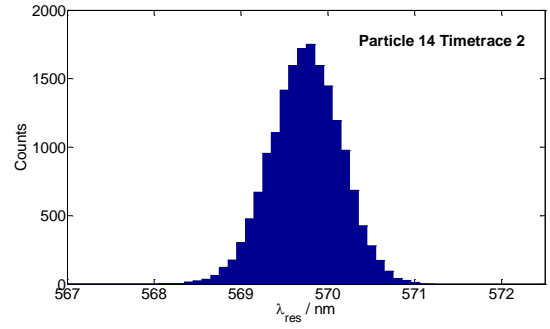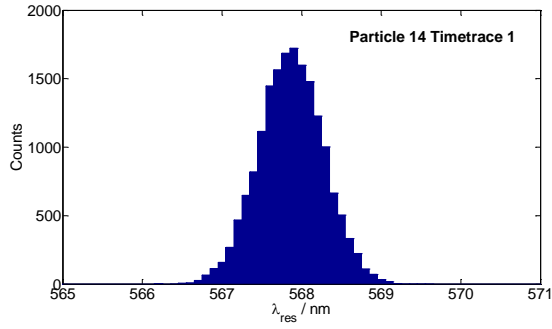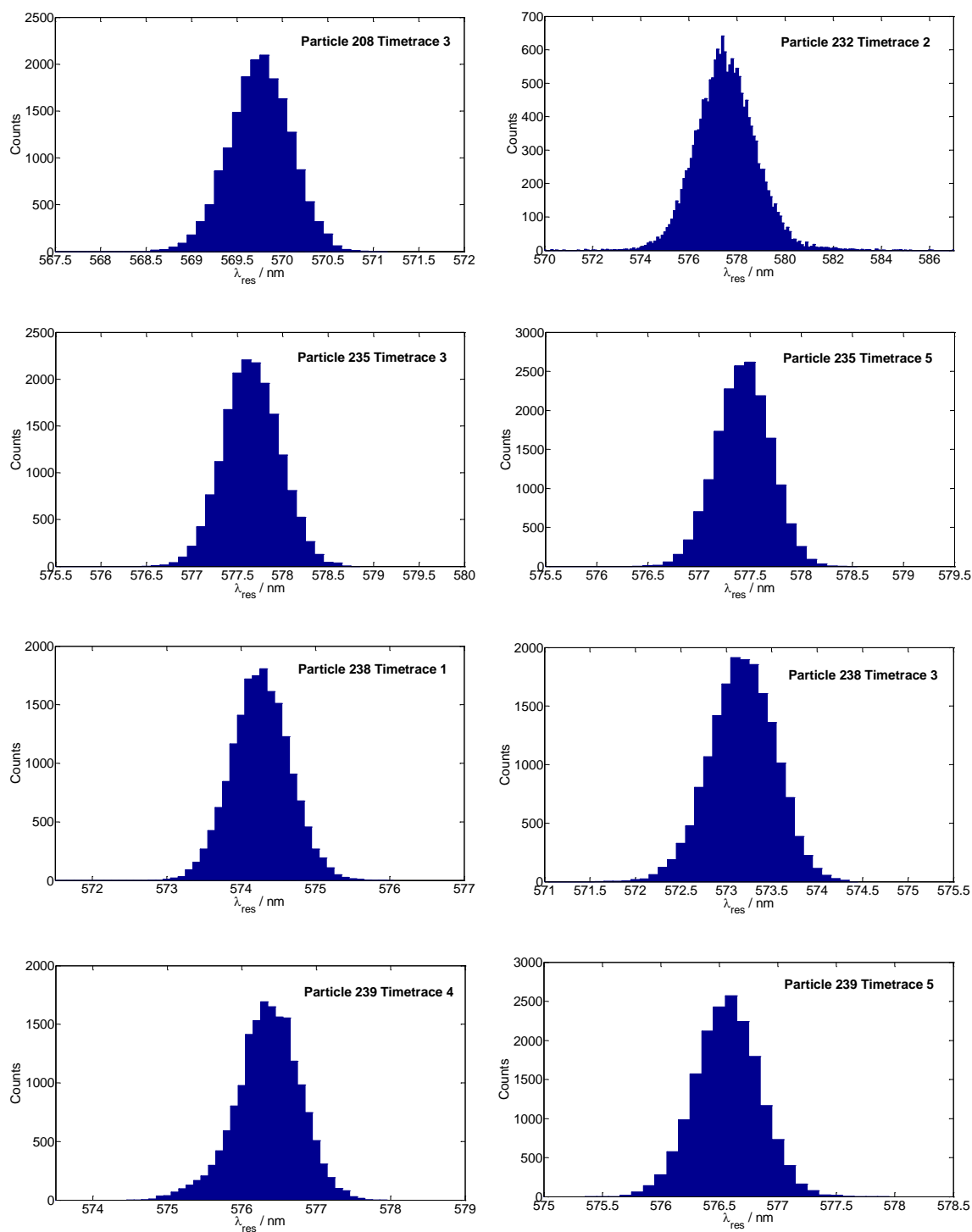
Figure D13. Histograms showing the change in resonance position of PEG linked gold dimer over 30 minutes duration in buffer A . At constant ionic strength no significant fluctuations in the spectral shifts were observed.

References

1. Ziegler, C.; Eychmüller, A. *The Journal of Physical Chemistry C* **2011,** 115, (11), 4502-4506.

2.   Zhang, F.; Sautter, K.; Larsen, A. M.; Findley, D. A.; Davis, R. C.; Samha, H.; Linford, M. R. *Langmuir* **2010,** 26, (18), 14648-14654.

3.   Chen, H.; Meisburger, S. P.; Pabit, S. A.; Sutton, J. L.; Webb, W. W.; Pollack, L. *Proceedings of the National Academy of Sciences* **2012,** 109, (3), 799-804.

4.   So″ti, C.; Vermes, Á.; Haystead, T. A. J.; Csermely, P. *European Journal of Biochemistry* **2003,** 270, (11), 2421-2428.

5.   Mihai, D. M.; Deng, H.; Kawamura, A. *Bioorganic & Medicinal Chemistry Letters* **2011,** 21, (14), 4134-4137.